IPS Instituto Politécnico de Setúbal
Escola Superior de Tecnologia de Setúbal

DANIEL ALEXANDRE FELICIANO PEREIRA

Additive manufacturing of rice husk filled PLA composites: Development and Characterization

Master's dissertation in Production Engineering

SUPERVISORS

Prof. Doctor Célio Gabriel Figueiredo Pina, ESTS/IPS

Prof. Doctor Ana Clara Lopes Marques, IST/UL

December 2021

DANIEL
ALEXANDRE
FELICIANO
PEREIRA

Additive manufacturing of rice husk filled PLA composites: Development and Characterization

Examination Commitee

Chairperson:

Prof. Doctor Pedro Filipe do Carmo Cunha

Supervisor:

Prof. Doctor Célio Gabriel Figueiredo Pina

Members of the comitee:

Prof. Doctor Ricardo António Lamberto Duarte Cláudio

December 2021

To my family

Acknowledgments

Firstly, I would like to thank Prof. Doctor Célio Gabriel Figueiredo Pina (ESTS/IPS) for accepting to be my advisor and for all the time he dedicated to my work, creating the conditions and solutions for the success of this work. I would also like to thank the co-advisor, Prof. Doctor Ana Clara Lopes Marques (IST/UL), for providing the necessary conditions for carrying out this work and all the follow-up given.

I also want to leave a vote of thanks to Prof. Doctor Ricardo António Lamberto Duarte Cláudio (ESTS/IPS), my scholarship coordinator, for being patient when I was more dedicated to this work, and for all his valuable suggestions.

Special thanks to Engineer Gonçalo Torres for all the help he gave me in laboratory tests.

Thanks to the researchers Sandro Matos (IST/UL) for all his support in my familiarization with the operation of the extruder and Mário Vale (IST/UL) for the analysis carried out on some materials and for all his willingness to help.

Abstract

The number of published scientific papers about natural fibers as a filler to produce composite filaments for additive manufacturing (AM) has increased in recent years. The aim of this thesis is to develop and characterize rice husk filled PLA composites obtained by AM. Thus, rice husks (RH) were blended with PLA (Ingeo™ Biopolymer 4043D) to produce natural fiber-filled polymer (NFFP) filaments for AM with fiber amounts between 5 and 20 wt.%. Raw materials, filaments produced and printed parts were characterized. The results showed that the filaments with a fiber content above 15 wt.% were not printable. Adding RH fibers to PLA negatively affected the mechanical strength, water absorption and densities on printed parts, mainly due to high variation in the filament diameter.

Keywords: Rice husk, Natural fiber-filled polymer, Additive Manufacturing; PLA

Resumo

O número de artigos científicos publicados sobre fibras naturais como enchimento na produção de filamentos compósitos para fabrico aditivo (FA) tem aumentado nos últimos anos. O objetivo desta tese foi desenvolver e caracterizar compósitos de PLA e casca de arroz obtidos por FA. Assim, cascas de arroz (CA) foram misturadas com PLA (IngeoTM Biopolymer 4043D) para produzir filamentos de polímero preenchido com fibra natural (PPFN) para FA, com quantidades de fibra a variar entre 5 e 20% em peso. Matérias-primas, filamentos produzidos e peças impressas foram caracterizados. Os resultados mostraram que os filamentos com um conteúdo em fibra superior a 15% em peso não eram imprimíveis. Além disso, adicionar fibras de CA ao PLA afetou negativamente a resistência mecânica, absorção de água e densidades das peças impressas, principalmente devido à variação no diâmetro do filamento.

Palavras chave: Casca de arroz, Polímero com enchimento de fibra natural, Fabrico aditivo; PLA

Table of Contents

List of Figures

List of Tables

List of Acronyms

ASTM	American Society for Testing and Materials
AT	Alkali Treatment
DTG	Derivative Thermogravimetry
EBM	Electron Beam Melting
FDM	Fused Deposition Modeling
FTIR	Fourier Transform Infrared Spectroscopy
ISO	International Organization for Standardization
LA	Lactic Acid
MFA	Micro Fibrilar Angle
MFR	Melt Flow Rate
MVR	Melt Volume Rate
NA	Not Available
NFFP	Natural Fiber Filled Polymer
PBS	Polybutilene Succinate
PF	Plant Fiber
PHB	Polyhydroxybutyrate
PLA	Polylactic Acid
PP	Polypropylene
RH	Rice Husk
SEM	Scanning Electron Microscopy
SLA	Stereolithography
SLM	Selective laser melting
SLS	Selective laser sintering

SS	Single-screw
TGA	Thermal Gravimetric Analysis
TPC	Thermoplastic Copolyester
TS	Twin-screw
UTM	Universal Testing Machine
WA	Water Absorption

List of Symbols

ρ	Density [g/cm³]
σ_f	Flexural stress [MPa]
ε	Strain [mm/mm]
σ	Stress [MPa]
A	Cross-sectional area [mm²]
d	Depth of tested beam [mm]
Ø	Diameter [mm]
D	Diameter [mm]
T_g	Glass transition temperature [°C]
Δh	Height variation [mm]
h_0	Initial height of the specimen [mm
l_0	Initial length of the specimen [mm]
W_0	Initial weight of the sample [g]
L	Length [mm]
Δl	Length variation [mm]
F	Load [N]
T_m	Melting temperature [°C]
E	Modulus of elasticity [MPa]
E_B	Modulus of elasticity in bending [MPa]
T_β	Relaxation temperature [°C]
m	Slope of the tangent to the initial straight-line portion of the load-deflection curve [N/mm]
L	Support span [mm]

WA	Water absorption [%]
A	Weight of sample in air [g]
B	Weight of sample in liquid [g]
W_1	Weight of the sample after 24h in distilled water [g]
wt.%	Weight percentage
b	Width of tested beam [mm]

Chapter 1
Introduction

This chapter briefly introduces the increasing need to use more eco-friendly materials, especially in the polymers area. The potential of biopolymers and plant fibers to substitute petroleum-based materials, and the motivations and objectives of this work, are also described. An overview of the structure of the chapters is also addressed.

1.1. Introduction

The increasing awareness about environmental issues has stimulated the demand for more sustainable resources, eco-friendly materials and recyclable products throughout the last two decades. While legislation keeps tackling the emission of greenhouse gases worldwide, the scientific community and several industries are focused on developing green materials and more eco-friendly processes [1].

Petroleum-based polymers are well known for releasing significant amounts of greenhouse gases into the atmosphere during their production and being a nonrenewable resource for manufacturing goods [2]. As a potential substitute for traditional fossil fuel-based polymers, biopolymers are gaining more acceptance day by day and PLA (Poly Lactic Acid), one of the most researched biopolymers, is already used for packaging [3]. Along with biopolymers, natural fibers are emerging as a filler/reinforcement for polymer composites due to their availability, biodegradability, low cost and eco-friendliness[3]. Natural fiber-filled composites are already a reality, widely used in the automotive industry, mainly in panels and insulation [4]. Nevertheless, there are still some drawbacks in the composites filled with natural fibers used in the automotive industry to be fully biodegradable, the low glass transition temperature of biopolymers, such as PLA (≈55°C) and the thermal instability of the majority of natural fibers at temperatures ≥200°C, are two of them [1].

On the other hand, the use of PLA has increased drastically in the 3D printing area, also known as additive manufacturing (AM) is a promising technology that has been growing at a fast pace and, according to experts, will continue to grow through 2025 [5]. AM is being used both in the industrial and personal field, the latter mainly because this process requires no elaborate assemblies, have low energy consumption and most of the 3D printers are cheap, allowing everyone to have a 3D printer at their desk and easily download models freely from the internet and print them [6].

As a feedstock material for AM, PLA has attracted much attention from academic researchers because of its complete biodegradability [7]. Researchers have also begun to add plant fibers to PLA in order to produce a variety of composite filaments for fused deposition modeling (FDM) and, due to numerous challenges related to inherent characteristics of natural fibers (thermal stability, hydrophilicity, inhomogeneity in filler dispersion and creation of voids during processing), there has been very little literature published about FDM with natural fiber composites (NFC) [6],[7],[8]. Adding natural fibers as a filler in biopolymeric materials for FDM can reduce filaments cost and improve their degradability. In addition, it makes the AM part with a natural woody feeling, which with proper marketing, customers can realize that AM products can be made from renewable resources and have pleasing aesthetics[3],[7].

Natural fibers as a filler in FDM filaments provide a sustainable lifecycle for 3D printed products, once these fibers are waste products coming from industry or agriculture, often produced locally [6].

This master's thesis was motivated by the topic of biodegradable polymers for 3D printing, where natural fiber-filled composite (NFFC) filaments using a biopolymeric matrix were produced. For the matrix, PLA was used due to its low processing temperatures and biodegradability. About natural fibers for filling, choosing rice husks (RH) was driven by the fact that Polytechnic Institute of Setúbal (IPS) is located in a well-known district for planting rice. Moreover, since 1760 the rice crop has been an important economic source in the Sado river valley [9]. The application of RH as a filler was not only about applying a subproduct of a traditional crop of the region. It was also related to the processability of RH in a single screw extruder and being suitable for use as polymer filler [10],[11],[12].

1.2. Objectives

The aim of this thesis is to develop and characterize rice husk filled PLA composites obtained by fuse deposition modeling (FDM).

The specific objectives were to evaluate the effect of:

- Alkali treatment in fibers structure;
- Fiber content on printability;
- Fiber content and printing parameters on the properties of printed parts.

In order to fulfill these objectives, rice husk fibers were prepared, sieved, alkali-treated, dried and blended with PLA to extrude AM filaments with 0%, 5%, 10%, 15% and 20% wt.% in fiber. Fibers had their densities and thermal stability determined and an FTIR spectroscopy was done to analyze the fiber chemical structure change due to alkali treatment. The produced filaments had printability tests and printable filaments were used to print specimens for density measurements, water absorption determination and mechanical testing. Moreover, all filament blends had their density and thermal stability determined and SEM imaging was used to study fiber morphologies and fracture surfaces of tensile and flexural tested specimens.

1.3. Chapter structure

The chapter structure of this dissertation is a chronologic sequence of the work done. The main chapters primary content are:

Chapter 1 - Introduction: A brief introduction to the thesis theme is done. Objectives for the work are defined and an overview of the chapters is described.

Chapter 2 – Literature review: Contains the literature review needed to achieve the objectives of this work. Where raw materials, chemical treatment procedures, processes and process variables used by researchers in this type of materials are studied.

Chapter 3 – Materials and methods: The materials used and their preparation procedures for filament extrusion and further use on AM are described. Tests to characterize the mechanical properties, densities, water absorption, morphologies, thermal behavior and chemical structures of the obtained materials and printed parts are also detailed.

Chapter 4 – Results: The results from the materials characterization tests and analysis done are shown.

Chapter 5 – Discussion: An analysis of the obtained results is done.

Chapter 6 – Conclusions and future work: The conclusion of the results for the objectives of this work is done. Few considerations for future work are also done.

Chapter 2
Literature Review

This chapter is divided into 3 topics encompassing relevant concepts for producing and 3D printing natural fiber-filled polymer (NFFP) filaments. The first part of the literature review describes the types, properties and nomenclature used for plant fibers and their preparation for further alkali treatment. In the second part, poly(lactic acid) (PLA) and its relevant properties for use as a matrix in NFFP materials for 3D printing are characterized. In addition, a brief introduction to the extrusion process of filaments for 3D printing and its importance on the quality of materials obtained. In the last part of the literature review, the main scope is additive manufacturing (AM) with NFFP, 3D printers and 3D printing process general concepts applied to this type of materials. The printed parts properties are also addressed.

2.1. Plant fibers

Fibers extracted from plants are a renewable source of raw material and the next generation of reinforcement/filler for polymer-based materials [13]. In addition to coming from renewable sources, these fibers are inexpensive and degradable. Their abundance, low density and satisfactory mechanical properties make them attractive alternatives to man-made fibers [13]. Cheap natural fibers also balance the relatively high cost of a biodegradable matrix (e.g., PBS, PBA, PLA). Thus green compounds are attracting substantial interest from the scientific community and industry [14].

A plant fiber (PF) is a composite made of cellulose, hemicellulose, lignin, pectin, waxes and water-soluble substances, where lignin binds the hollow cellulose fibrils in the hemicellulose matrix [15],[16]. Cellulose is the most available biopolymer on earth and the main PF element, providing structural stability, high strength and stiffness to the fiber [4],[16]. Fibers from both herbaceous (nonwoody) and woody plants have cellulose, lignin and hemicellulose in their cell walls [17]. These natural polymers (cellulose, lignin and hemicellulose) combined are often known as lignocellulosic materials and are extensively used globally, with an estimated annual production of 10-50 billion tons (50% of the produced biomass) [18]. Lignocellulosic materials have been successfully applied in packaging, with several innovative commercial products already deployed on the market (Figure 1). Although some products made of PF are available on the market, using PF as a reinforcement/filler in a thermoplastic matrix is still very challenging, especially with nonhygroscopic synthetic thermoplastic matrices.

Figure 1 - Examples of packaging innovations using natural fibers [19].

One of the several challenges that arise when using PF as reinforcement/filler in polymeric matrices is the fact that the fibers are hydrophilic and tend to have poor adhesion to polymeric (hydrophobic) matrices [4],[15],[20],[21]. This poor bonding between matrices and fibers and the high moisture absorption of PF restrict the application of these materials to non-structural and indoor purposes [22]. Adhesion promoters or chemical changes to fibers are often used to minimize this problem, where different mechanisms modify the surface properties of the fibers, such as eliminating weak boundary layers and changing acidity-alkalinity [21]. When using fibers

from plants to produce materials, inhomogeneities in size and natural defects (due to plant growth) in their surface and volume must also be considered [13].

2.1.1. Types and properties of plant fibers

Plant fibers are categorized accordingly to their origin in the plant structure. These fibers can be extracted from the bast/stem, stalk, leaves, fruit/seed, or straw/grass (Figure 3) [13]. Plants are also classified as woody or nonwoody feedstock and both of these designations encompass the lignocellulosic material definition, a generic denomination for materials derived from a wide range of plants [17]. Lignocellulosic fibers composition can vary significantly within the same type of plant. Changes in fibers properties are related to geographical regions of plant cultivation, the extraction process, the origin of the fiber in the plant structure and the age of the plant [23]. Depicted in Figure 2 are examples of nonwoody (herbaceous) and woody plants and from left to right are represented flax, wheat, switchgrass, miscanthus, kenaf and corn, that are in the nonwoody plant grade. The woody plants are the hardwood tree, softwood tree, palm and bamboo from right to left [17]. The simplest way to distinguish woody from nonwoody feedstock is by the plant stem. Woody plants have stems typically rigid/non-bendable that live for several years, adding growth (height and width) year after year [24]. On the other side, nonwoody feedstock has easily bendable stems and their lifecycle is usually annual [24].

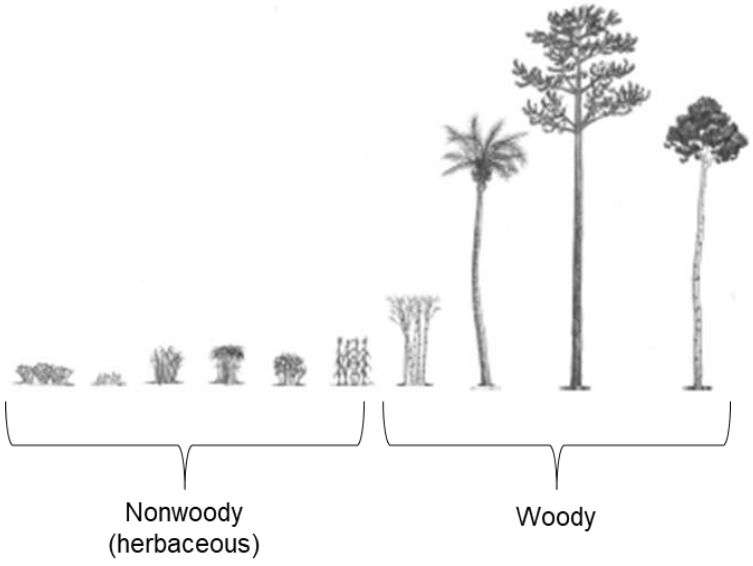

Figure 2- Overview of some woody and nonwoody plants (Adapted from [17]*).*

The three major natural polymers that form a natural fiber cell wall are cellulose, hemicellulose and lignin (Figure 4). From these, cellulose is the main element and gives mechanical strength and stiffness to the fiber. Cellulose is a semicrystalline polymer with a structure consisting of high crystalline and amorphous regions, where the crystallinity packing and degree of polymerization, as well as microfibrillar angle (MFA), plays a critical role in PF mechanical properties [1],[25]. Cellulose is also resistant to strong alkali (17.5 wt.%) and

somewhat resistant to oxidizing agents [26]. Either in woody or nonwoody plants, the mechanical properties of a fiber are defined by the fiber content in cellulose (wt.%) and MFA [25]. With the fiber axis as a reference, fibers are more ductile when MFA is higher and more rigid with superior tensile strength when the MFA is lower [1],[25]. Moreover, fibers with high density have higher stiffness and mechanical strength than those with less density [1].

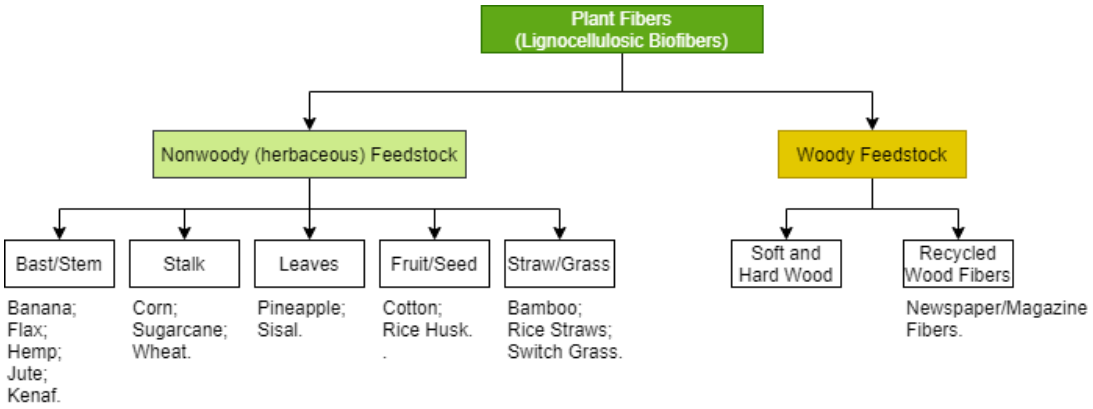

Figure 3- Plant fiber sources [13],[25].

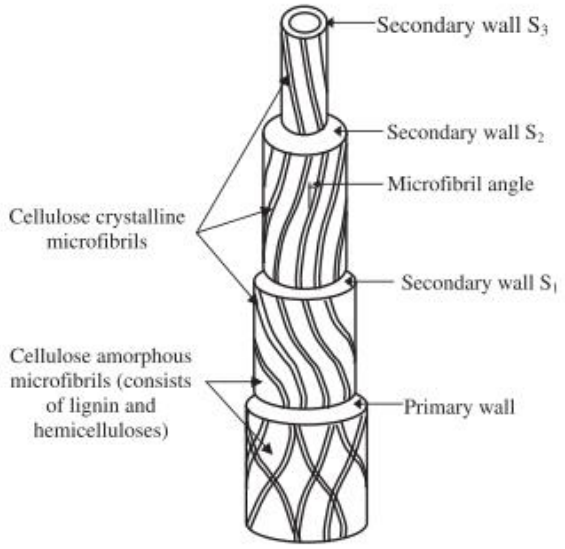

Figure 4- Structure of a natural fiber [27].

The hydrophilicity of PF is attributed to cellulose and the high hydroxide concentrations in its composition [15],[25]. These hydroxides form not only hydrogen bonds between (and within) cellulose macromolecules but also with the hydroxy groups of air [25]. Another contributor to PF moisture absorption is hemicellulose, which is very hydrophilic and soluble in alkali [26]. Therefore, the selection of PF as reinforcement/filler has cellulose content as one of several critical variables. More cellulose content better the mechanical performance of the fiber, but, on the other side, moisture absorption increases.

Fiber thermal stability is another critical property of the PF since most thermoplastic matrices have processing temperatures above 200°C. Hemicellulose is the support matrix for the cellulose and the first lignocellulosic compound to have thermal degradation and due to that, the loss of mechanical strength of PF starts approximately at 200°C (thermal degradation of hemicellulose is between 190-280°C [23]), as shown in Figure 5. Lignin, the most thermal resistant compound of a lignocellulosic fiber, has its chemical composition not yet well defined and is known to be amorphous and hydrophobic [26]. It is a thermoplastic made by nature with a glass transition temperature of around 90°C and a melting point of about 170°C, also easily oxidable and soluble in hot alkali solutions [26].

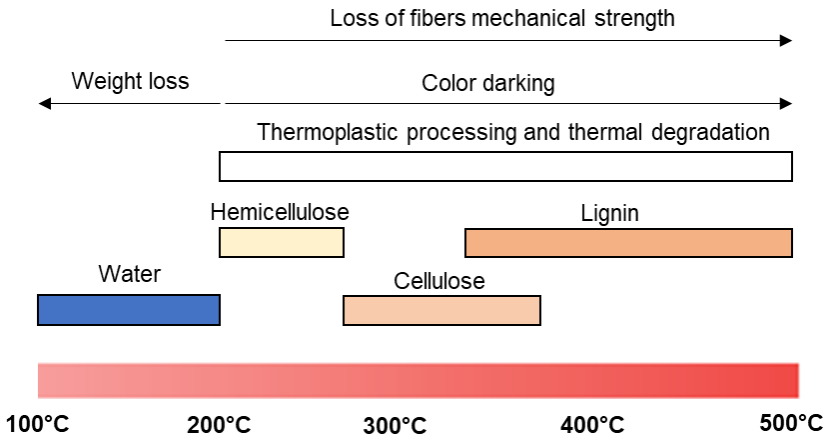

Figure 5- Thermal decomposition ranges of lignocellulosic constituents (Adapted from [23]*).*

Several factors affect the mechanical and thermal properties of different types of fibers. However, the balance between fiber content in hemicellulose and cellulose has been revealed to be a significant element when choosing a type of fiber to use as a filler/reinforcement in thermoplastic materials.

Some advantages and disadvantages of PF use in material development are listed below:

- Advantages [1]:
    - Environmentally friendly, biodegradable and a renewable source of raw material;
    - Inexpensive, abundantly available, reducing the overall costs in composite materials;
    - Provide better occupational safety (less dermal and respiratory irritation);
    - Some plant fibers are less abrasive (than mineral ones) and increase the overall life span and efficiency of processing equipment;
    - Their lightweight can improve fuel efficiency in automotive applications;
    - Promote agricultural residues use, stimulating the job market and income using a usually disposable subproduct of crops.

- Disadvantages [1]:
    - High moisture absorption;
    - Low wettability, leading to loss of mechanical properties when used in hydrophobic matrices, due to weak fiber-matrix bonding;
    - Easily flammable with low thermal degradation temperatures, but also susceptible to fungal attacks;
    - Fiber characteristics and properties can vary significantly, even within the same crop;
    - Weather and cultivation conditions directly affect fiber quality and either price and supply.

Detailed in Table 1 are some PF chemical and physical properties data collected from the literature.

Table 1- Density, chemical composition and MFA representative values of few lignocellulosic fibers (Data collected from [1],[16],[17],[26],[28],[29]*).*

Fiber type	Density (g/cm³)	Cellulose (wt.%)	Hemicellulose (wt.%)	Lignin (%)	MFA (°)
Nonwoody Feedstock					
Bast/Stem					
Banana	1.3	44-64	10	5-7.5	10-25
Flax	1.5	64-71	18.6-20.6	2.2-2.5	5-11
Hemp	1.47	70-74	17.9-22.4	3.7-5.7	2-6.2
Jute	1.3-1.5	61-71.5	13.6-20.4	12-13	7-9
Kenaf	1.5-1.6	45-59	21.5	8-19	9-15
Stalk					
Corn		32-40	20-39.8	5-34	
Sugarcane		25-45	28-32	15-25	
Wheat		29-39.9	16-28.2	15.6-21.5	
Leaves					
Pineapple	0.8-1.6	70-82		8-13	8-14
Sisal	1.3	66-78	10-14	10-14	10-22
Fruit/Seed					
Cotton	1.6	85-90	5.7	0.75	20-30
Rice Husk	1-1.6	29.7-35.6	11.9-29.3	15.4-20	
Straw/Grass					
Bamboo	0.6-1.1	20-60	24.1-27.7	21-31	8-11
Rice Straws		29.2-35.6	11.9-29.3	15.4-20	
Switch Grass	1.4	32.4	26.3-29.3	20.1-23	
Woody Feedstock					
Softwood		40-45	7-14	26-34	7.4-45
Hardwood		38-49	19-26	23-30	

2.1.2. Plant fiber preparation for FDM composite materials

Fiber geometry and size are the main factors that directly affect the printability of NFC FDM filaments [30]. Thus, adequate fiber granulometry is essential for a printable filament because PF in composite filaments can cause print nozzle clogging, which frequently occurs with particle size >400µm [31]. The influence of fiber size in printability was determined by N. Petchwattana *et al.* [30], who produced PLA/WF (wood flour) filaments with a particle size of 125µm and 74µm, obtaining only successful results in printability with 74 µm WF. Christian *et al.* [32] also studied the effect of particle size on the printability of composite filaments and they concluded either that filaments with larger particle sizes cannot be printed, especially in high filled filaments. M. Morales *et al.* [33] developed printable filaments made of recycled polypropylene and rice husk (RH), where RH had a granulometry between 250 and 425 µm. D. Depuydt *et al.* [34] produced composite filaments with PLA and bamboo/flax fibers, the dimension of the fibers used was between 315 and 630 µm and some parts were printed after a nozzle adaptation. Y. Tao *et al.* [35] concluded that WF/PLA filament is suitable for 3D printing after producing filament with an average particle size of 14 µm.

FDM literature is often incomplete in fiber morphology information and average particle dimensions frequently come from the mesh sizes used for sieving procedures instead of detailed geometrical characteristics [6]. Although this fact, a specific study in filament tensile testing made by D. Depuydt *et al.* demonstrated that the length/diameter (L/D) ratio is a critical geometric parameter [6],[34]. Furthermore, since most printers use a nozzle diameter of 0.4 mm, this L/D ratio is somehow related to nozzle geometry [6]. Nozzle diameter has been decisive in fiber dimensions used in several studies, showing that printability of larger fiber sizes is linked to greater nozzle diameters. An example of this was the works of M. Morales *et al.* and D. Depuydt *et al.,* the former used RH fibers sized between 250 and 425 µm (with a Ø 0.8mm nozzle) and the latter used bamboo/flax fibers with dimensions between 315 and 630 µm (with a modified nozzle), both of these studies had printability of their filaments. On the other hand, in the study of Petchwattana *et al.,* where WF fibers were used, filament containing fibers with an average size of 125µm was not printable, but in this work, the nozzle had Ø 0.4mm.

In this pre-processing stage, a correct selection of fiber L/D ratio can significantly reduce the unsuccess of filaments in 3D printing. In filaments for commercial purposes, fiber dimensions (L and D) must not pass the standard nozzle diameter (0.4 mm). Other issues can influence the printability of these materials, such as material flow, viscosity variations and the fact that fibers are prone to agglomeration [8].

The typical fiber preparation process for FDM materials is depicted in Figure 6. This procedure consists mainly of washing, grinding and sieving the fibers until the desired granulometry. Washing procedure before grinding removes impurities and may chemically modify the surface of fibers depending on water temperature. M. Benítez-Guerrero *et al.* [36] conducted a study about the effects of washing and grinding on sisal fibers and they concluded that fibers

washed in hot water have partial solubilization of minerals, hemicellulose and other carbohydrates of low molecular weight.

PF chemical structure changes start at this stage, not only by the physical effect of grinding fibers, which cause fiber defibrillation and loss of mechanical strength, but also by the exposure of hydrophilic groups that increase fiber moisture absorption [36]. Mechanical grinding destroys cell walls and due to this, the crystalline cellulose fraction on fiber surface decreases along with an increased proportion of amorphous intracellular components [36]. Grinding is employed for both size reduction and fiber surface exposure for chemical treatment [37].

In brief, fiber preparation is the first pre-processing step for producing plant fiber composite filaments for 3D printing and is decisive in filament printability.

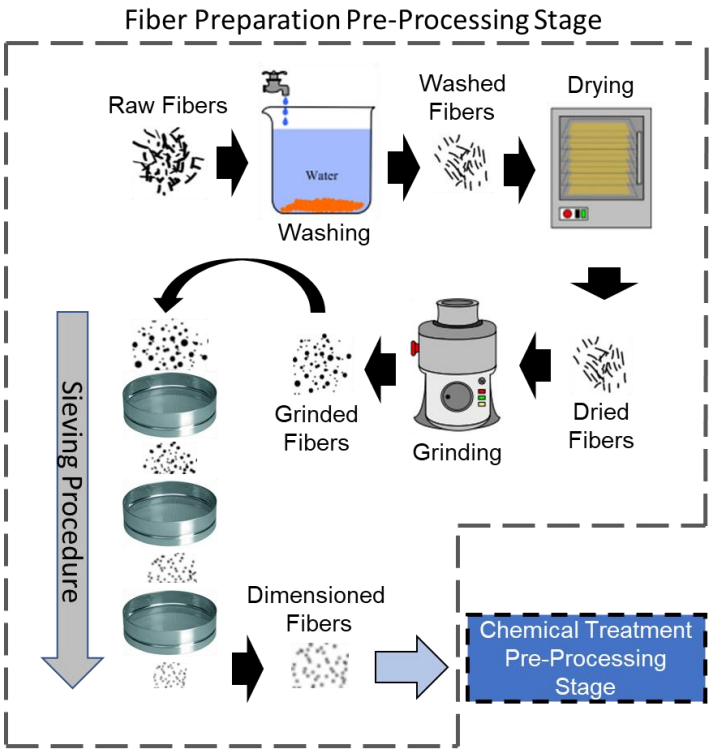

Figure 6- Typical plant fiber preparation for FDM materials (Adapted from [12],[38]*).*

2.1.3. Alkali treatment

Among the different chemical treatments available for plant fibers that have been reported in the literature, alkali treatment (AT) is the most used because it is very effective in surface modification and also economic [15],[21],[39],[40]. Thus, the scope of the literature review in the current topic was focused on alkali treatment (with sodium hydroxide), mainly because it was the chemical treatment used in this work and the number of literature about plant fiber chemical treatments published is very extensive.

Alkali treatment (or mercerization) is a process where fibers are subjected to a strong base solution to disrupt hydrogen bonds in the PF network structure (Figure 7), with resultant changes

in the dimensions and morphology of the fibers and their mechanical performance [15],[21]. This treatment removes lignin, wax, oils and depolymerizes the fiber cell wall [27]. Hemicellulose, which is very sensitive to alkali solutions, is removed in variable amounts (depending on time exposure to NaOH solution), increasing the number of cellulose crystallites exposed in the fiber surface [25]. When hemicelluloses are removed, the interfibrillar region decreases its density and rigidity, making the fibrils more able to rearrange themselves in the direction of mechanical loads [25]. However, B. Koohestani *et al.* [21], in a literature review about natural fiber treatments, referred that a decrease in tensile strength of PF may occur as a result of this reduction of hemicellulose content.

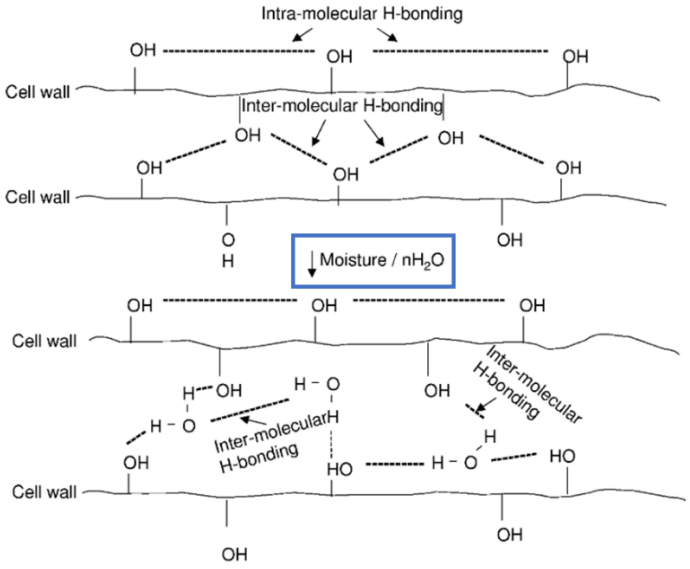

Figure 7- Schematic representation of intramolecular and intermolecular hydrogen bonding in PF(Adapted from [25]*).*

In general, the value added by alkali treatment on PF used in composites is an increase in fiber surface roughness (resulting in a more stable fiber-matrix interlocking) and moisture absorption (Figure 7) resistance improvement [15],[21]. AT chemical reaction between PF and NaOH occurs as follows :

$$\text{PF Cell-OH} + NaOH \rightarrow \text{PF Cell-}O^{-}Na^{+} + H_2O + \text{Surface impurities.}$$

The positive effects of NaOH treatment on fibers depend on solution concentration and the time that fibers are immersed in it [41]. M. Kathirsevalm *et al.* [42] assessed this treatment dependency on time and solution concentration in thespesia populnea (a typical tree in Pacific islands) bast fibers, where it was concluded that the optimal treatment is with 5% NaOH concentration for 60 min. An increase in weight fraction of cellulose (8.75%) was observed, attributed to the fact that some hemicellulose and lignin were diluted in NaOH solution. The right time and concentration for alkali treatment is not a straightforward process, depends on fiber chemical constitution and if the alkali concentration is higher than the ideal, delignification (excess of lignin removal) can occur and damage the fibers [27]. As a result of high NaOH concentration, fiber damage was reported by T. Tran *et al.* [41], where wheat and rice husks were subjected to

a 2, 5 and 10% NaOH concentration. Fibers immersed in a 10% NaOH solution for 24h (at room temperature) were destroyed. In this study, weight loss was analyzed as a function of NaOH concentration (in a 24h treatment) (Figure 8a), showing that increasing the concentration affects fiber weight loss, which is linked to higher dissolution rates of alkali sensitive compounds. This dissolution had a time milestone and weight loss increased more significantly under an 18h period than after, as shown in Figure 8b. In terms of moisture absorption (Figure 8c), both husks had maximum absorption values at 5% NaOH concentration, this evolution among the increase of concentration until 5% value is related to the exposure of hydroxyls on the fiber surface and at higher concentrations of NaOH, AT may change cellulose crystallinity and reduce the polarity of the fibers surface, resulting in water absorption decrease.

As already mentioned, AT is not a linear procedure and results obtained from the same concentration and time used can vary widely, depending on fiber chemical composition. The results obtained by T. Tran *et al.*, compared with those obtained by Kathirsevalm *et al.*, highlight the importance of AT adaption to the type and chemical composition of fibers used. On rice and wheat husks, it was reported by T. Tran *et al.* that 5% NaOH solution fibers reached the maximum water absorption value (Figure 8c), while Kathirsevalm *et al.* obtained an optimal AT with 5% of NaOH (Figure 9). For both works, weight/size changes showed a strong dependency on the time of AT. Although better results in water absorption being pointed to thespesia populnea bast fibers, in T. Tran *et al.* experiment, it was not very clear the time of AT considered for moisture absorption analysis.

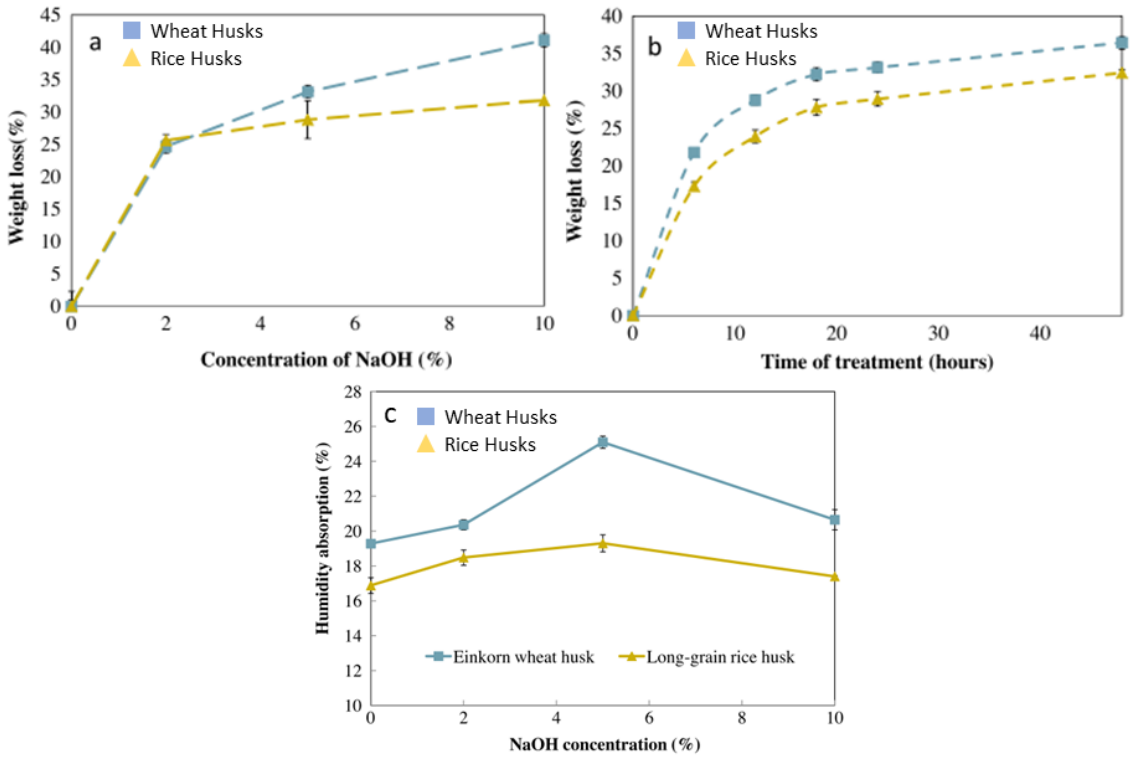

Figure 8- a) Weight loss as a function of NaOH concentration (24h Treatment); b) Weight loss as a function of treatment time (5% NaOH concentration); c) Moisture absorption as a function of NaOH concentration [41].

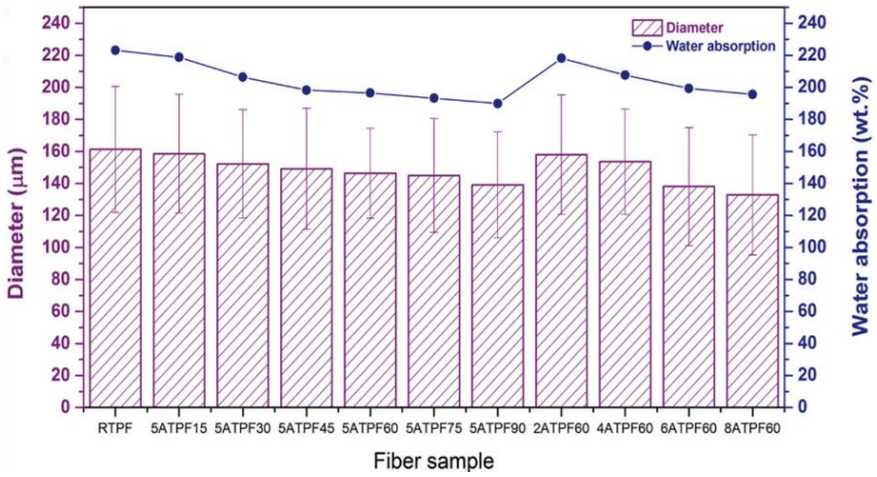

Figure 9- Fiber diameter and water absorption variation, as a function of NaOH concentrations of 2%, 4%, 6% and 8% with a variable time of exposure between 15 min and 60 min, in thespesia populnea bast fibers [42].

In Table 2 are values surveyed from the literature about AT (with NaOH), where information about concentration, time and temperature, used for different fibers was compiled from different works. It is evident that the most used concentration is 5% and the time of treatment, despite the variation, is mostly under 8h. A relationship between AT time/concentration and fibers chemical constituents percentages (Cellulose, hemicellulose and lignin) to determine the ideal values before treatment was not evident from the literature used. However, many authors had done a chemical analysis of the fibers before and after AT.

Table 2- Alkali (with NaOH) treatment details for different fibers surveyed from literature.

Fiber	Concentration	Time of AT	Temperature	Ref.
Pineapple Leaf	5%	2h		[21]
Sisal	5%	72h		[21]
Jute	5%	8h		[21]
Jute	5%	4, 6 and 8h		[27]
Hemp	8%			[27]
Coir	5%			[27]
Rice Straw	5%	2h	Room	[39]
Flax; Hemp; Kenaf	4%	3h	Room	[40]
Rice Husk	4%	2h		[43]
Abaca	5%; 10%; 15%; 20%	72h	30°C	[44]
Rice Husk	4%	2h	≈90°C	[45]
Palmyra	5%	1h	Room	[46]
Hemp	1%; 5%	30min		[47]

2. Extrusion of natural fiber filled polymer (NFFP) filaments for 3D printing.

The development of new thermoplastic filaments is one of the biggest challenges in the 3D printing industry [48]. 3D printing filaments are considered semi-finished products and in composite materials, the material performance is mainly determined by how carefully semi-finished materials are produced (e.g., the AT PF) [49]. Problems related to mechanical and thermal properties degradation are typical of this process stage [49].

Amorphous polymers are preferred in filaments for AM processes over semicrystalline ones because, in parallel with their low volume variation during solidification, due to their liquid-like structure, their properties in the molten state are also better [6]. For AM composite filaments, PLA is the most used polymer (thermoplastic) matrix [50]. Obtained from lactic acid, which is typically extracted from vegetable and renewable resources, PLA is degradable in nature and the human body [50]. Furthermore, PLA has low processing temperatures, which make it an attractive polymer for use as a matrix in NFFP filaments, but its low glass transition temperature (T_g≈55°C) is still a disadvantage.The 3D printing market already has a wide offer of NFFP filaments made of PLA matrix (Figure 10). Several companies advertise these types of filaments as being environmentally friendly, biodegradable, less abrasive and with an additional woody aesthetic given to the printed parts.

Figure 10- a) esun® PLA/Wood filament [51]*; b) Prusa® PLA/Wood filament* [52]*; c) dowire® PLA/Wood filament* [53]*; d) Prusa® PLA/Cork filament* [52].

The manufacturing process of 3D printing filaments is by extrusion and here the process has two types of extruders available, single screw and twin screw extruder, where often the twin-screw extruder is pointed as the best option for better distribution of fibers on the matrix [54],[55]. However, a good distribution of fibers should be achievable with a single screw extruder if it has an adequate mixing screw [56].

2.2.1. Poly Lactic Acid (PLA)

The term PLA is used to classify generally 3 types of polymeric or copolymeric chains which that PLA can be made: PLLA (poly-L (lactic acid)), PDLA (poly-D (lactic acid)) and PDLLA (poly-D,L (lactic acid)) [57]. These polymeric chains are made of lactic acid (LA) and the process of obtaining lactic acid is, at its first stage, made by nature, when plants use energy from the sun to do photosynthesis within their cells, converting the carbon dioxide and water from the atmosphere into starch [58]. This starch is then extracted from the vegetable matter and transformed into fermentable sugar (e.g., Glucose), where carbon and several other elements present in these sugars are converted to LA through their fermentation (Figure 11) [58].

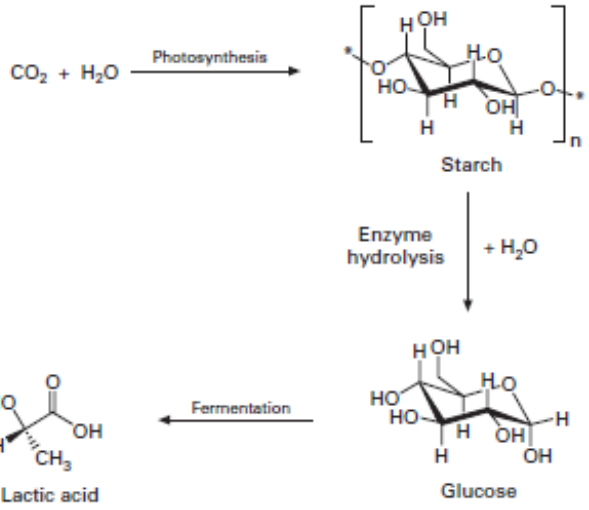

Figure 11- Production of lactic acid from renewable resources [58].

Obtaining LA is an intermediate step to producing PLA. Thus LA needs to be polymerized into PLA and for that, there are two routes available (Figure 12a): 1) direct condensation of LA or 2) through an intermediate lactide in a ring-opening process [58]. The direct condensation process requires a high vacuum and temperature. It consumes high amounts of energy during the whole process, making it unfeasible not only for economic reasons but also by taking out the eco-friendly purpose of using a biopolymer [58]. The ring-opening polymerization process needs much less energy consumption and for obvious reasons, production costs are considerably lower, along with an accentuated decrease in the ecological footprint of the process [58]. This lactide intermediate method was the base for a patent developed by NatureWorks® LLC, which produces many grades of PLA known as Ingeo™ biopolymer, often used in research works with composites using PF [58],[59].

Commercial PLA is usually supplied as a copolymer, where the proportion of each lactide (Figure 12b) influences the type of structure (amorphous or semicrystalline). L lactide, which constitutes the main volumetric fraction of PLA, when in a proportion superior to 90%, tends to make the polymer semicrystalline (and under totally amorphous) [60]. Litterature related to PLA remarks that more crystallinity and thermal resistance are linked to higher L-lactide content on polymer structure [60]. The proportion of each lactide (Figure 12b) on PLA structure is relevant

when working with PF because most fibers are unstable at temperatures above 200°C. More content of D or DL lactides makes PLA more amorphous and consequently, with lower processing temperatures, which is decisive to avoid the deterioration of the fibers during the extrusion of filaments [1],[61].

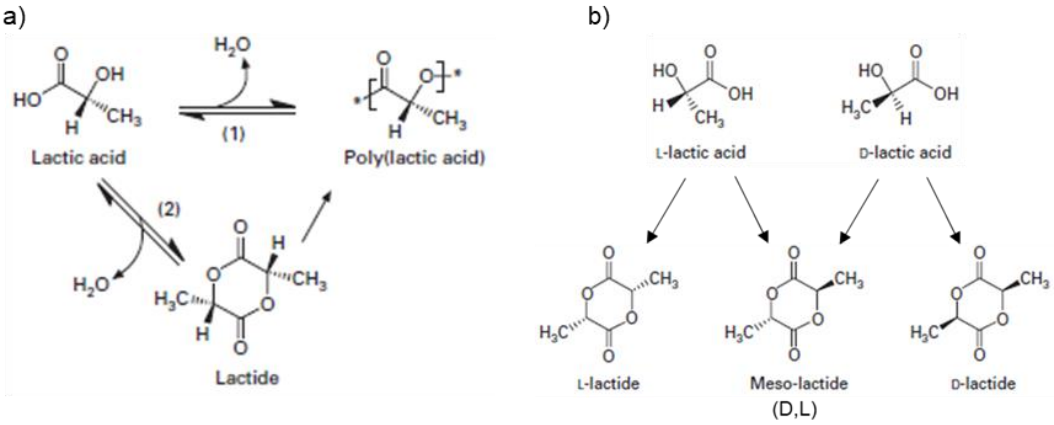

Figure 12- a) Polymerization routes to poly(lactic acid); b) Lactides derived from lactic acid Adapted from [58]).

For a good selection of the PLA to NFFP filament extrusion, it must be considered that while extruding, for a homogeneous mixture of fibers on the matrix, the polymer has to be above the melting temperature (T_m) to have an ideal viscosity [60]. For that, PLA at an amorphous state is the ideal choice for producing NFFP filaments since amorphous PLA has lower melting temperatures. Figure 13 represents the physical states of amorphous PLA as a function of temperature. It is noticeable that amorphous PLA has melting temperatures between 110 and 150°C, which is a desirable thermal property for NFFP production, once it is possible to have suitable viscosity under 200°C. In contrast, semicrystalline PLA physical behavior over temperature (Figure 14) shows that melting point can range up to 207°C, slightly above the ideal processing temperature for PF. These different temperatures for melting points between amorphous and semicrystalline PLA are, as already mentioned, related to the content of L lactide on their polymeric structures [61].

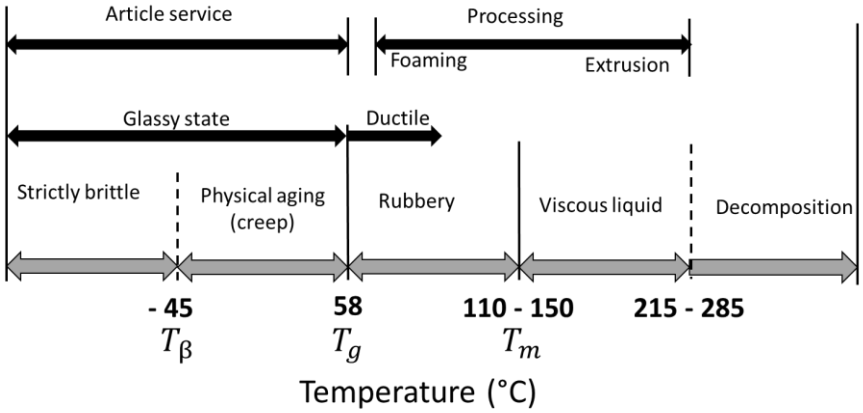

Figure 13- States of amorphous PLA as a function of temperature (Adapted from [61]*).*

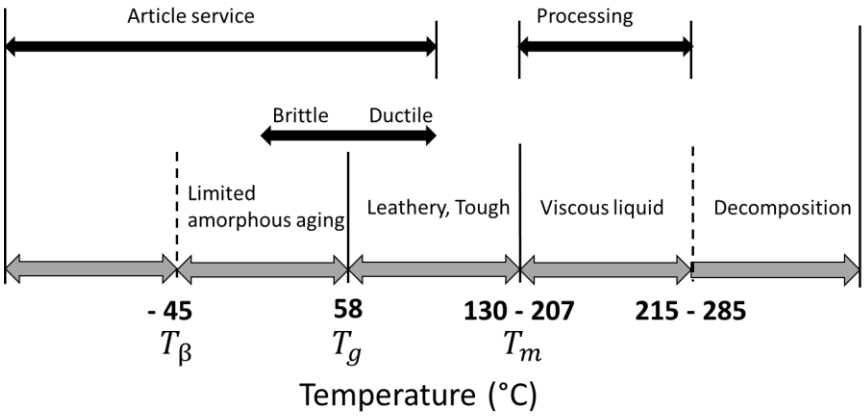

Figure 14- States of semicrystalline PLA as a function of temperature (Adapted from [61]*).*

The drawback of glass transition temperature (T_g) that gives PLA limitations on its applications is well visible in both diagrams (Figure 13 and Figure 14). In both structures the T_g is pointed to be the same, but with quite different behaviors above. Since amorphous PLA is considered better for NFFP applications due to its processability at lower temperatures, its mechanical properties may be compromised right above ≈58°C, related to a rubbery state. An understanding of temperature interval between T_β and T_g is also important, mainly because within this interval, aging occurs, which gives PLA a tendency for brittle fracture, but although PLA is typically brittle in this temperature interval, amorphous PLA can exhibit either ductile or brittle fracture in this region [61].

Table 3 contains a few PLA grades used in NFFP filaments and it is visible that 4032D and 4043D grades are more frequently used. These are suitable grades for extrusion processes (Figure 15).

Table 3- Few PLA grades used in NFFP filament production

PLA grade	Fiber used	Ref.
4032D	Rice Husks	[12]
4043D	Wood flour	[30]
4032D	Wood flour	[35]
2003D	Kraft pine lignin	[54]
4032D	Hemp	[62]
3260HP	Flax	[63]
3001D	Microcrystalline Cellulose	[64]
4043D	Kraft lignin	[65]
4032D	Cork	[66]
4043D	Cellulose nanocrystals	[67]

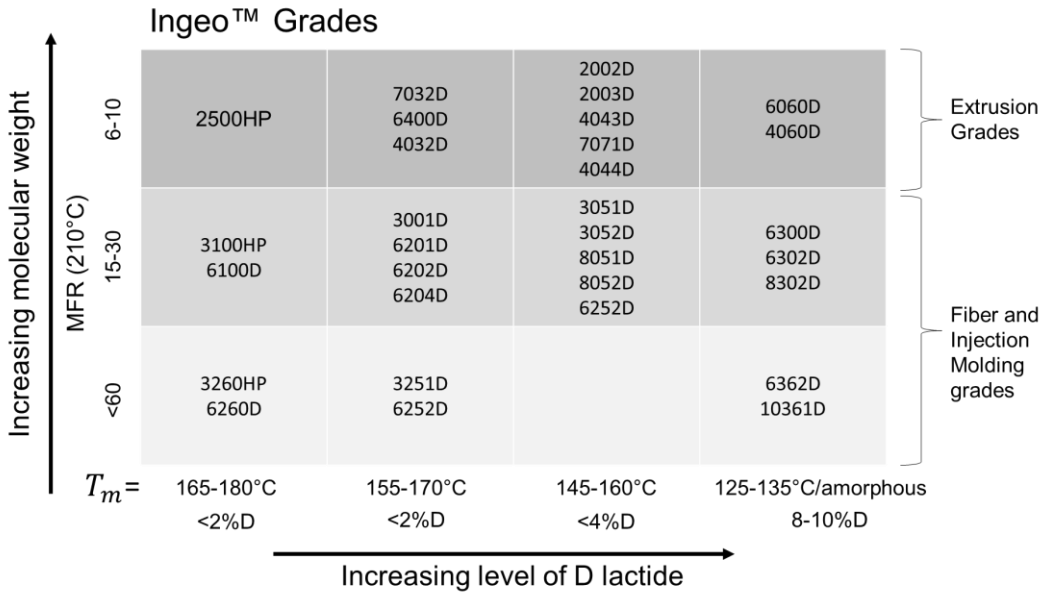

Figure 15- Ingeo PLA grades from NatureWorks and their viscosities and D lactide content (Adapted from [68]).

Analyzing Table 3 and Figure 15, it is evident that an increase in D lactide content decrease T_m, which lead to the conclusion that between the most used grades (4032D and 4043D), 4043D has the one that has lower melting temperatures due to his higher content of D lactide.

2.2.2. Extrusion of NFFP filaments with PLA as a matrix

In a brief description, the extrusion process is an operation that gives form to a material in a molten state by forcing it through a restriction/die [69]. Extrusion is a continuous process that uses an extruder to perform all the processes such as transport, melt, mixing and compression of particulates [69]. These extruders can have a single-screw (Figure 17) or co-rotational twin-screw (Figure 18) design, where a twin-screw extruder (TS) is usually the best option to ensure good distribution of fibers in the matrix [6],[55]. Despite many authors stating that co-rotational twin-screw extruders are more effective than single-screw (SS) extruders when working with composites, many advances on the single-screw design over the past years have been made SS extruders suitable for composite extrusion [56]. SS extruders also have the same modular construction (as twin-screw) of the barrel, which allows different temperatures along the process and their potential for mixing and economic gains has been often overlooked [56].

Whether extruding composite or non-composite materials, mixing is one of the most complex and decisive variables of the process that directly affects the quality of the obtained material [69]. There are two types of mixing: Dispersive mixing; and distributive mixing. Distributive mixing is used to alloying plastics, pigment dispersion and nonreinforcing fillers mixing; And distributive mixing is used with fibers, reinforcing fillers and shear sensitive materials [55].

When filling PLA with PF to produce filaments for AM, the process of extrusion is in the distributive mixing field and it is possible to be done with an SS extruder. However, the screw design (Figure 16) is decisive to achieving a good distribution of the fibers within the matrix.

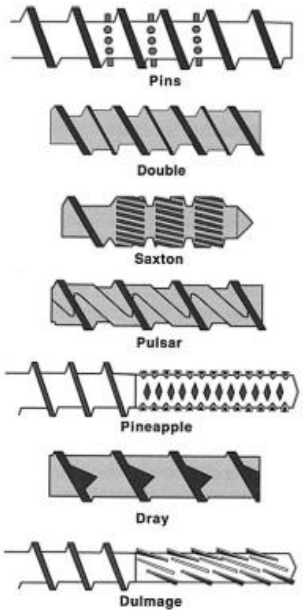

Figure 16- Single-screw distributive mixers types [55].

The pineapple design (Figure 16), which was the one used in this work (Figure 19b), has a good overall rating in dispersive mixing and adequate splitting /reorientation of the fibers should be expected [55]. Several authors also refer to the L/D ratio as being decisive in mixing as well as material quality and whether a twin or single screw; the L/D ratio influences the following extrusion process aspects [55]:

- Mixing capacity;
- Pressure right before the die;
- Material melting capability;
- Barrel conductive heat transfer to processed material.

Figure 17 is a schematic view of a SS extruder with 3 distinct geometric sections. These geometric sections are the material processing sequences and the compression section in some SS extruders is divided into more sections to have a gradual depth decreasing of the channel, thus melting the materials more uniformly. These sections work as following described [69]:

- **Feed Section:** With a greater fillet height of the worm thread, its function is to maintain a high material transport capacity through the barrel.
- **Compression section:** The temperature of the particulate solids mixture increases by conduction while materials are compressed against the walls of the heated barrel, leaving the mixture in a molten state (viscous fluid).

- **<u>Metering section:</u>** The height of the thread pitch is already small and constant. The material is in an ideal molten state and is compressed against the die, obtaining the filament outside the extruder die.

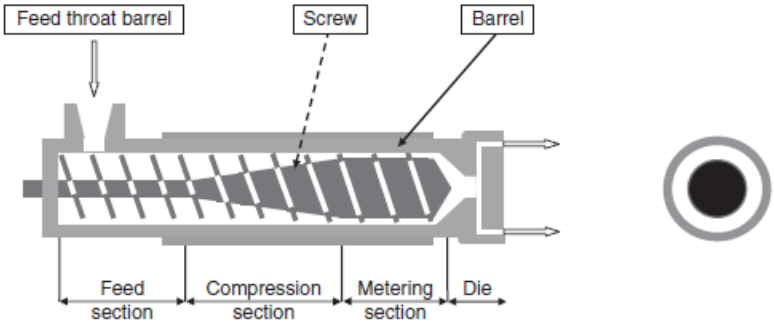

Figure 17- Schematic view of a 'monobloc' one-stage single screw extruder [69].

As already mentioned, the twin-screw extruder leads to a better quality in the filament obtained due to guaranteeing a better distribution of the fibers in the matrix. In this type of extruder (Figure 18), the height of the fillet is constant and the mixture of materials is optimized by combining different pitch dimensions, changing the direction of the thread along with the different screw modules. The interlocking of the screws (Figure 12) in co-rotation is responsible for creating intense mixing conditions.

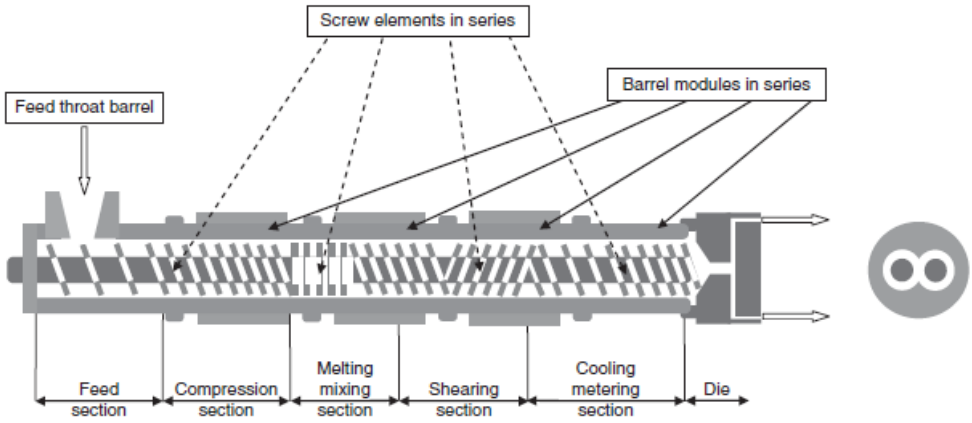

Figure 18- Schematic view of a modular twin-screw extruder [69].

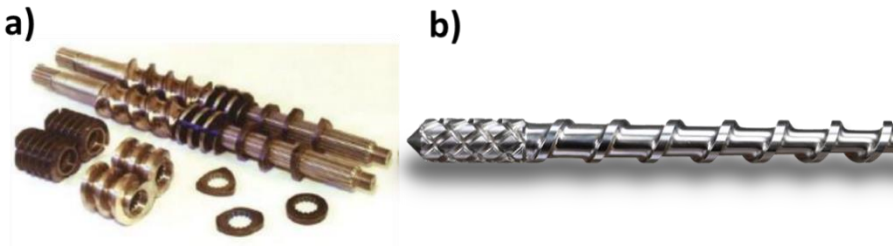

Figure 19- a)Interlocking screws of a twin-screw extruder [69]*; b)Screw of a modular single-screw extruder (3Devo® Composer series)* [70].

The modular construction (available in SS extruders) of these extruders (Figure 18) also makes it possible to obtain different temperature levels throughout the process. Each module may also have hatches for vacuum pumps or for placing the reinforcement fibers only in the melting mixing section, which significantly reduces the time the fibers are exposed to the high temperatures of the process.

The extrusion of PLA matrix composite filaments for 3D printing requires adequate material drying before processing, especially when working with NFFP materials. Both PF and PLA are hygroscopic and if the moisture content is too high, the extrusion process can be compromised, resulting in a low-quality filament obtained. Apart from drying the materials before extrusion, in some cases, using vacuum pumps over the different barrel modules can remove some remaining moisture from PLA and fibers during processing. The effectiveness of using vacuum pumps on filament quality was verified by Depuydt *et al.* [34]. A vacuum pump placed on the extruder's metering section resulted in 0% porosity in PLA/Flax and PLA/Bamboo filaments.

The literature reviewed for this work showed pre-drying procedures varying widely in terms of time and temperature used. However, in most of the works, it was referenced that drying is crucial to obtain printable NFFP filaments.

Table 4 contains parameters used by several works on NFFP filament production and pre-processing drying procedures used. It can be concluded that for NFFP filament extrusion, a printable filament relies on the type of extruder, extrusion temperature profile, extruder screw rotation speed and adequate pre-process drying procedure.

Table 4- Literature review on extrusion parameters and pre-processing drying procedures for NFFP 3D printing filaments production.

Extruder	L/D	Heating zones	Temperature profile [°C] (From feeding to metering)	Screw rotation [rpm]	Compound	Pre-processing drying procedure	Ref.
Twin-screw			170	180	PLA/Rice husk	80°C for 10h	[12]
Twin-screw		5	180;185;190;195;195	9	PP/Rice husk	105°C for 3h	[33]
Twin-screw	36:1	9	165;165;170;175;175;185;185; 200;200	200-350	PLA/Bamboo and PLA/Flax	90°C for 7h	[34]
Single-screw		2	171-175		PLA/Wood flour	103°C for 4h	[35]
Twin-screw	28:1	5	170;175;175;175;180	347	PLA/Hemp	24h until moisture bellow 0.5 wt%	[62]
Twin-screw			165-190	65	PLA/microcrystalline cellulose	8h	[64]
Twin-screw			165-200	120	PLA/Cellulose nanofiber	55°C for 8h	[71]
Twin-screw			170-180		PLA/Chitosan	100-110°C for 8h	[72]

2.3. Additive manufacturing with NFFP

Additive manufacturing encompasses a set of technologies that have in common their work principle: building products by adding very thin layers of material, layer on top of layer [73]. Among them are FDM, stereolithography (SLA), selective laser melting (SLM), selective laser sintering (SLS) and electron beam melting (EBM), which are technologies widely adopted in industries for AM [5]. From these AM technologies, FDM, has been gaining much attention due to its time savings, low cost and flexibility on produced designs [74]. Although 3D printing applications were first used for rapid prototyping and tooling, due to its evolution about cost decreasing of feedstock materials and accuracy improvement, AM is now being used for direct manufacturing rather than prototyping [5]. Moreover, the RepRap project, started by Dr. Gordon in 2005 to make 3D printing technologies accessible for all, was a milestone at the beginning of the personal 3D printing market's growth. From this project, three participants (Bre Pettis, Adam Mayer and Zach "Hoeken") marketed the technology for consumers by founding MakerBot in 2009, which launched on the market one of the first fully assembled consumer 3D printers [73].

Both the personal and professional use of 3D printing is stimulating market growth (Figure 20) and the global 3D market size was USD 12.57 billion in 2020 and is projected to grow from USD 15.26 billion in 2021 to USD 68.71 billion in 2028 [75].

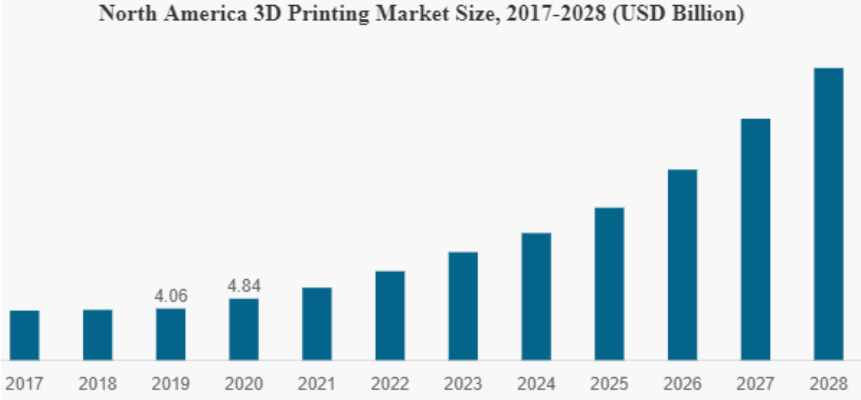

Figure 20- North America 3D printing market size growth (USD Billion) [75].

Along with the market growth, the supply for feedstock has to match the demand and considering that 3D printing uses thermoplastic filaments, this growth will contribute to large amounts of plastic tons circulating all over the globe. Moreover, with the growth in personal use of 3D printing, it will be almost impossible to control the end of life of printed parts. Here, using NFFP filaments with a biopolymeric matrix may mitigate the environmental impact of 3D printing since most of the personal use of 3D printing is not for parts that require high mechanical or thermal performance.

In brief, 3D printing has the potential of sustainable lightweight construction and complex structures fabrication in a single process phase [74].

2.3.1. FDM 3D printers and 3D printing process

FDM 3D printers are classified accordingly to their kinematic mechanism and these printers can have a cartesian (Figure 21a and Figure 21c), delta (Figure 21b), scara, or polar mechanism. However, most of the printers in the market are cartesian or delta and their prices can range from 200 € (e.g., anycubic Kossel (Figure 21b)) for a personal use 3D printer, to ≈200k € (e.g., Stratasys Fortus 450mc (Figure 21c)) for professional printers.

3D printers have all the same nomenclature for the main parts. Figure 22 is a schematic representation of a cartesian printer, where the standard designations used by the 3D community are represented, namely:

- **Print head:** Contains the extruder and may have fans assembled for part refrigeration during printing. The print head has a dependency on the axes and describes the movements given by the printing program (Gcode);
- **Nozzle:** Assembled on the hot-end of the extruder is the die for the melted material;
- **Printed part:** The end product of the 3D printing process;
- **Hotbed:** Often made of glass, it gives a support base for the first layer of the printed part. It can be heated or not;
- **Filament:** Feedstock material for the 3D printing process, usually a thermoplastic or a composite made of a thermoplastic matrix.

Some printers also have an enclosure for chamber heating (Figure 21c) due to some thermoplastics being prone to warpage during the printing process and a heated chamber minimizes that issue.

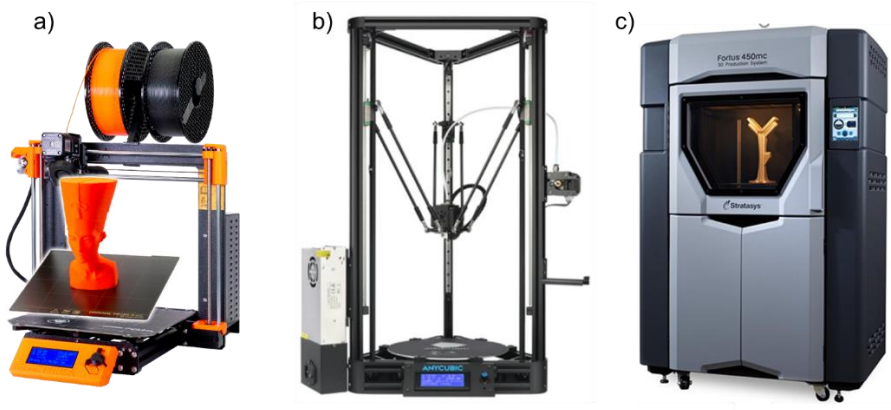

Figure 21- a) Prusa i3 MK3 [76]*; b) anycubic Kossel* [77]*; c) Stratasys Fortus 450mc* [78].

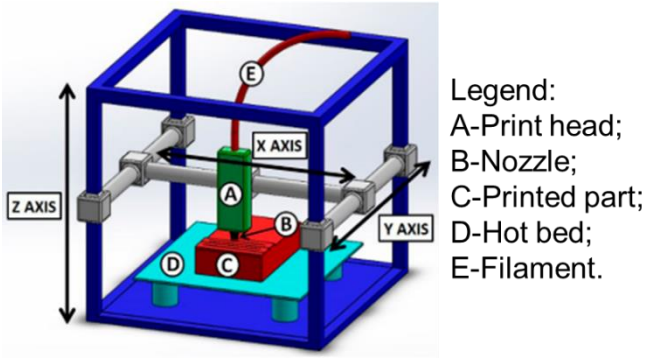

Figure 22- Typical cartesian 3D printer setup (Adapted from [6]*).*

The heart of a 3D printer is the print head (Figure 24). It is where that all the extrusion system is assembled. This is divided into 3 sections [74]:

- **Extrusion mechanism:** It is where the extrusion process is initialized and its function is to ensure a continuous flow of material through the processing channel. A stepper motor is connected to a drive gear, which has direct contact with the filament and compresses it against an idler. The pressure applied should not be too high or insufficient in order to maintain a consistent flow of material.
- **Cold-end:** Has a heat sink (Figure 23) and can be equipped with a fan. Its function is to block the heat flow from the hot-end to escape upwards to the cold section. That is for preserving the filament in a non-melted condition on the section before the hot-end. Furthermore, the non-melted portion of the filament works as a piston pushing the molten material on the hot end through the nozzle.
- **Hot-end:** Contains the heat block and the nozzle (Figure 23), is where the material reaches a molten state and is pushed against the nozzle.

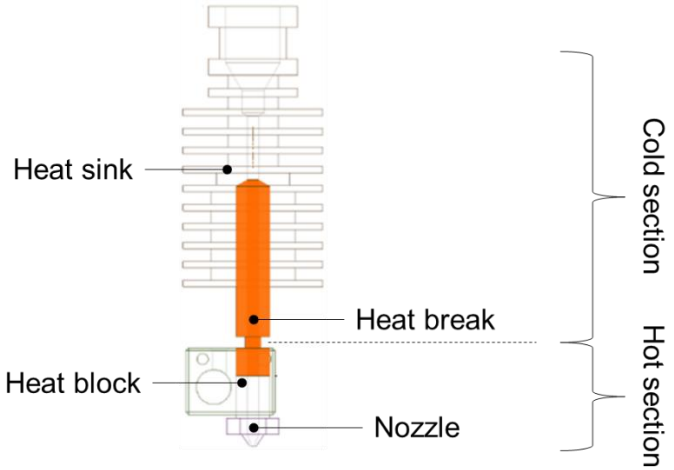

Figure 23- Print head extruder assembly (Adapted from [79]*).*

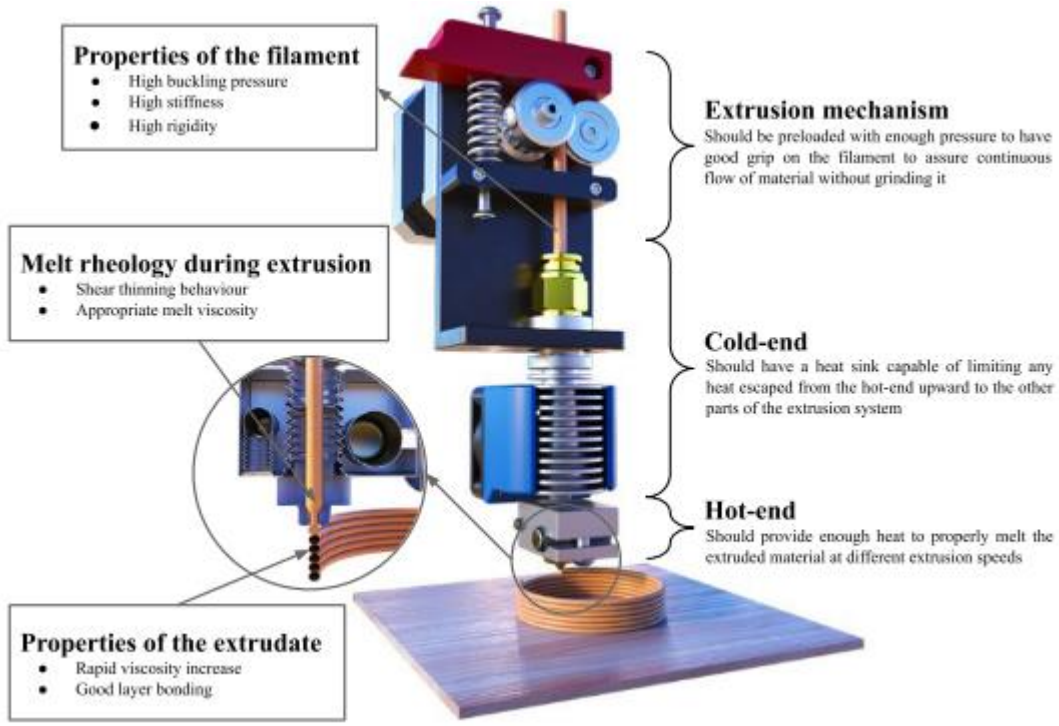

Figure 24- Detailed construction of a print head and required parameter for adequate material extrusion [74].

3D printing is a process (Figure 25) made of several stages and a usual process for printing a part goes as follows:

1. **CAD Design:** The intended part design is modeled in CAD software;
2. **Export to .stl file format:** After the part has been modeled, the final CAD format model is exported to .stl format, a file type that only represents the part surface with triangular planes. Considering that the .stl format is an approximation to the CAD solid, thus it is crucial to ensure a good resolution while converting from CAD to .stl, to achieve good accuracy on the printed part;
3. **Import .stl file into a slicer program:** The .stl file is imported to a slicer program, a common given name for software that will slice in layers the intended part to print. These layers will contain all the trajectories and information needed for the 3D printer controller to give the correct instructions to its mechanism in order to build the part;
4. **Export Gcode from the slicer:** A file in .gcode format is exported from the slicer software into an SD card or uploaded directly by a wifi connection between the printer and the computer. This .gcode file contains all the trajectories as well as the information about extruder geometry, processing and predefined structural factors (Table 5);

5. **3D Printing:** The 3D printer, after having the .gcode file uploaded to their controller, automatically home its axis and start the heating of the nozzle and bed and after that, the part will start to be printed.

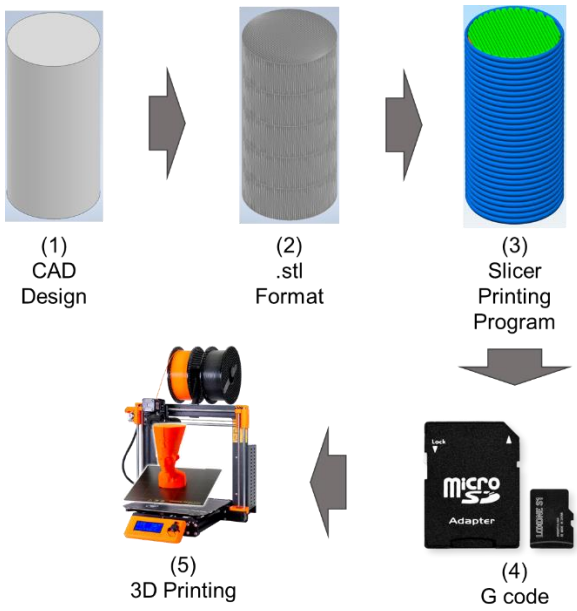

Figure 25- 3D printing process.

Table 5- Printing parameters (Adapted from [14]*).*

	Parameters	Units/description
Extruder geometry	Nozzle diameter	mm
	Filament diameter	mm
Processing	Melt temperature	°C
	Hotbed temperature	°C
	Printing speed	mm/s
Structural	Layer thickness	mm
	Infil geometry (Figure 26)	Rectilinear; Triangular; Grid; Wiggle; Fast honeycomb; Full honeycomb
	Infill density	%
	Number of layers	1, 2, …, n
	Raster angle (Figure 27)	°
	Raster gap (Figure 27)	mm
	Raster/contour width (Figure 27)	mm

Many variables are involved in a single 3D printing process (Table 5) and each one of them affects the printed part's performance. Rather than injected plastic parts, 3D printed parts and their layer-by-layer structure makes this type of product discontinuous and anisotropic by nature [80]. Structural and processing parameters, such as temperatures, infill density, infill geometry

(Figure 26), raster geometries (Figure 27) and layer thickness, are critical for 3D printing end product behavior [81],[82].

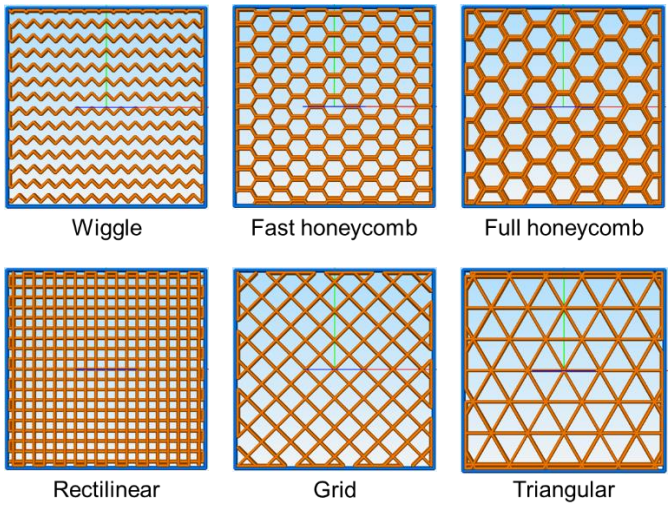

Figure 26- Infill geometries (extracted from Simplify3D®).

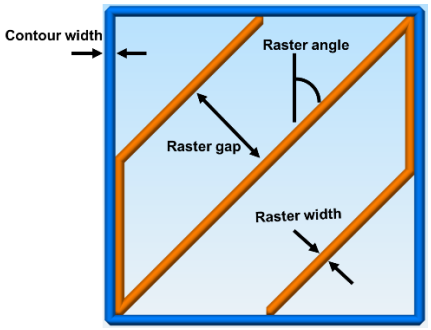

Figure 27- Parameters of nozzle path (extracted from Simplify3D®).

2.3.2. Additive manufacturing of NFFP filaments

As described in the previous topic, the AM process has many variables involved and when printing with NFFP materials, the most critical parameter is the nozzle temperature. This type of filament tends to clog the nozzle at current printing temperatures for the matrix polymer. Thus, it is usual to have working temperatures ≈10°C above the usual printing parameters for neat material. This fact was observed by V. Balla *et al*.[8], while printing TPC/Soybean hull filaments, it was verified that lower printing temperatures resulted in severe nozzle clogging. F. Daver *et al.* [66] reported good printability at 230°C using PLA/Cork filaments, which is a temperature in line with the fact that the printability of NFFP filaments has temperatures above the neat material (PLA usually has working temperatures of 205-220°C [81], [83]). A nozzle temperature of 230°C was also used by M. Kariz *et al.* [20] while printing filaments made of PLA/Wood. However, considering the nozzle temperature parameters from several studies depicted in Table 6, it can be seen that Y. Tao *et al.* [35] had the printing temperature set at 210°C for PLA/Wood flour, but with an

average particle size of 14µm, which is a far smaller size than the particles used by other authors that had printability only with higher temperatures.

Table 6 summarizes relevant printing parameters used by several authors while working with NFFP filaments. It is quite noticeable that the most used filament diameter was 1.75mm and the chosen nozzle diameter in some cases is related to the fiber dimensions. Here, V: Mazzanti *et al.* [6], in a review work, mentioned that for NFFP filaments, although the most common nozzle diameter is 0.4mm, for filled filaments, the nozzle diameter has to increase its diameter.

Table 6- Printing parameters used in NFFP filaments.

Printer	Material (Fiber dimension)	Layer height [mm]	Nozzle Ø and temp. [mm;°C]	Bed temp [°C]	Filament Ø [mm]	Print speed [mm/s]	Ref.
Printrbot	TPC/Soybean hull	0.2	0.5; 220	65	1.75	30	[8]
Zortax M200	PLA/Wood (<0.237mm)	0.19	0.4; 230		1.75		[20]
Shenzen Aurora 603S model	PLA/wood flour (average 0.014mm)		0.4; 210				[35]
LULZBOT 3D	ABS/Wood flour (0.90-0.212mm)		0.8; 245	100	2.75	15	[38]
Da Vinci 1.0 Professional	PLA/Hemp hurd	0.15	0.4; 200	60	1.75	60	[62]
Prusa i3	PLA/Flax (continuous fibers)		1.8; 195	60	1.75	6	[63]
RepRap X400	PLA/Kraft lignin		0.3; 210	60	2.8		[65]
Makerbot Replicator 2	PLA/Cork (average 0.446mm)	0.4	0.8; 230	60	1.75	30	[66]
Divide by Zero	PLA/Chitosan (average 0.025mm)		0.2; 195	80	1.75	35	[72]
	PLA/Bamboo (<0.08mm)		NA-200	60		60	[84]
Prusa i3 MK3S	PLA/Lignin		0.4; 205-230		1.75	35	[85]

2.3.3. Characterization and properties of 3D printed parts made of NFFP materials

The characterization of parts obtained by AM is a research field currently under development. This fact is related to a rapid increase in the use and importance of AM technologies and a lack of specific standardization [80]. Although some standards for AM have already been launched (e.g., ISO 17296; ISO/ASTM 52900) [80], many works use standards used for injection plastics. Accordingly to ISO 10350, which field of application are thermoplastic and thermosetting

materials, reinforced and unreinforced, a correct characterization of the material should contain the following analysis criteria:

- Rheological properties (MVR, MFR);
- Mechanical properties (Tensile, Flexural, Creep, Impact, Compressive);
- Thermal properties (Transition temperatures);
- Other properties (Density, Water absorption).

Mechanical properties of printed parts depend on a wide range of printing and structural parameters (Table 5). The printed part performance can change significantly with the change of only one printing parameter modified [6]. This interdependency of mechanical performance and printing parameters, especially with infill geometries (Figure 26), is already known for unfilled 3D printed materials and NFFP ones are no exception [6]. It is also frequently observed, in several studies, that fiber content increase has a detrimental effect on the mechanical properties of neat materials [35],[66],[84],[86]. Although many papers focus on the mechanical properties, several other factors influence the behavior and performance of printed parts.

Table 7 contains an overview of several papers that studied the properties of NFFP materials on 3D printing, where it is quite visible that an increase in fiber content has a negative effect on tensile strength and Young Modulus.

Table 7- Tensile strength and Young Modulus from several papers entitled with NFFP 3D printing.

Filament compound	Fiber contents [%]	Tensile strength (with fiber content increase)	Young Modulus (with fiber content increase)	Ref.
PLA/Rice husk	20; 30; 40; 50	Decreased		[12]
PLA/wood	5; 10; 20; 30; 40; 50	Increased for 10% wood content	Increased until 40% wood content	[20]
PP/Rice husk	5; 10	Decreased	Decreased	[33]
PLA/Wood flour	5	Decreased		[35]
PLA/Kraft pine lignin	5; 10; 15; 20	Decreased	Increased	[54]
PLA/Cork	5; 10; 20; 30; 40; 50	Decreased	Decreased	[66]
PP/PLA/Bamboo fiber	10; 15; 20; 25; 30	Decreased		[84]
PLA/Wood	10	Decreased		[86]

Although all the papers in Table 7 were carried out to study the 3D printing of NFFP materials, there are two distinct situations. In the studies of F. Daver *et al.* [66] and C. Tsou *et al.* [12], the former produced PLA/Cork filaments and the latter PLA/Rice husk filaments. In both

studies, the material was processed by hot pressing rather than 3D printing, leading to the conclusion that mechanical properties are more affected by the fiber content than the type of process used. In both studies, the hot-pressed materials had high fiber content (up to 50%), yet on the M. Kariz *et al.* [20], the fiber content was also up to 50%, with all test specimens being printed. M. Kariz *et al.* [20] reported increased tensile strength for the printed specimens with a 10% wood fiber content in their PLA/wood filaments. However, the authors also reported that their results were not statistically significant due to the small sample size and large standard deviation.

The fiber content's negative effect on printed parts is verified not only on tensile strength but also on flexural and impact properties. Figure 28 depicts plots from results obtained on 3 different studies on 3D printed NFFP parts. The studies of Figure 28a and Figure 28c showed that an increase of fiber content implies a loss of flexural strength. In terms of impact strength, the results depicted in Figure 28b and Figure 28c also show a loss in impact strength on printed parts at higher fiber contents.

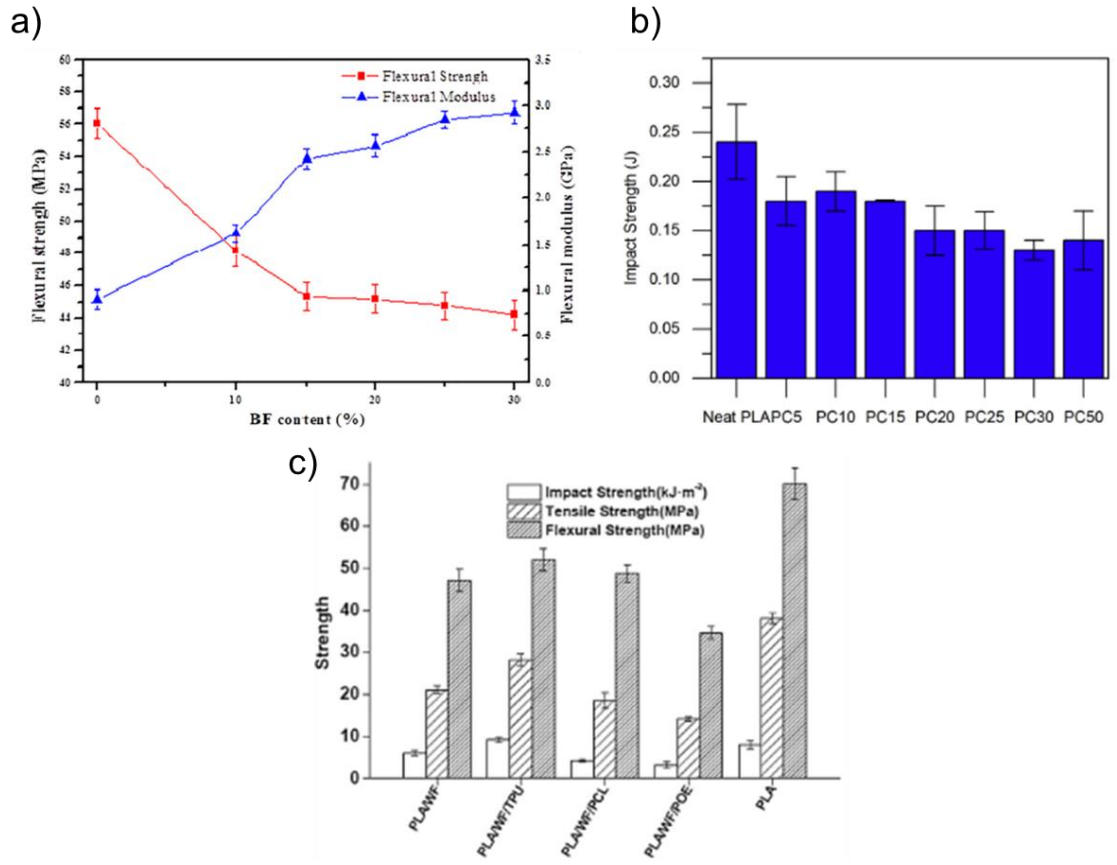

Figure 28- a) PP/PLA/Bamboo fiber printed parts flexural strength [84]*; b)Cork/PLA printed parts impact strength* [66]*; c) Impact, tensile and flexural strength of PLA/wood printed parts*

Density and water absorption are other relevant properties of printed parts. Although biopolymers, such as PLA, are hygroscopic, increased water absorption of printed parts is often linked in many studies to fiber content. C. Tsou *et al.* [12] and M. Morales *et al.* [33] had an increase in water absorption in their works (Figure 29), attributed to fiber content. In terms of

density, M. Kariz *et al.* [20] had a decrease in density (Figure 30), but on their results, it is not very clear if the fiber content caused a change in density properties. In M. Kariz *et al.* work, it is more likely that a decrease in density is linked to the printing process instead of fiber content. When comparing filament density with printed part density (Figure 30), this density decrease can be related to printing parameters used and high raster gaps (Figure 27) since the neat material has the same density loss.

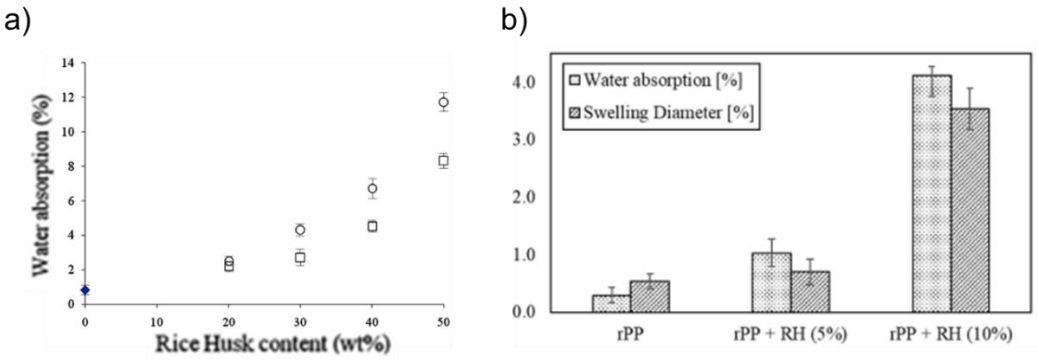

Figure 29- Water absorption of printed parts as a function of fiber content in a) PLA/Rice husk [12]*; b)PP/Rice husk* [33].

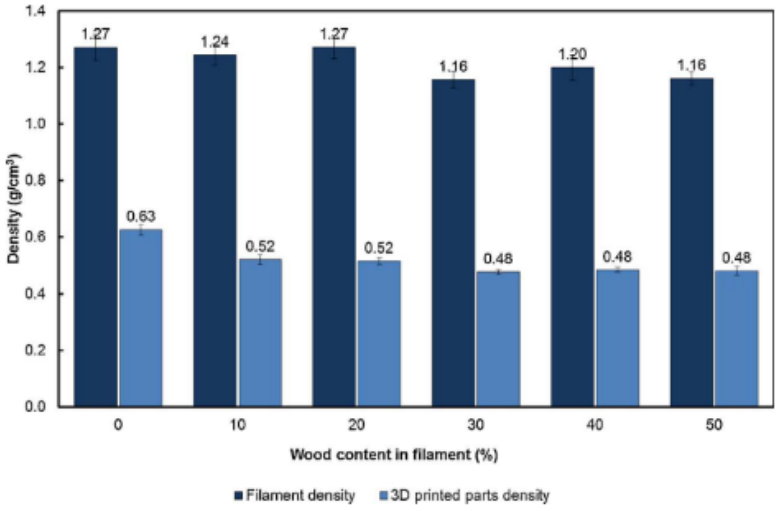

Figure 30- Filament density vs. printed part density as a function of fiber content on PLA/Wood [20].

Chapter 3
Materials and methods

This chapter describes the materials and methods used to produce NFFP filaments made of PLA and RH and all the tests/analyses performed to characterize raw materials, filaments produced and printed parts. The subtopics sequence depicts the order of all the work done.

3.1. Materials

The materials used in this work for all NFFP filament compounds were PLA (Ingeo™ Biopolymer 4043D) and rice husks from Alcácer do Sal, Portugal.

3.2. Fiber preparation and treatment

The RH (rice husks) used in this work were obtained from the rice milling dehusking stage, inherent to this process, there are always rough rice grains and a considerable amount of leaves and stems mixed with the husks (Figure 31 a). The first step of fiber preparation was to separate the husks from all undesirable fibers, grains and impurities. Although decanting is a rudimentary process, it was quite effective in extracting the husks in this work.

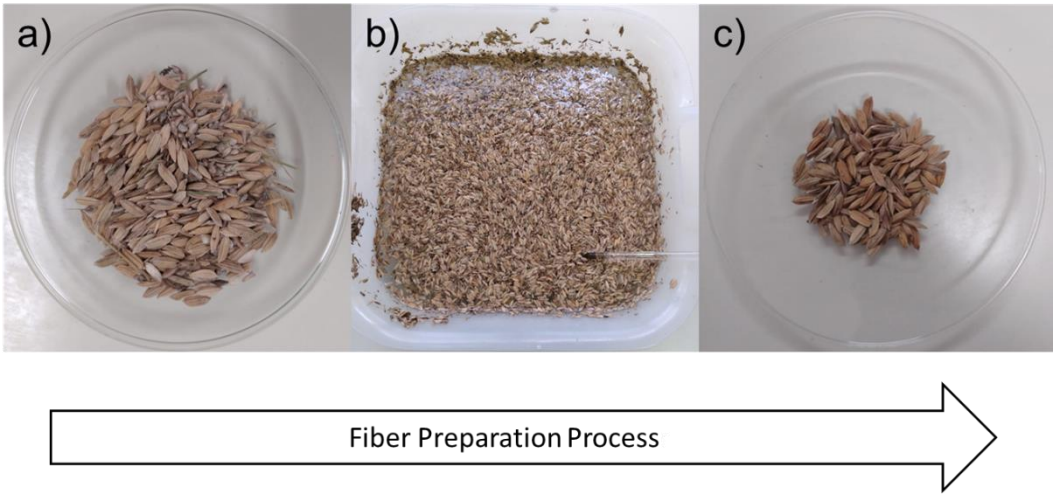

Figure 31- a) Raw material obtained as a subproduct of the dehusking stage.;b) Rice husk extraction by decantation.; c)Clean RH.

As shown in Figure 31b, the raw material (Figure 31a) was immersed in a recipient with water and left to rest for approximately 2h, which was enough to let the husks float in the water. The supernatant material (mainly RH) was then removed using a strainer and dried in a drying oven (Binder® ED115) for 12h. After drying, the RH was sieved (2mm mesh) to remove some remaining impurities, obtaining only RH (Figure 31c). After that, RH was grinded to obtain a powder for a two-stage sieving procedure (Figure 32) to categorize the fiber dimensions.

As shown in Figure 32, the sieving procedure began with a 1mm mesh sieve, where the grinded RH was sieved and the above 1mm size fibers submitted to further grinding and sieving procedure. This operation (regrinding and sieving again) showed a good fiber recovery in terms of initial weight vs.≤0.5mm fibers. The second sieving was with a 0.5mm mesh. The fibers that did not pass through were grinded and sieved again. All categorized fibers were conserved in the convection drying oven at 50°C to prevent moisture absorption before the alkali treatment.

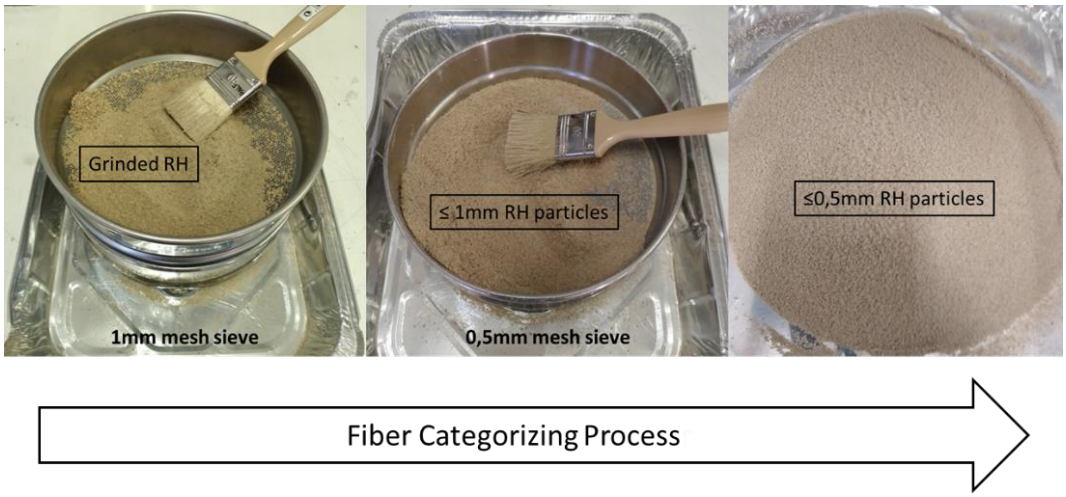

Figure 32- 2 stages fiber categorizing process.

The alkali treatment procedure had 2 stages (Figure 31a and b). As depicted in Figure 31a, in the first stage, RH were immersed in a 5% wt. NaOH solution with a weight ratio of 1:10 for 6h at room temperature. As the RH tends to form clots, the mixture was stirred for 2 min every hour. In the second stage of alkali treatment (Figure 31b), fibers were quickly washed with circulating water to neutralize the pH. For that, RH was washed until the pH reached a value <12 and after citric acid was added in order to obtain a pH of ≈7. All pH measurements were performed with an Adwa® AD1020 professional multi-parameter bench meter. After pH normalization, the fibers were washed, filtered and dried in a drying oven for 12h at a temperature of 60°C. All treated and dried RH followed the sieving procedure from Figure 32 to ensure all fibers maintained the <0.5mm dimension and were vacuum-sealed to prevent moisture absorption.

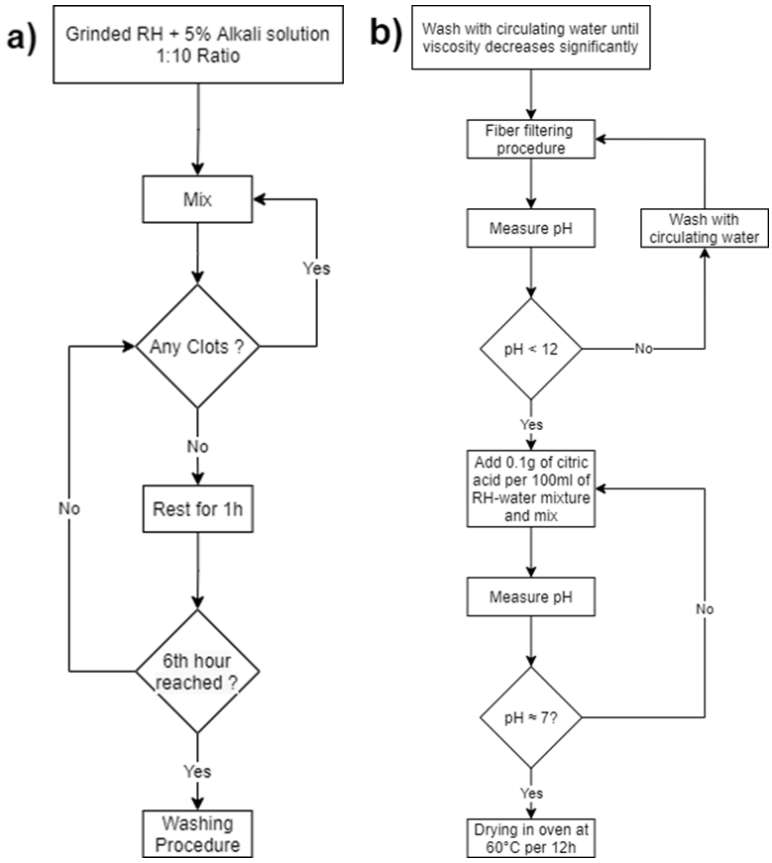

Figure 33- a)Alkali treatment procedure; b)washing procedure.

3.3. Filament extrusion

The PLA 4043D pellets were first dried at 80°C for 4h in a drying oven. Using a plastic recipient, formulations with 5, 10, 15 and 20 wt.% of RH were blended. As a result of adequate material drying, the RH showed good adhesion to the PLA pellet's surface (Figure 34b). The filaments with 0, 5, 10, 15 and 20 *wt.*% of RH and 1.75mm of diameter were extruded in a single screw 3Devo® composer 450 desktop extruder (Figure 34a).

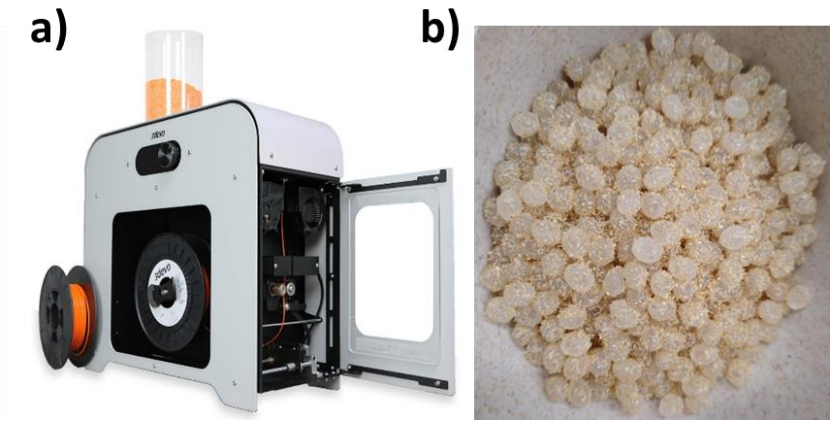

Figure 34- a) 3Devo® composer 450 desktop extruder; b)5 wt.% formulation after mixing in a plastic recipient.

The 3Devo 450 desktop extruder has 3 compression sections, 1 metering section, 4 heater zones (Figure 35) and a PID controller for filament diameter (puller), spooling and winding. This filament extruder presented a reasonably good behavior processing the material formulations used in this work and after a few trial-and-error adjusting heating temperatures and extrusion screw velocity, the optimum extrusion profile for all blends was 175°C; 180°C; 190°C; 180°C for the heaters setpoints, and a screw velocity of 4rpm (Figure 35). As mentioned, diameter control (puller), spooling and winding velocities were automatic. The cooling fans velocity and direction were revealed to be critical variables of the process. As shown in Figure 36a, the outlet of the colling fans must slightly diverge from the hot filament exiting the die and have their velocity set to 40%, allowing that the filament does not cool too quickly, maintaining a rubbery state. This rubbery state significantly improves the diameter variance since the puller (Figure 36a) can easily correct the diameter, as the material is still deformable. The filament indicated a proper processing temperature when it was almost at the desired diameter before the puller (Figure 36b).

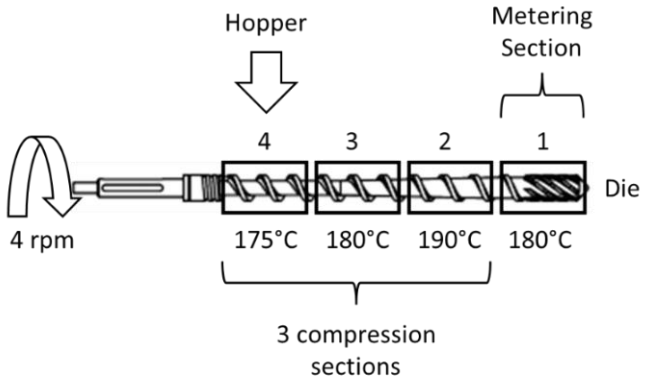

Figure 35- Schematic overview of the extruder screw and extrusion profile applied.

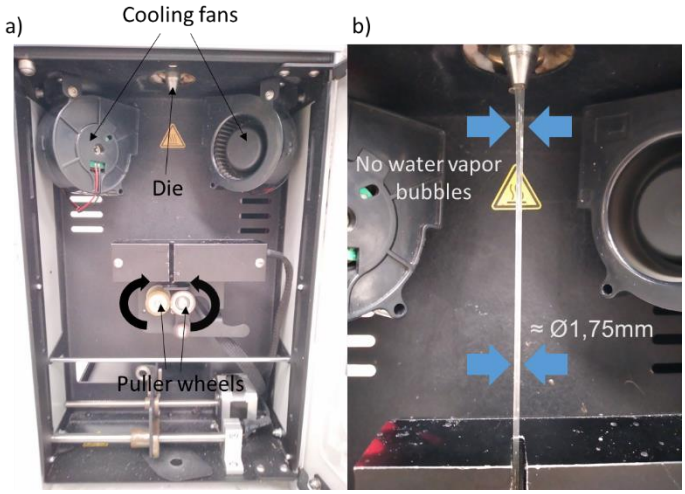

Figure 36- a) filament puller system; b)Ideal extrusion conditions.

3.4. 3D printing of specimens

Specimens for tensile, compressive and flexural tests (Figure 37) were printed on a Prusa® i3 Hephestos 3D Printer (Figure 38). Specimens geometries were given by the standards used (Figure 37). The .stl files were created on Dassault 3D experience and the .gcode files with printing profiles were programmed on Simplify 3D®, a professional 3d printing software. Except for ASTM D695-45°, all specimens were printed in a flat position (Figure 40) and the printing parameters used in all prints are detailed in Table 8. Each specimen batch was printed as a function of infill printing direction (Figure 39) for further analysis of printing direction influence on the material properties. Printed specimens were identified according to their fiber content and printing direction in the following way: X% RH-Y° where X is the % wt. of fiber and Y is the printing direction.

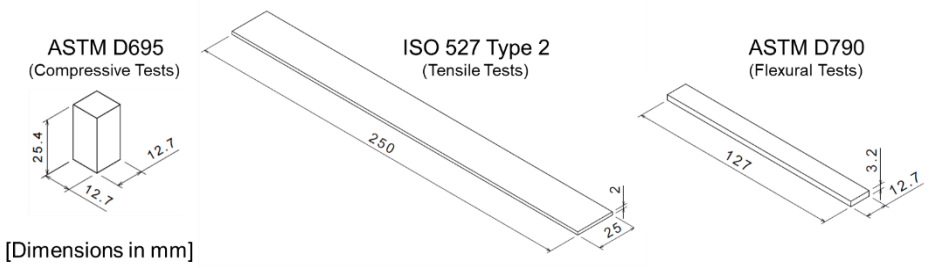

Figure 37- Mechanical properties test specimens modeled in Dassault 3D experience.

Figure 38- Prusa® i3 Hephestos 3D printer.

Table 8- Printing parameters

Nozzle diameter	0.8 mm
Layer height	0.4 mm
Number of perimeter shells	2
Printing speed	1800 mm/min
Nozzle temperature	220°C
Heated bed	No
Infill printing directions	0°; 45°; 90°

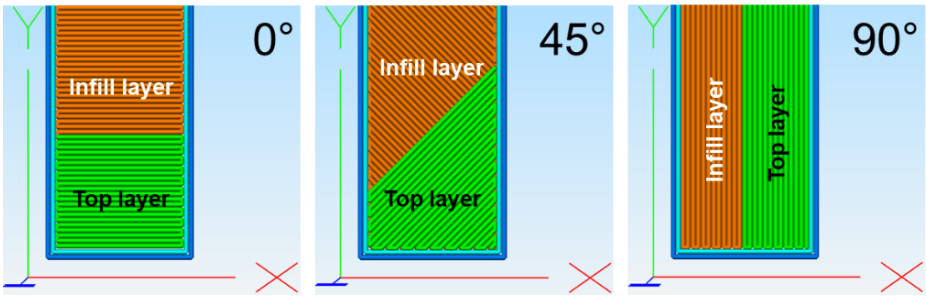

Figure 39- Simplify3D® top views of printing directions used.

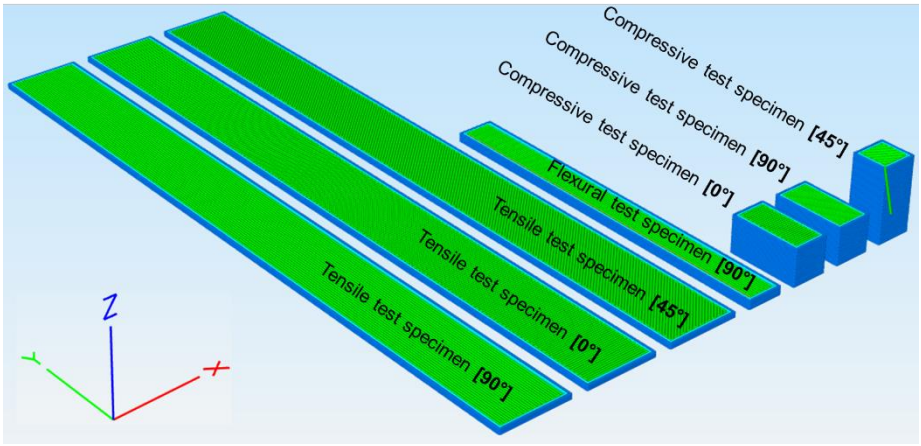

Figure 40- Printing orientations of specimens (extracted from Simplify3D®).

The printhead had some changes to allow the printer to handle this type of filaments. The nozzle and the heat break were machined and the gear was changed (Figure 41). Prusa 3D printers use mk8 type hotend parts that usually have 2 mm of hole diameter and in this case, the nozzle and heatbreak (including the Teflon) were drilled to a diameter of 2.4mm.

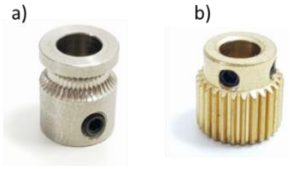

Figure 41- a) Type MK8 feeder pulley (old); b) Type MK8 26 tooth feeder gear (new).

3.5. Water absorption

Water absorption (WA) of printed parts was calculated accordingly to equation 1, using samples with a volume of 10x10x2 (mm^3) trimmed from ISO 527 90° printed specimens. The samples were weighed (in an A&D® EK-1200gx0.1g compact balance) before and after being immersed in distilled water for 24h at room temperature. From each printed blend, 5 samples were analyzed.

$$WA(\%) = \frac{W_1 - W_0}{W_0} \times 100 \quad (1)$$

Where:

W_0 - Initial weight of the sample (after drying for 24h at 40°C in a drying oven);

W_1 - Weight of the sample after 24h in distilled water.

3.6. Density

Densities of printed parts, filaments and PLA pellets were determined by Archimedes principle. RH density values were obtained in a pycnometer (Quantachrome® Ultrapycnometer 1000) with 5 measurements. For the density determinations, an analytical balance (A&D® GR-200-EC) and a density determination kit (A&D® AD-1653) were used along with a 300ml beaker containing distilled water (at room temperature). After all weighings (Table 9), density values were obtained using the following equation:

$$\rho = \frac{A}{A - B} \quad (2)$$

Where:

A - Weight of sample in air;

B - Weight of sample in liquid.

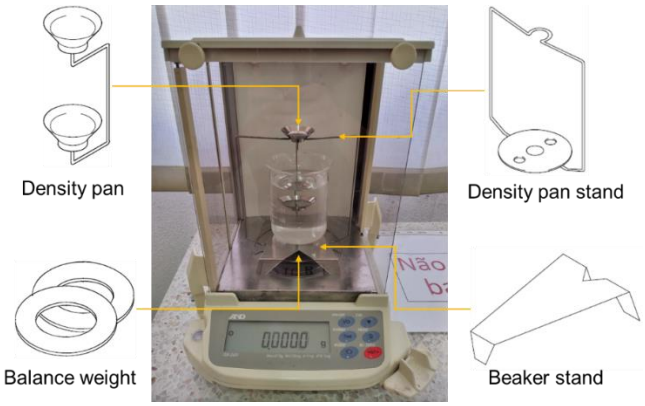

Figure 42- A&D® GR-200-EC analytical balance with A&D AD-1653 density determination kit mounted.

Table 9- Samples measured for densities determination.

Sample	Number of samples
Filaments	
0% RH	5
5% RH	5
10% RH	5
15% RH	5
20% RH°	5
Compressive test specimens	
0% RH-90°	5
0% RH-45°	5
0% RH-0°	5
5% RH-90°	5
5% RH-45°	5
5% RH-0°	5
10% RH-90°	5
PLA	
PLA pellets	20

3.7. SEM (Scanning Electron Microscopy)

SEM images from fracture surfaces (tensile and flexural tests), filaments and RH fibers, were acquired in a Hitachi® S-2400 scanning electron microscope (Figure 43) using an acceleration voltage of 20kV and a magnification ranging from 20 to 400x. Previously the samples were coated with Au-Pd alloy.

Figure 43- Hitachi® S-2400 scanning electron microscope.

3.8. FTIR (Fourier Transform Infrared Spectroscopy)

FTIR-ATR spectra of RH before and after NaOH treatment were obtained using a Perkin Elmer (Figure 44), Spectrum Two, FTIR spectrometer equipped with a UATR Two accessory, at 4 cm^{-1} resolution and eight scans of data accumulation.

Figure 44- Spectrum Two FT-IR Spectrometer, PerkinElmer® [89]

3.9. TGA (Thermal Gravimetric Analysis) and DTG (Derivative Thermogravimetry)

The analysis of all materials was conducted under a nitrogen atmosphere (200 ml/min) using a Hitachi® STA7200 Thermal Analysis System equipment (Figure 45), at a temperature increase rate of 10 C/min (until 600°C).

Figure 45- Hitachi® Thermogravimetry/Differential Thermal Analyzer STA7200RV [90].

3.10. Tensile tests

Tensile tests were performed in a Impact® E-Series – TS 300 servo-hydraulic UTM (Figure 46a), equipped with a load cell of ±50kN and an axial extensometer with a nominal length of 50mm.

a) b)

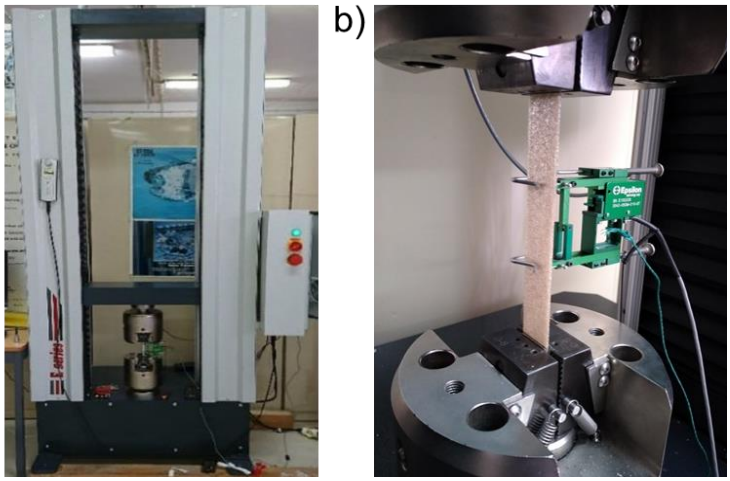

Figure 46-a) Impact® E-Series - TS 300 testing machine; b)Tensile test assemble.

All tests (Table 10) were conducted under ISO 527 – 4 standard (Test conditions for isotropic and orthotropic fiber-reinforced plastic composites), which determines that for measuring maximum elongation and tensile Modulus of elasticity, test speed should be 2mm/min. Data from the tests were acquired with Lightest® software (version 2.1.66) and the geometry of the samples used was type 2 (Figure 37). Printed specimens were tested (Table 10) at room temperature. Values for Young modulus, yield stress, ultimate tensile stress (UTS) (Figure 47) and elongation at break (Figure 47) were determined. Stress-strain curves were obtained by plotting the values from equation 3 and equation 4 and the young modulus was calculated accordingly with equation 5. The yield stress was determined graphically by the 0.2% offset method (Figure 47).

$$\sigma = \frac{F}{A} \tag{3}$$

Where:

σ- Stress [MPa];

F- Load [N];

A- Specimen cross-sectional area [mm²].

$$\varepsilon = \frac{\Delta l}{l_0} \tag{4}$$

Where:

Δl- Length variation [mm];

l_0- Initial length of the specimen [mm].

$$E = \frac{\sigma'' - \sigma'}{\varepsilon'' - \varepsilon'} \tag{5}$$

Where [87]:

E- Young modulus [MPa]

ε'=0.0005;

ε''=0.0025;

σ'=Stress value for ε' strain [MPa];

σ''=Stress value for ε'' strain [MPa].

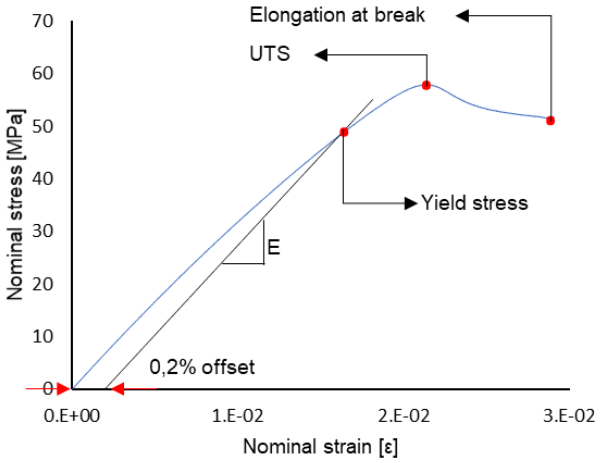

Figure 47- Yield stress by the 0.2% offset method, ultimate tensile strength (UTS) and elongation at break.

Table 10- Number of tensile specimens tested.

Specimen	Number of tested specimens
0% RH-90°	5
0% RH-45°	5
0% RH-0°	5
5% RH-90°	5
5% RH-45°	5
5% RH-0°	5
10% RH-90°	5
10% RH-45°	3

3.11. Compressive tests

Compressive tests were conducted in an Instron® 1342 electro-mechancial UTM (Figure 48), equipped with a ±250kN load cell and a stroke of ±75mm. The tests were performed accordingly to ASTM D695 standard (Test method for compressive properties of rigid plastics) and as determined by the standard, speed control was set at 1.3mm/min.

a)  b) 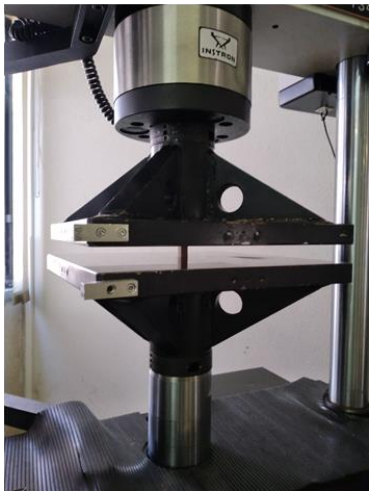

Figure 48- a) Instron® 1342 servo-hydraulic UTM; b)Compressive test assemble.

Specimen geometry used was prismatic, as detailed in Figure 37. Apart from speed control, tests were set to a displacement of 25% of the sample height (6.35mm). Data from tests were acquired with National Instruments® Labview® 7 express software. Printed specimens were tested (Table 11) at room temperature. Values for Young modulus and yield stress were determined. Stress-strain curves were obtained by plotting the values from equation 6 and equation 7. Young modulus and yield stress were determined graphically. For the yield stress and accordingly, to the ASTM D695 standard, toe compensation was taken into account and the 0.2% offset method was applied to the compensated straight line (Figure 49).

$$\sigma = -\frac{F}{A} \tag{6}$$

Where:

σ- Stress [MPa];

F- Load [N];

A- Specimen cross-sectional area [mm²].

$$\varepsilon = -\frac{\Delta h}{h_0} \tag{7}$$

Where:

Δh- Height variation [mm];

h_0- Initial height of the specimen [mm].

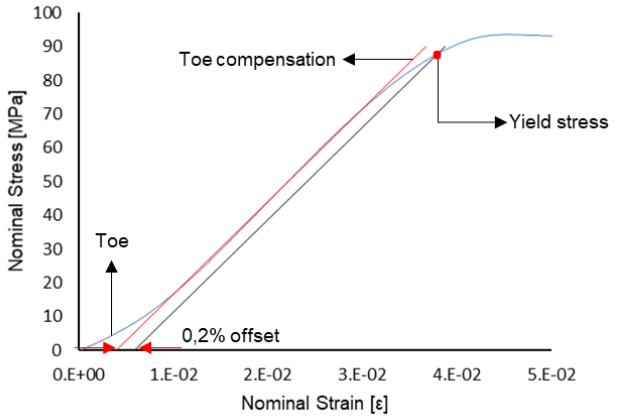

Figure 49- Yield stress determination with toe compensation and by the 0.2% offset method.

Table 11- Number of compressive specimens tested.

Specimen	Number of specimens
0% RH-90°	5
0% RH-45°	5
0% RH-0°	5
5% RH-90°	5
5% RH-45°	5
5% RH-0°	5
10% RH-90°	5

3.12. Flexural tests

Flexural tests were performed on the same equipment as the tensile tests (Figure 46a). The flexural test assembly is depicted in Figure 50.

Figure 50- Impact® E-Series - TS 300 testing machine, flexural test assembly.

All tests were conducted under ASTM D790 standard (Flexural properties of unreinforced and reinforced plastics and electrical insulating materials), test speed was set to 5mm/min and rotatable supports for the test specimens were used, with a span of 60mm. Printed specimens (Table 12) were tested at room temperature. Flexural modulus (equation 8) and maximum flexural stress (equation 9) had their values determined. For the bending modulus of elasticity, the test data values were plotted to obtain a slope (**m** from equation 8) from the load-deflection curve for further modulus determination.

$$E_B = \frac{L^3 m}{4bd^3} \tag{8}$$

Where [88]:

E_B- Modulus of elasticity in bending [MPa];

L- Support span [mm];

b- Width of tested beam [mm];

d- Depth of tested beam [mm];

m- Slope of the tangent to the initial straight-line portion of the load-deflection curve [N/mm]. (Graphically determined).

$$\sigma_f = \frac{3PL}{2bd^2} \tag{9}$$

Where [88]:

σ_f- Stress in the outer fibers at midpoint [MPa];

P- Load at a given point on the load-deflection curve [N];

L- Support span [mm];

b- Width of tested beam [mm];

d- Depth of tested beam [mm].

Table 12- Number of flexural specimens tested.

Specimen	Number of tested specimens
0% RH-90°	5
5% RH-90°	5
10% RH-90°	5

Chapter 4
Results

This chapter contains results obtained for filaments printability, their densities and raw material densities and morphologies. Densities and water absorption values for printed parts are also shown. Furthermore, the processed materials chemical structures and thermal stability are analyzed and the mechanical properties of the printed specimens are reported.

4.1. Fiber morphology

Whole husks show two different textures (Figure 51a). On the interior side of the husk (Figure 51c and Figure 51e), the husk has a smoother surface, showing almost no roughness and on the exterior side (Figure 51b, Figure 51d and Figure 51f), the husk has a rough texture with a well-defined pattern. Detail from Figure 51c shows some defibrillation on the interior side of the husk and Figure 51a reveals some cracks on both sides. These cracks have different sizes and at higher resolutions (Figure 51f), it is visible that several crack initiation points are characterized by being located at the husk pattern divisions at the outer side.

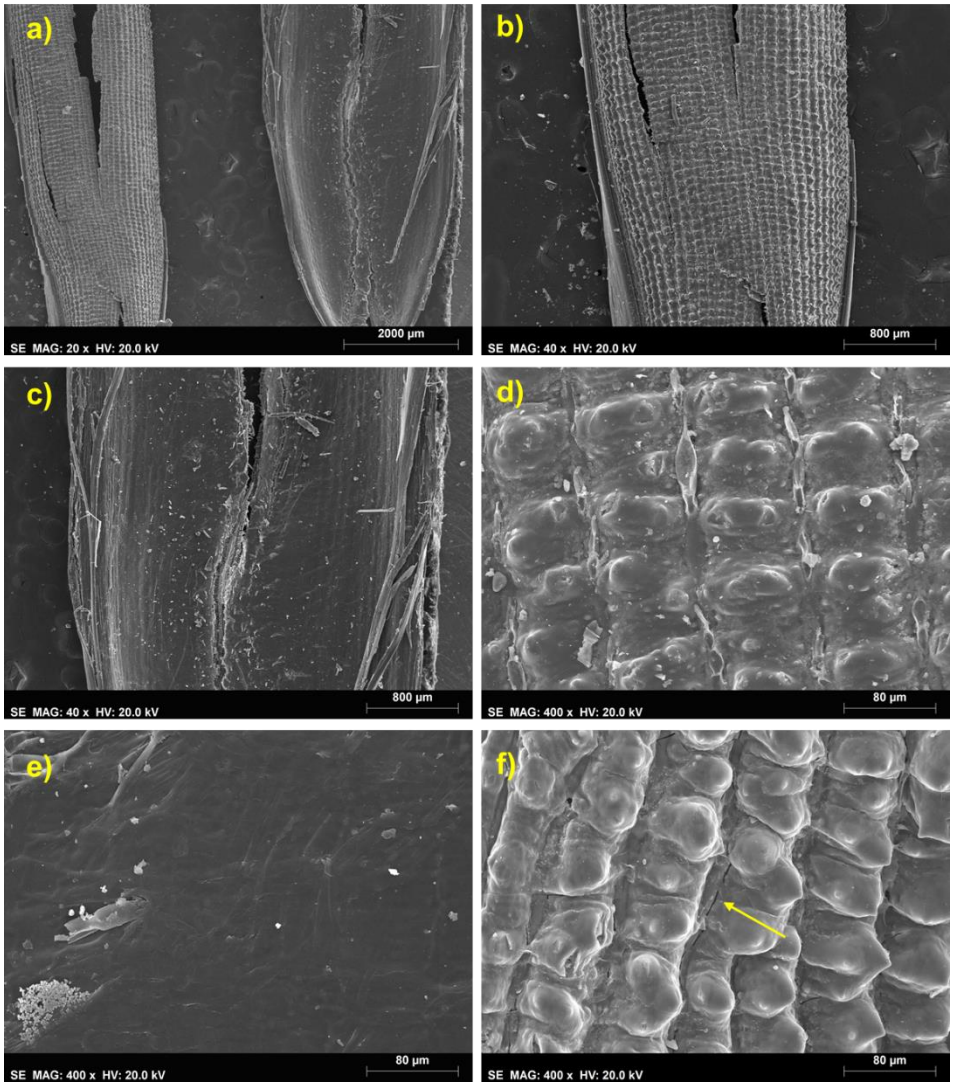

Figure 51- SEM images of: a) Whole RH, inside and outside.; b) Whole RH outside texture.; c) Whole RH inside texture.; d) Whole RH outside texture detail.; e) Whole RH inside texture detail.; f) Whole RH outside detail.

The grinded husks are a heterogeneous material (Figure 52a and Figure 52c) and although sieved, different sizes and shapes still characterize the material. Fibers show delamination of their surface and it can be visualized in Figure 52b and Figure 52d that elongated hollow fibers form husks. There are no visible changes in the surface texture between treated and untreated fibers.

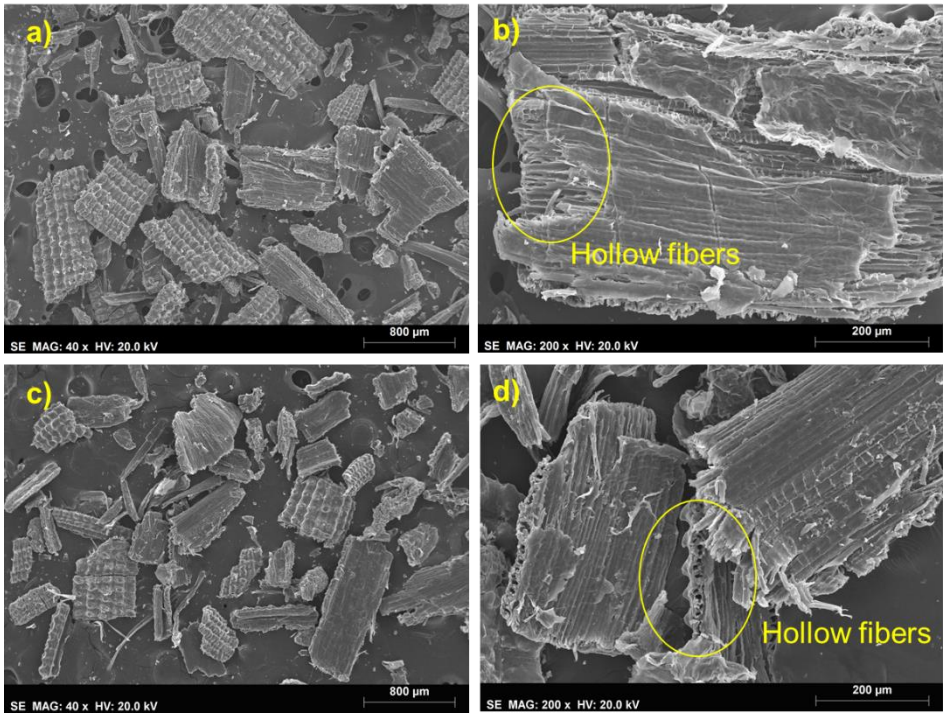

Figure 52- SEM images of: a) Grinded and sieved untreated RH.; b) Grinded and sieved untreated RH detail.; c) Grinded and sieved alkali-treated RH.; d) Grinded and sieved alkali-treated RH detail.

4.2. Filament and printability

The obtained filaments are given in Figure 53. The incorporation of fiber had increased the filament roughness and diameter variation. Figure 54b and SEM images of Figure 55 show that the roundness and diameter variation is proportional to fiber content increase. The fiber agglomerations induced high diameter variation for the filaments of 10%, 15% and 20% RH content.

Issues in printability were found for the 10% RH, 15% RH and 20% RH filaments. The 15% RH and 20% RH blends were revealed to be too brittle to hold the forces applied by the extruder feeder pulley. The 10% RH blend had constant nozzle cloggings (even at temperatures above 220°C) and showed a tendency to fracture before the extruder pulley (Figure 55). Consequently was not possible to produce the same amount of samples as the 0% RH and 5% RH due to the unfeasibility of constantly disassembling the printhead to solve nozzle clogging issues.

The 5% RH filament, which had few diameter variations, showed no nozzle cloggings or other significant issues and all printed specimens were produced without any supervision of the process. The printability of 0% RH filament was similar to the printability of average commercial PLA filament. Some produced specimens are given in Figure 57.

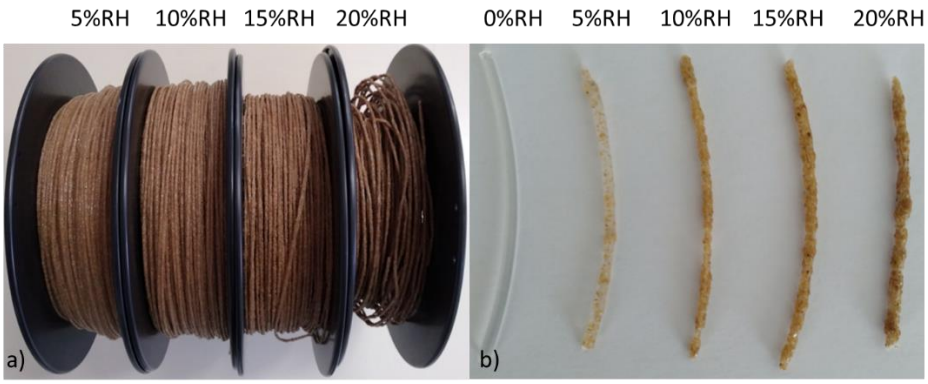

Figure 53- a) Composite filament spools produced; b) Filaments produced.

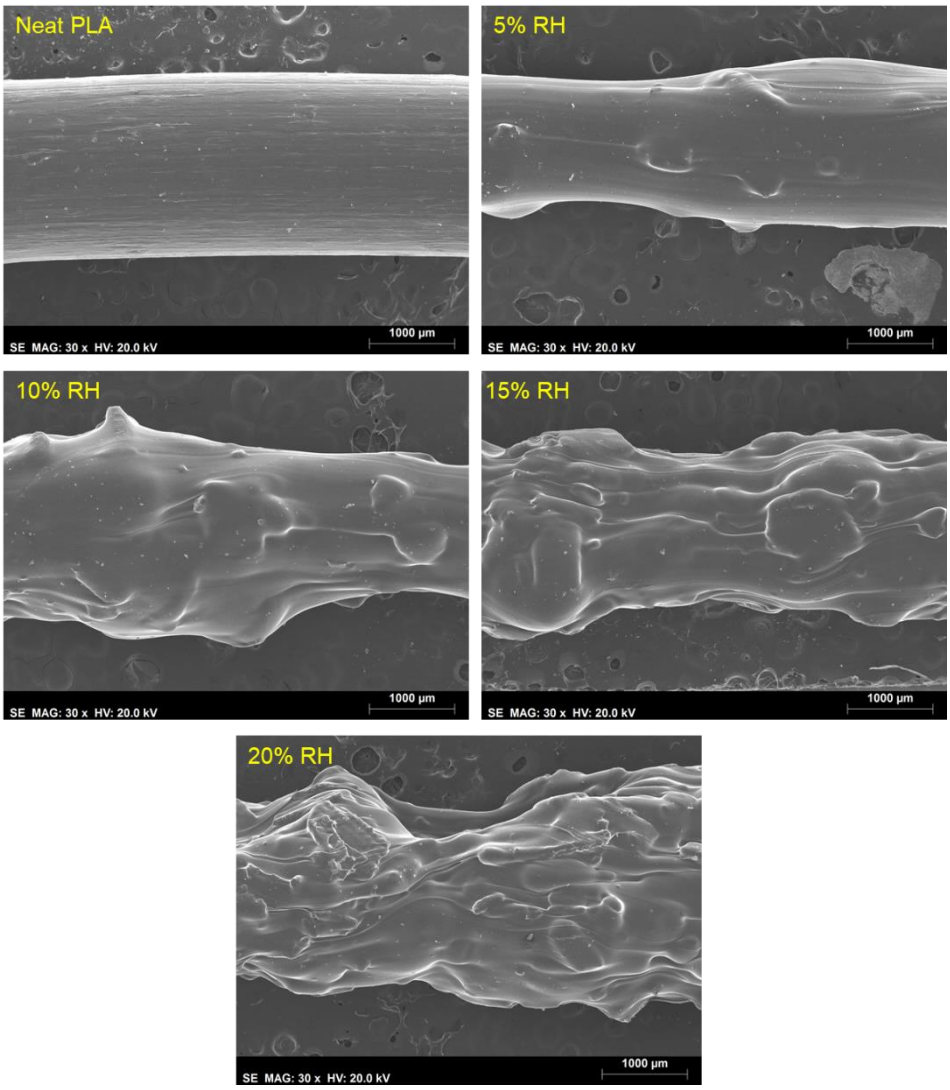

Figure 54- SEM images of filaments produced.

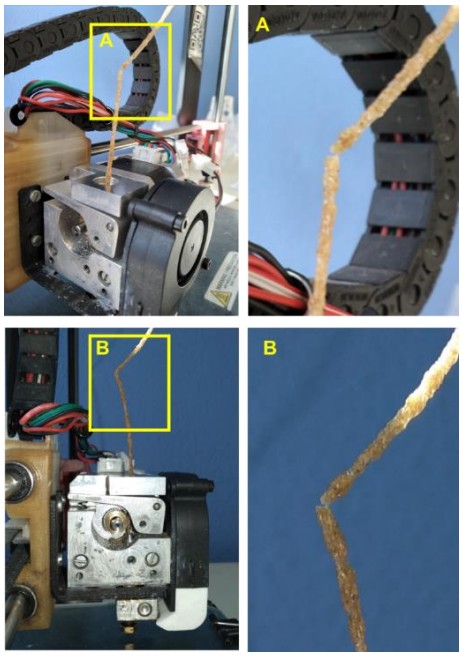

Figure 55- Filament with 10% RH content fracturing during 3D printing.

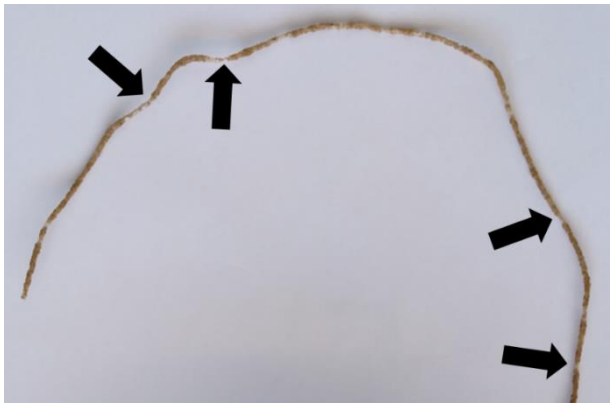

Figure 56- Filament with 15% RH content showing diameter thinning due to poor fiber distribution on the matrix.

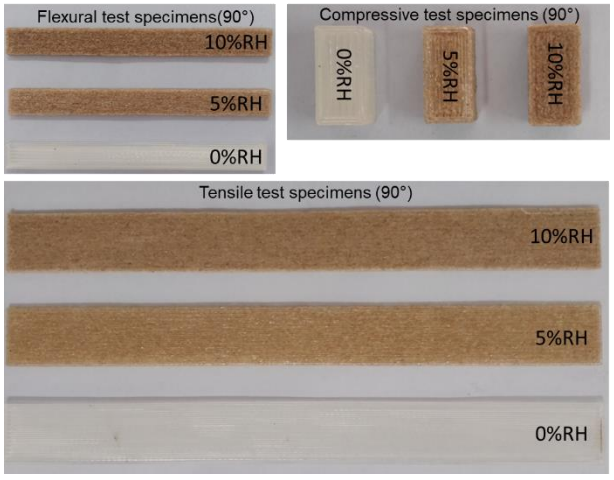

Figure 57- 90° direction printed specimens.

4.2. Densities and water absorption

4.2.1. Raw materials densities

The densities of whole RH and PLA 4043 pellets are given in Figure 58. The results showed that the density for whole RH is higher than the PLA 4043 pellets. The value determined for the PLA pellets is according to the density value provided by the technical datasheet of 4043D grade (≈1.24 g/cm³).

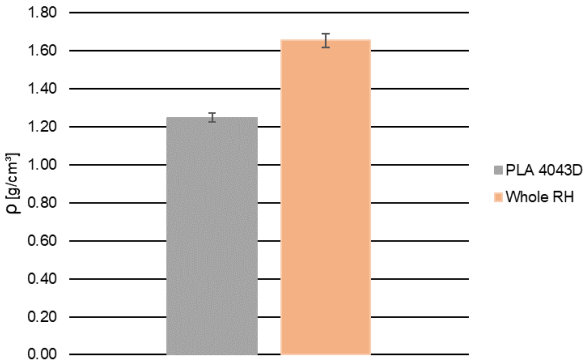

Figure 58- Raw materials densities [g/cm³].

4.2.2. Filaments and printed parts densities

Filaments (Figure 59) had revealed a decrease of density for fiber content above 5%. The density reduction was more accentuated for the filaments with 15% and 20% RH fiber content. When comparing the filaments with the printed samples, samples showed a significant density reduction for 5% and 10% RH content. Printed specimens had also shown an influence of printing direction on density reduction since the 5% RH-0° specimens demonstrated higher density values than the 5% RH-90° and 5% RH-45° samples. For neat PLA printed samples, density decrease was more visible in the 45° printing direction.

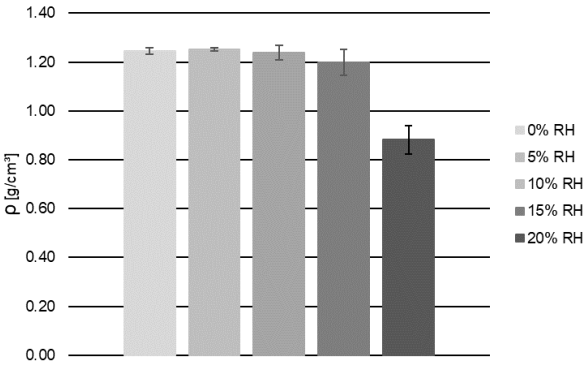

Figure 59- Filament densities [g/cm³].

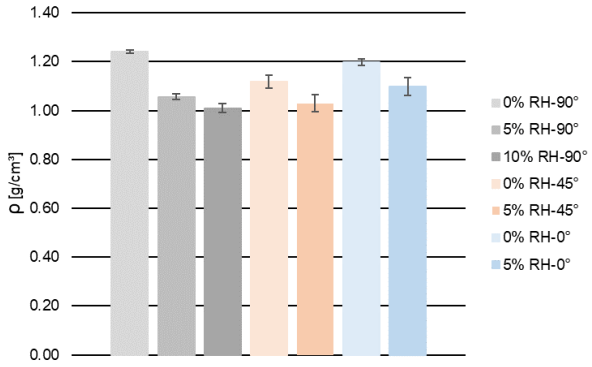

Figure 60- Densities [g/cm³] of printed specimens for compressive tests.

4.2.3. Water absorption

The samples revealed that water absorption (Figure 61) is more prevalent in the printed parts with RH content than those with only PLA. Moreover, 5% RH content printed parts had higher water absorption than the 10% RH ones.

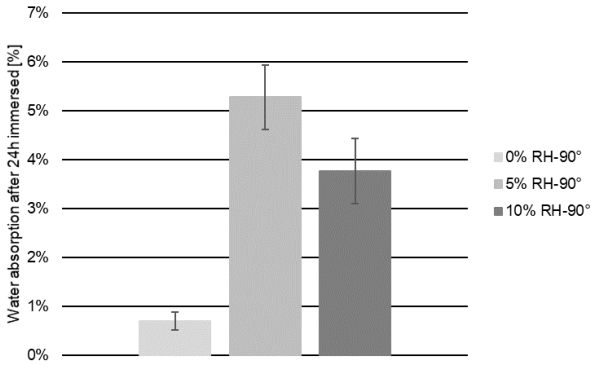

Figure 61- Water absorption [%].

4.3. Chemical analysis and thermal stability

4.3.1. FTIR analysis of untreated and treated RH fibers

Depicted in Figure 62 is the FTIR spectrum for treated and untreated RH. FTIR analysis shows several chemical changes induced by the alkali treatment. The primary changes were on the wavenumber ranges of OH, C-H, C-O and C=O bonds vibrations. The significant peaks labeled on the spectra of Figure 62 and their respective band assignment are detailed in Table 13. The results indicate a significant loss of transmittance in the peaks of alkali-treated husks located at 3334 cm^{-1}, 2920 cm^{-1}, 2850 cm^{-1} and 1310 cm^{-1}. These peaks correspond to the stretching frequencies of OH, C-H and C-O bonds. Peaks located at 1710 cm^{-1}, 1644 cm^{-1} and 1524 cm^{-1}, which are representative of C=O and C=C groups stretching, had an increase in transmittance. The elbow near the 1250 cm^{-1} frequency, coincident with C-O bond stretching,

disappeared after the alkali treatment. The spectrum of both samples showed evidence of the presence of moisture, revealed by the wide band at ca. 3334 cm^{-1}, at 1644 cm^{-1} and 650 cm^{-1}.

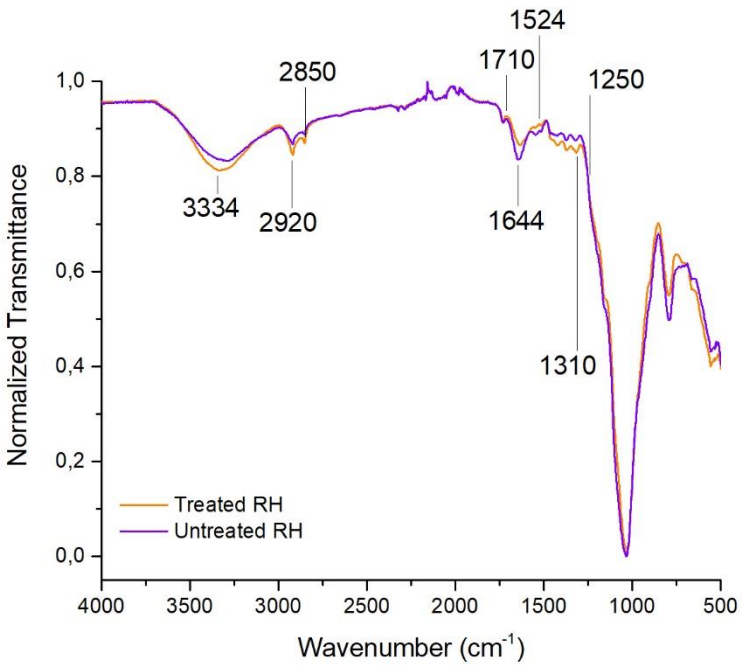

Figure 62- FTIR spectra of raw and alkali-treated fibers.

Table 13- RH (treated and untreated) FTIR band assignation.

Range [cm^{-1}]	Wavenumber [cm^{-1}] labeled on graph	Group
3550-3200	3334	OH stretching (strong)
3000-2840	2920	C-H stretching (medium)
3000-2840	2850	C-H stretching (medium)
1720-1706	1710	C=O stretching (medium)
1662-1626	1644	C=C stretching (medium)
1560-1510	1524	C=O stretching (medium)
1310-1250	1310	C-O stretching (medium)
1310-1250	1250	C-O stretching (medium)

4.3.2. Thermal stability of filaments and RH fibers

TGA (Figure 63) shows 4 relevant intervals where different stages of thermal degradation occur for the filaments and alkali-treated RH. The interval until 100°C shows a more accentuated weight loss for the RH and between 180°C and 250°C, the RH also has another weight loss stage. Between 250°C and 400°C, RH, neat PLA and composite filaments have their highest thermal degradation rate and it is visible at the DTG graph (Figure 64) that maximum peaks for all tested materials are located in this interval. Although neat PLA filaments had the highest temperature for the thermal degradation, showing a peak in the DTG graph between 350°C and 400°C, the

composites were revealed to have a higher residual weight above the 400°C than neat PLA, which might be due to the presence of char residues from the RH particles. The DTG shows a low peak for the RH and it is also noticeable in the TGA that RH had ≈40% more residual weight above the 400°C when compared with the filaments. These results reveal the presence of RH within the PLA matrix for the composites. And also, the presence of moisture (weight loss below 100°C) corroborates the FTIR results

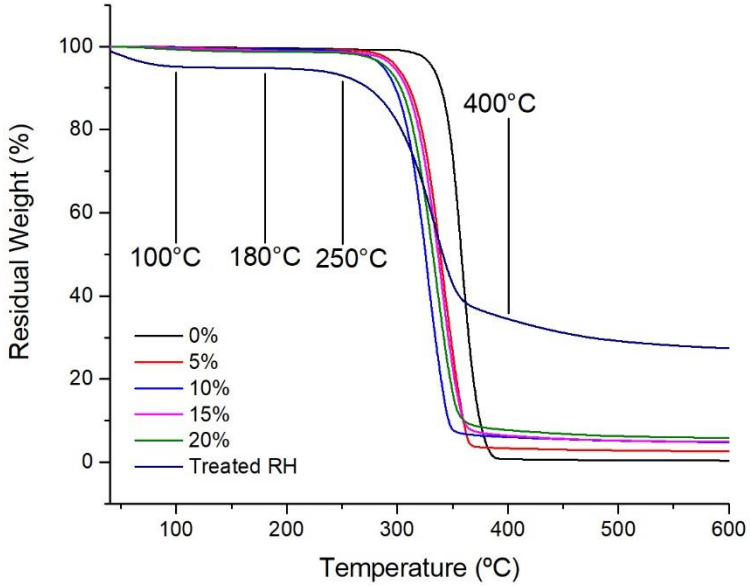

Figure 63- Filaments and treated RH TGA thermogram.

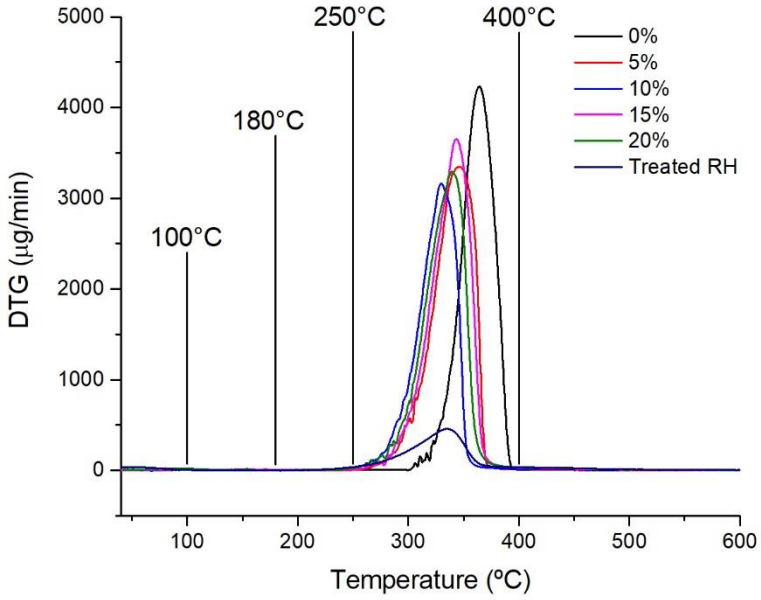

Figure 64- Filaments and treated RH DTG thermogram.

4.4. Mechanical properties of printed specimens

4.4.1. Tensile tests

All tensile tests (Table 14) revealed that adding RH fibers to PLA negatively affected the tensile strength in all printed directions. However, 5% RH-90° had similar ultimate tensile strength as 0% RH-45° printed specimens. Furthermore, 5% RH-90° specimens showed a higher young modulus and yield strength than the 0% RH-45° ones. In the 45° printing direction, 10% RH-45° specimens had better mechanical properties than the 5% RH-45° specimens. Independently of the type of filament used, 90° printing direction had superior mechanical performance and the 0° direction has the worst.

Table 14- Tensile tests results.

ISO 527-4 Type 2	UTS [MPa]		Yield Stress [MPa]		Elongation at break [%]		E [GPa]	
Sample	Mean	SD	Mean	SD	Mean	SD	Mean	SD
0% RH-90°	57.44	±1.66	46.59	±1.67	4.91	±2.37	3.33	±0.06
5% RH-90°	37.08	±1.53	32.82	±1.48	2.45	±0.11	2.60	±0.07
10% RH-90°	30.81	±2.94	25.50	±3.82	2.56	±0.18	2.54	±0.12
0% RH-45°	37.07	±5.41	31.74	±3.90	2.07	±0.28	2.69	±0.19
5% RH-45°	24.09	±2.26	22.53	±4.25	2.24	±0.30	1.86	±0.14
10% RH-45°	29.71	±2.05	25.11	±1.68	1.87	±0.11	2.60	±0.13
0% RH-0°	26.24	±12.99	25.53	±11.75	1.08	±0.46	2.81	±0.30
5% RH-0°	13.27	±4.68	13.19	±4.64	0.93	±0.09	1.77	±0.49

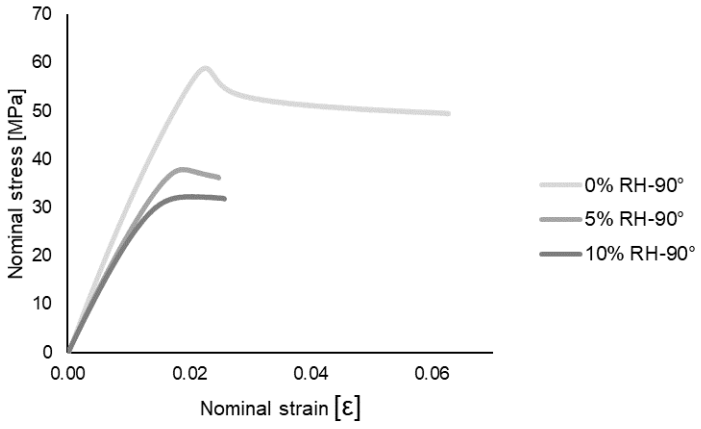

Figure 65- Typical tensile stress-strain curves for specimens with 90° printing direction.

Depicted in Figure 65 are the typical stress-strain curves of the 90° direction printed samples. It was observed that the neat PLA shows a higher mechanical performance than the composite specimens. Neat PLA also has a larger elongation to fracture, preceded by a plastic region. The

plastic region for the composites is almost inexistent. The composite blends revealed that fibers added brittleness to neat PLA. Figure 66 shows samples of fractured 90° printed specimens and there are no noticeable changes in the shape of tested specimens at a macroscale. However, SEM images of fractured surfaces (Figure 71) show different textures between blends. 0% RH-90° specimen has visible air gaps between layers with no detectable porosities at the scale of the images (Figure 71b). Composite specimens reveal an increased porosity along with the increment of fiber content (Figure 71c and Figure 71e) and uneven air gaps between layers for both blends. The PLA matrix still has a brittle fracture texture and random fractured RH fibers are detectable on the fractured surface of 5% RH-90° and 10% RH-90° specimens (Figure 71d and Figure 71f). Furthermore, RH fibers show reasonably good adhesion to the matrix.

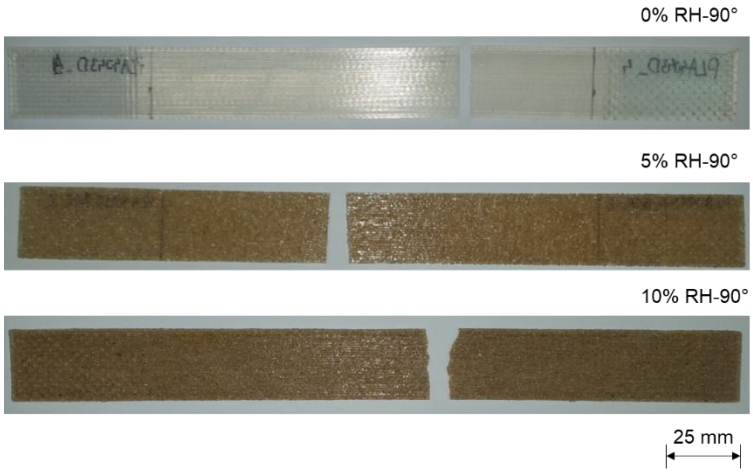

Figure 66- Tensile test fractured specimens printed at 90°.

The typical stress-strain curves for the 45° printed specimens are given in Figure 67. Neat PLA shows a slightly higher strain to fracture and all blends had a nonexistent plastic region with a breaking point at low strains. In terms of shape, tested samples (Figure 68) show no visible changes. 0% RH-45° under-extrusion (Figure 72b) and uneven air gaps with a nonuniform diameter of rasters. Composite specimens show more variation in raster diameter than neat PLA and it is visible in Figure 72d and Figure 72f that RH fibers do not have a specific orientation within the matrix. Figure 72e shows increased porosity for the 10% RH-45°.

The 0° specimens typical stress-strain curves (Figure 69) show totally brittle behavior for all tested samples, characterized by fracture at low strains without showing plastic region. The 0% RH-0° had a slightly higher strain to fracture than the 5% RH-90° composite material. Fractured samples (Figure 70) show no visible changes in the specimen shape after testing. The 0° specimens fracture surface SEM images (Figure 73) show that the rasters had poor adhesion between themselves, which is verified for 0% RH-0° and 5% RH-0° specimens. The small surfaces with adhesion reveal brittle fracture texture. In addition, the 5% RH-0° sample shows porosities (Figure 73d) and randomly distributed fibers (Figure 73c).

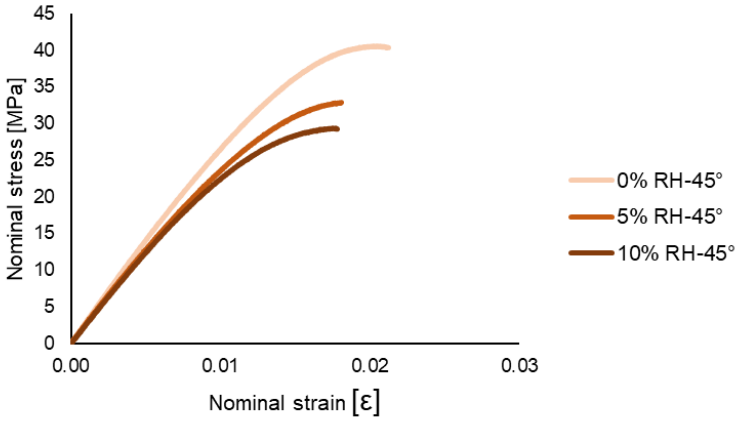

Figure 67- Typical tensile stress-strain curves for specimens with 45° printing direction.

Figure 68- Tensile test fractured specimens printed at 45°.

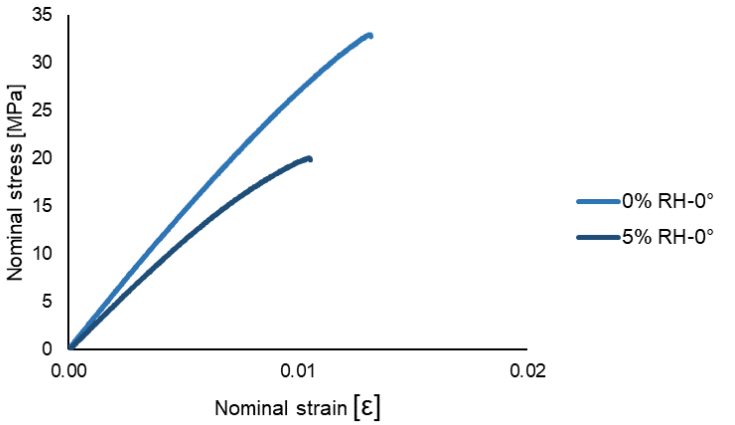

Figure 69- Typical tensile stress-strain curves for specimens with 0° printing direction.

Figure 70- Tensile test fractured specimens printed at 0°.

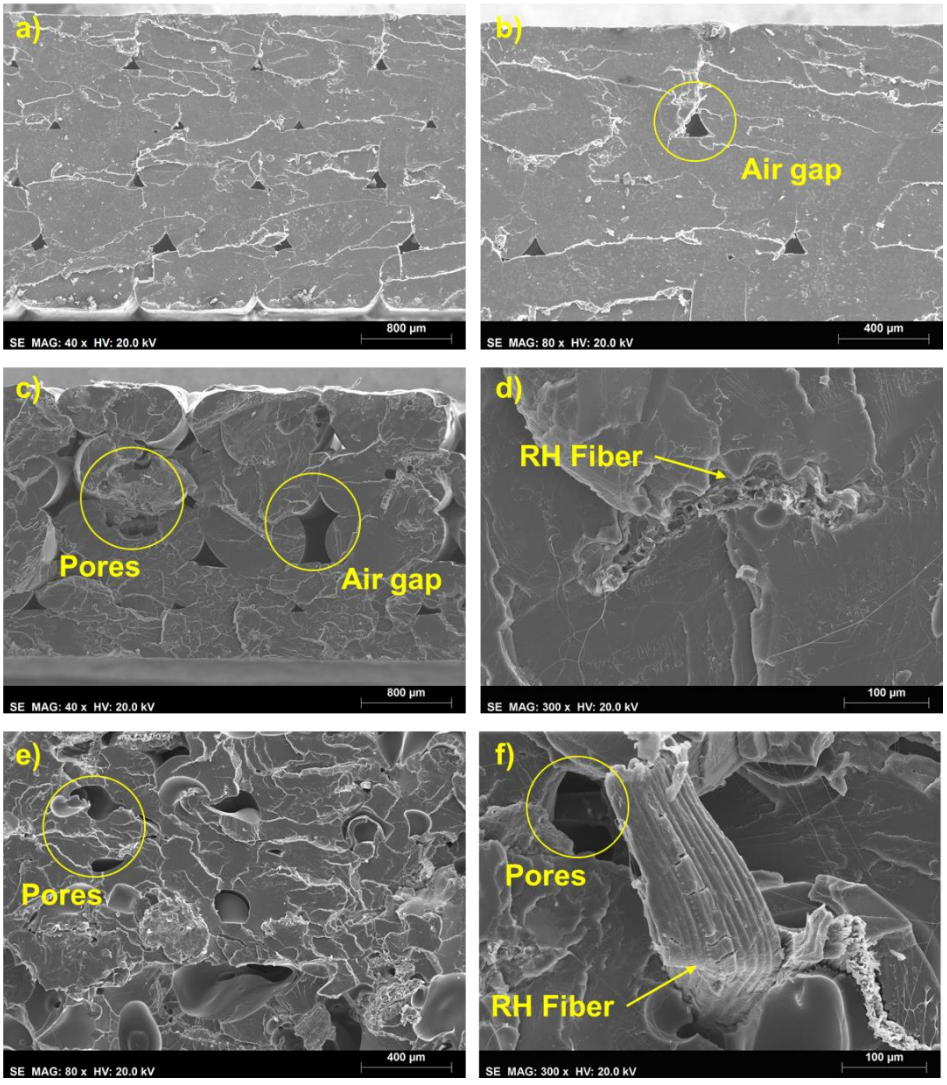

Figure 71- Tensile tested fracture surfaces SEM images of: a) 0% RH-90°.; b) Detail from 0% RH-90°.; c) 5% RH-90°.; d) Detail from 5% RH-90°.; e) 10% RH-90°.; f) Detail from 10% RH-90°.

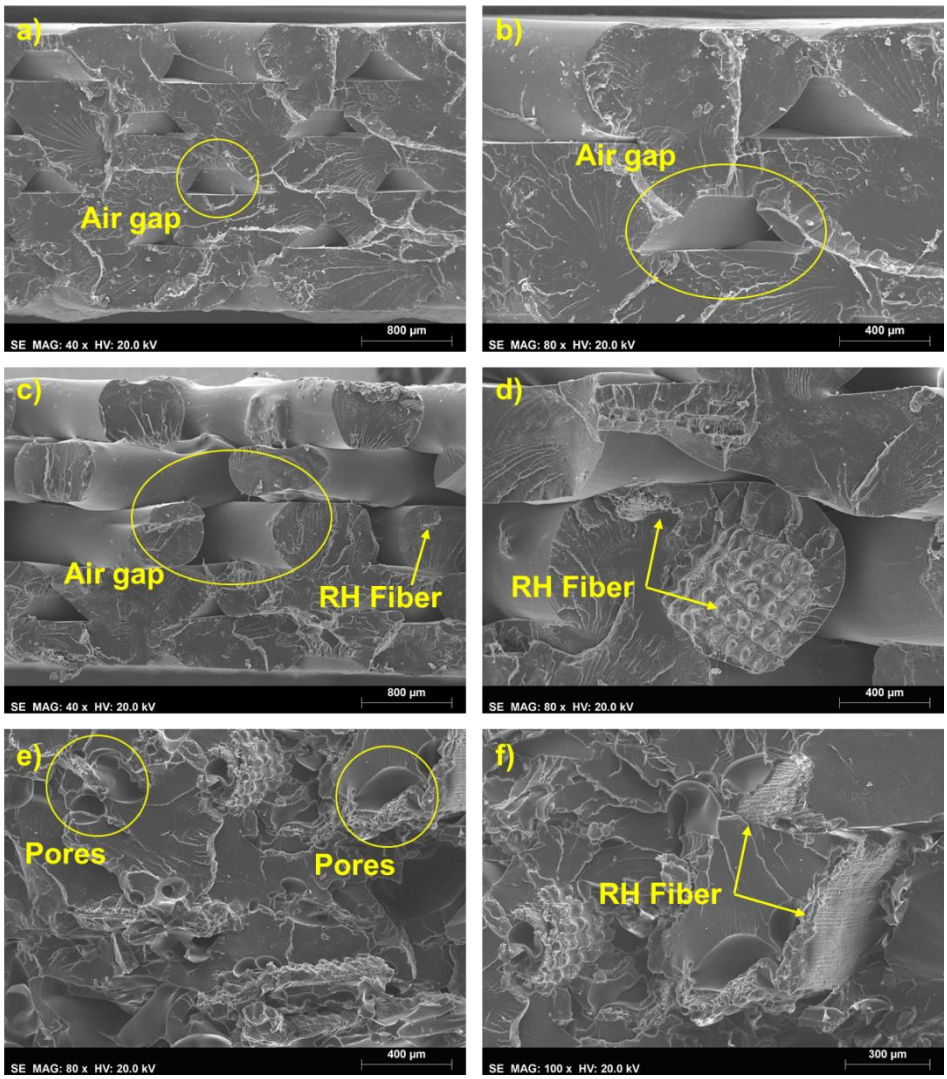

Figure 72- Tensile tested fracture surfaces SEM images of: a) 0% RH-45°.; b) Detail from 0% RH-45°.; c) 5% RH-45°.; d) Detail from 5% RH-45°.; e) 10% RH-45°.; f) Detail from 10% RH-45°.

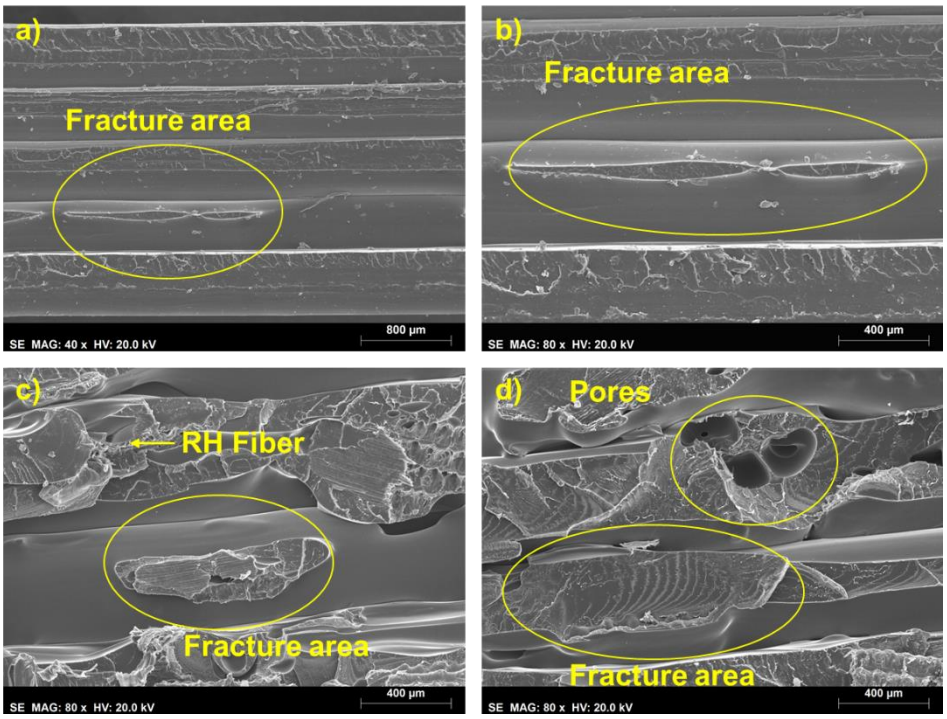

Figure 73- Tensile tested fracture surfaces SEM images of: a) 0% RH-0°.; b) Detail from 0% RH-0°.; c) 5% RH-0°.; d) Detail from 5% RH-0°.

4.4.2. Compressive tests

Results from the mechanical behavior of printed parts under compressive forces are depicted in Table 15. Specimens printed in a 90° direction had the highest compressive strength. The neat PLA had the highest yield stress and young modulus values. The 90° tested samples also show that adding fibers to filaments does not improve the compressive strength. The compressive strength is affected by the fiber content in all printing directions tested. Specimens with a 45° printing direction had the lower compressive strength values (0% RH-45°, 5% RH-45°).

Table 15- Compressive tests results.

ASTM D695	Yield Stress [MPa]		E [GPa]	
Sample	Mean	SD	Mean	SD
0% RH-90°	83.98	±2.33	2.69	±0.06
5% RH-90°	52.39	±4.24	1.54	±0.27
10% RH-90°	44.01	±2.84	1.34	±0.06
0% RH-45°	45.11	±2.47	1.80	±0.12
5% RH-45°	20.81	±2.40	1.02	±0.15
0% RH-0°	69.41	±4.00	2.35	±0.14
5% RH-0°	47.17	±9.61	1.53	±0.30

Regarding to 90° printed specimens, typical stress-strain curves (Figure 74) it was found three distinct behaviors. The 0% RH-90° had failure by shear stress showing sliding planes at 45°

(Figure 75). The 5% RH-90° specimens (Figure 75) had failure by instability between layers and showed poor adhesion between layers. The 10% RH-90° specimens (Figure 75) had plastic deformation after yielding without structural failure.

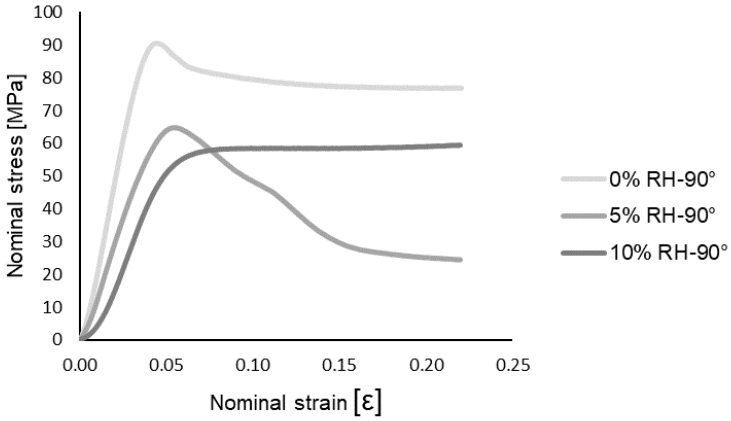

Figure 74- Typical compressive stress-strain curves for specimens with 90° printing direction.

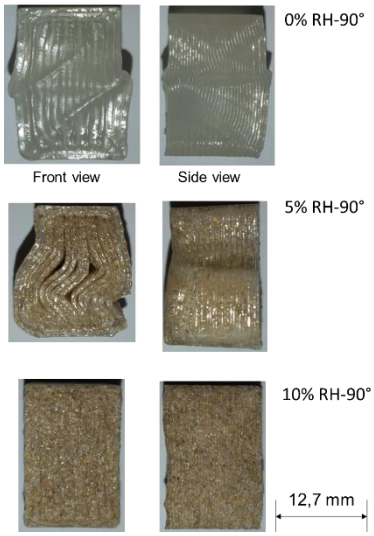

Figure 75- Compressed specimens printed at 90°.

0% RH-45° and 5% RH-45° deformed specimens (Figure 77) and their respective typical stress-strain curves (Figure 76) show a conventional behavior for this type of materials where the increase of nominal stress after yield is justified by the increase of the cross-sectional area under compression.

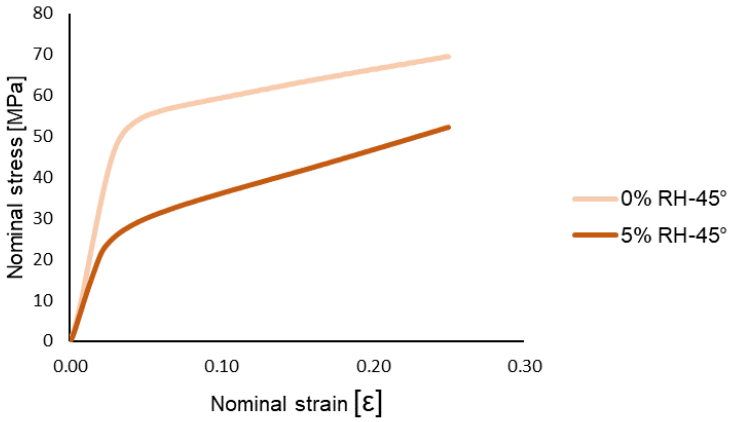

Figure 76- Typical compressive stress-strain curves for specimens with 45° printing direction.

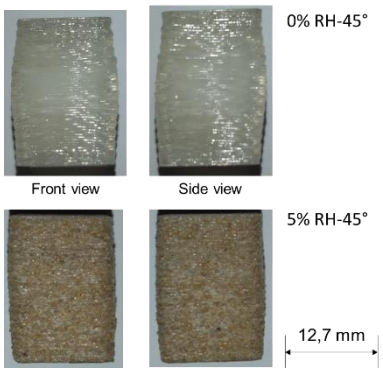

Figure 77- Compressed specimens printed at 45°.

Typical stress-strain curves of 0% RH-0° and 5% RH-0° specimens (Figure 78) show two distinct behaviors. 0% RH-0° specimens (Figure 79) had a typical curve showing plastic deformation. However, the 5% RH-0° specimens (Figure 79) showed a loss of strength in the plastic domain due to the layer structure failure (Figure 78).

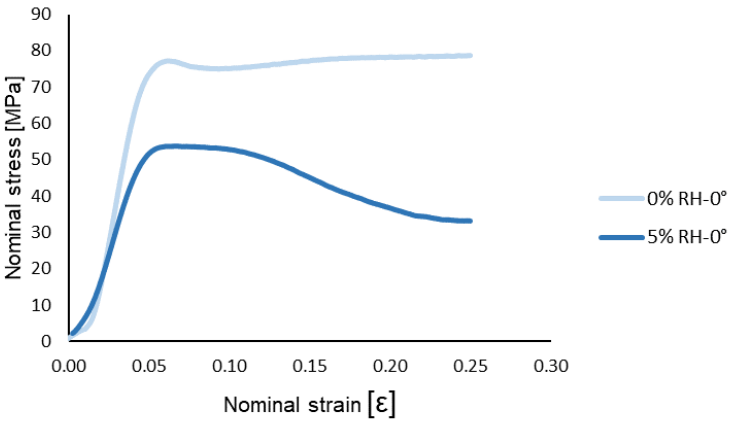

Figure 78- Typical compressive stress-strain curves for specimens with 0° printing direction.

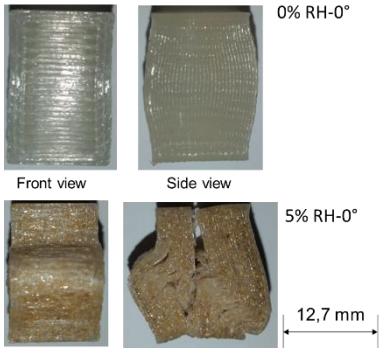

Figure 79- Compressed specimens printed at 0°.

4.4.3. Flexural tests

The flexural test results for the 90° printed specimens are depicted in Table 16. are the flexural test results for the 90° printed specimens. The results revealed that the flexural strength of printed parts is not improved by the presence of RH. The 5% RH-90° and 10% RH-90° had almost the same maximum flexural strength, but the flexural modulus for the 10% RH-90° was higher than the 5% RH-90°.

Table 16- Flexural tests results.

ASTM D790	Maximum Flexural Stress [MPa]		Flexural Modulus [MPa]	
Sample	Mean	SD	Mean	SD
0% RH-90°	109.05	±3.93	3590.14	±164.90
5% RH-90°	70.43	±0.84	2386.94	±82.99
10% RH-90°	69.28	±4.74	2754.70	±216.65

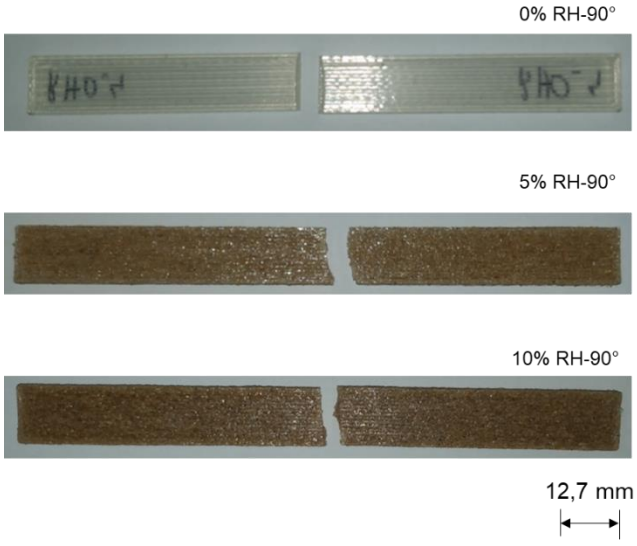

Figure 80- Flexural test fractured specimens printed at 90°.

SEM image of Figure 81a shows the distinct texture of a fracture by a flexural load in a 0% RH-90° specimen. Above the neutral plane, the texture is from the compressed side and below from the tensile side. Figure 81a and Figure 81b show intermeshed airgaps between layers for the 0% RH-90° sample. Textures from the 5% RH-90° (Figure 80c; Figure 80d) and 10% RH-90° (Figure 80e; Figure 80f) fracture surfaces show poor layer adhesion, under extrusion and severe porosities, along with uneven fiber distribution on the matrix.

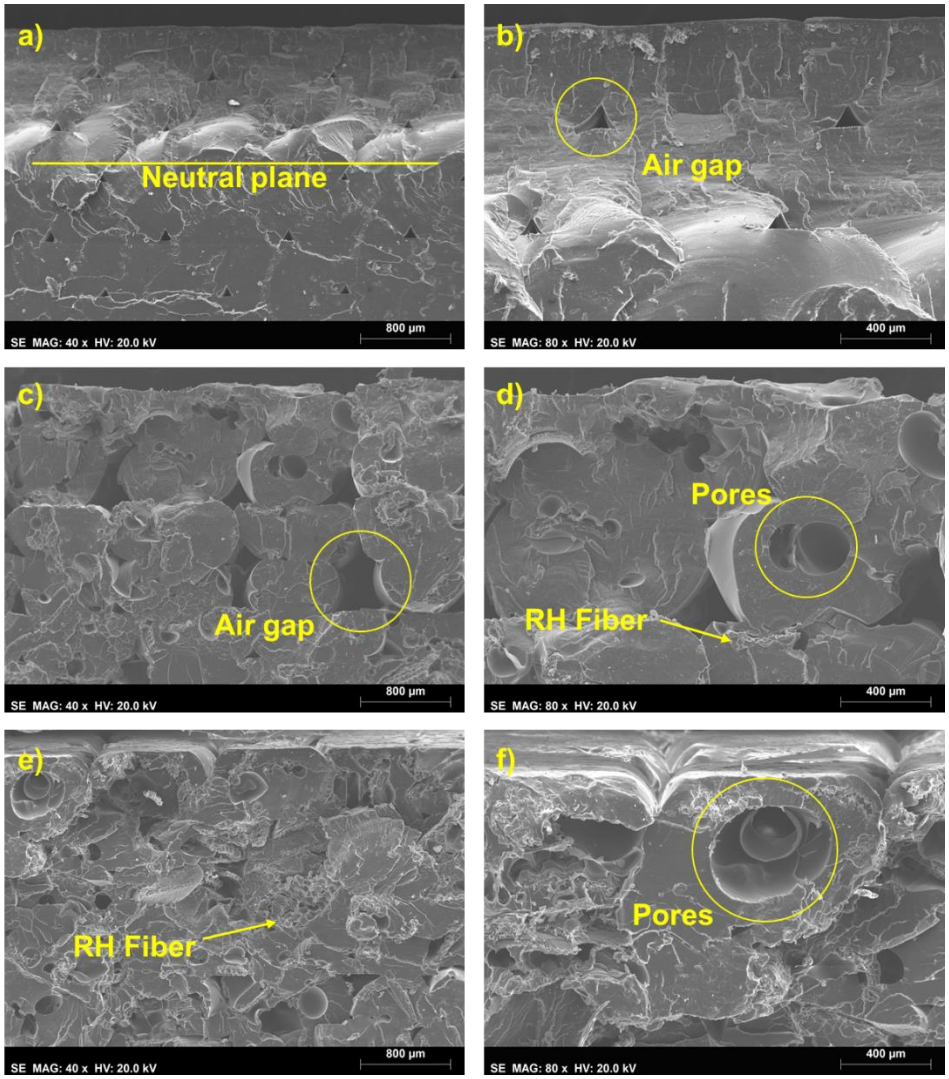

Figure 81- Flexural tested fracture surfaces SEM images of: a) 0% RH-90°.; b) Detail from 0% RH-90°.; c) 5% RH-90°.; d) Detail from 5% RH-90°.; e) 10% RH-90°.; f) Detail from 10% RH-90°.

Chapter 5
Discussion

This chapter contains the interpretation and discussion of the results obtained in the previous chapter. The effects of alkali treatment on fibers and the printability of the produced filaments are analyzed. Densities and water absorption of printed specimens are discussed. The mechanical behavior of the printed parts under tensile, compressive and bending loads, are also analyzed.

5.1. Introduction

The ever-growing environmental issues due to petroleum-based polymeric materials have increased the demand for more sustainable resources, eco-friendly materials and recyclable products. Thus, the objective of this work was to develop and characterize rice husk filled PLA composites obtained by fuse deposition modeling (FDM). For that, rice husk fibers were prepared, sieved, alkali-treated, dried and blended with PLA to extrude AM filaments with 0%, 5%, 10%, 15% and 20% wt.% in fiber. In addition, 3D printed specimens were produced and characterized.

5.2. Fibers and alkali treatment

Changes in the size, shape and surface of fibers were obtained in this work due to mechanical grinding. As shown in the SEM images of Figure 52a and Figure 52d, prepared and unprepared RH has a wide range of shapes and sizes and the thickness remained almost unchanged. Identical results were discussed in the work of E. Csiszár *et al.* [37]. Their research reported that mechanical grinding changed the external form of cotton fibers and lateral fiber dimensions, but the thickness remained unchanged. Furthermore, grinding RH fibers increased fiber size variation, as reported in the work of Y. Huang *et al.*[38]. The mechanical grinding effects in RH external surfaces are visible, especially in the SEM image of Figure 52b, where delamination is detectable in fiber surfaces due to the grinding procedure. This delamination is in a certain way desirable since that the outside surface of fibers exposed to chemical treatment will be increased. Nevertheless, the variation of surface amounts between fibers exposed to chemical treatment will induce variations in the chemical structure of treated fibers, increasing the heterogeneity in behavior of the fibers when blended with the polymeric matrix. The effect of grinding on chemical treatment was reported by M. Benítez-Guerrero *et al.* [36], where chemical modifications were attributed to the exposure of intracellular elements and variable proportions of crystalline cellulose and amorphous components.

Modifications of the RH chemical structure were found to occur with the alkali treatment. Comparing the FTIR spectra of raw and alkali-treated RH (Figure 62), there are transmittance value changes in peaks that were reported by several authors as indicators of relevant chemical modifications in lignocellulosic fibers. These peaks (Table 13) are on the vibrational frequency ranges of OH, C-H, C=O and C=C groups, which are associated with cellulose, hemicellulose and lignin components, as well as water absorption [36],[41],[42],[43],[47]. The broad peak found at ≈3334 cm^{-1} is related to OH bond stretching, attributed to hydroxyl groups of cellulose and eventually some moisture present in the material [42],[84],[91],[92]. A reduction in transmittance on the OH bonding range in alkali-treated RH may indicate an increase in cellulose fraction after treatment. The peaks located at ≈2920 cm^{-1} and ≈2850 cm^{-1} are in the range of C-H bond stretching, characteristic of cellulose and hemicellulose [42],[91]. The transmittance value decreasing on these peaks (≈2920 cm^{-1} and ≈2850 cm^{-1}) may express the cellulose content increase in treated fibers. Hemicellulose fraction increasing linked to peaks on the ≈2920 cm^{-1}

and ≈2850 cm^{-1} wavenumbers are unlikely in this analysis. Moreover, several authors referred that peaks on the C-O and C=O stretching wavenumbers are related to hemicellulose [47][84]. These peaks are identifiable in the spectra of Figure 62, where a peak at ≈1710 cm^{-1} (C=O stretching) and a shoulder at ≈1250 cm^{-1} (C-O stretching) reveal a transmittance increase. Thus, the hemicellulose fraction may have decreased due to alkali treatment. Regarding lignin fraction, an evidence for its reduction was found after the treatment, due to a decrease in intensity observed for the peak at ca. 1524 cm-1, attributed by M. Sanjay *et al.* [11] to the presence of aromatic rings in lignin structure. Lignin content reduction can be complemented by the observations of Oh *et al.* [41] and T. Tran *et al.* [41], where the shifting of the broad peak located at ≈3334 cm^{-1} towards a higher wavenumber was attributed to lignin fraction variations. Water absorption may have decreased in treated fibers, indicated by the decrease in intensity of the peak located at ≈1644 cm^{-1} [36],[41],[43]. M. Kathirselvam *et al.* [42] and A.N. Balaji *et al.* [92] had done a correlation with hemicellulose in the band at ≈1637 cm^{-1} and 1663 cm^{-1}, where the dissolution of hemicellulose can be masked by the assumption of water absorption decrease. Nonetheless, the TGA (Figure 63) curve for the treated RH reveals a loss in weight of ≈2% in the temperature interval between 40°C and 100°C, coincident with moisture evaporation.

There is strong evidence that alkali treatment was effective in this work since FTIR analysis suggests that the fraction in cellulose increased and some hemicellulose and lignin were dissolved by the NaOH. Affinity with water absorption may have decreased as a result of alkali treatment.

5.3. Effect of fibers in filament printability

Filaments with 0%, 5% and 10% in RH content were printable. However, the 10% RH content filament had provoked constant nozzle cloggings and showed a tendency to fracture while subject to the feeding process of the extruder. The filaments of 15% and 20% in RH content showed no feasibility for 3D printing. Effects of fiber content on 3D printing were evident and related to the heterogeneity of the filaments and the poor distribution of fibers on the matrix. The increment of fiber content increased the filament diameter variation and roundness, as shown in Figure 54. X. Xiao et al. [62] also identified inconsistencies in filament diameter and roundness as a potential cause of nozzle clogging. The same observation was done by M. Kariz *et al.* [20]. In their work with wood particles and PLA, nozzle cloggings were attributed to filament diameter variations and blends with higher content of wood particles. Since the printable filament blends used here had their density values (Figure 59) almost unaffected by the fiber content, there is no significant correlation between filament densities and nozzle clogging. The same results on filament densities were obtained by M. Kariz *et al.* [20], where densities of wood/PLA filaments remained with low variation for fiber contents of 0%, 10% and 20%. RH filaments had their densities more affected only for fiber contents of 15 and 20%. Considering that those were the unprintable filaments, density values can be correlated with the lack of stiffness obtained in these filaments and further unstable behavior for a proper feeding process of the extruder. In SEM images of

Figure 54, it is visible that filaments with 15% and 20% fiber content have fiber agglomeration. Thus, clusters of fibers within the matrix may have voids inside, which can cause density decrease and lack of stiffness. Clusters are also visible in Figure 53b, especially in the 15% and 20% RH content filaments and analyzing the 15% RH filament section of Figure 56, it can be detected that the unprintable blends are categorized by fiber agglomeration sections folowed by an extruded thin section of matrix material. This is a extrusion issue caused by the variable throughput rate of filament, due to the large size of fiber particles that induce high variations in viscosity of the composite inside the extruder.

The thermal stability of neat PLA was affected by the fiber content. Analyzing the DTG peaks (Figure 64), 0% RH filament had a maximum mass loss rate at ≈363°C, followed by the 5% RH (≈346°C), 15% RH (≈343°C), 20% RH (≈340°C)

and 10% RH (≈330°C). The 10 % RH showed a higher mass-loss rate than the 15% RH and 20% RH, which is probably related to the poor fiber distribution within the matrix. The percentage of the residual weight along temperature increase (FTIR thermogram from Figure 63) was higher for the 0% RH until ≈375°C and at higher temperatures, the composite filaments had maintained a higher residual weight. This fact was observed and reported by M. Kathirselvam *et al.* [42]. The higher residual weight of composite materials was attributed to waxes and some lignin portions in the fibers, which have a final thermal degradation stage between 280°C-500°C [42]. For the composite filaments, the primary weight loss started at ≈250°C and for the neat PLA filament at ≈290°C. Comparing these temperatures with the treated RH thermal degradation profile, where a weight-loss stage was verified between 180°C and 250°C (hemicelluloses decomposition [33]), there is evidence that fibers were more thermally stable within the PLA matrix. Regarding the chemical bonding between treated RH and PLA, T. Tran *et al.* [41] reported that a good chemical bonding between RH and the PLA matrix affects the thermal degradation temperature of the fibers. Moreover, in their study, the maximum mass loss rate (DTG) peak determined for alkali-treated RH was at 336°C, the same value obtained in this work.

The composite printable filaments (5% RH and 10% RH) and their primary weight-loss stage temperature (≈250°C) indicated that alkali-treated RH is suitable for use as a filler in polymeric matrices, at operating temperatures of less than 250°C, without significant thermal degradation. Considering that in this work, the nozzle temperature used was 220°C, filaments were processed at a safe temperature concerning the thermal degradation of fibers.

5.4. Properties of 3D printed parts

5.4.1. Densities and water absorption

Water absorption and densities of printed parts were negatively affected by adding RH fibers to PLA. Water absorption (Figure 61) was higher for the 5% RH than for the 10% RH samples,

which may relate to the uneven fiber distribution along the filament and thus, on the printed part. Furthermore, printing defects inside the part may have contributed to voids that were additional spaces for water. Thus, although results indicate that the composites had higher water absorption than neat PLA. The differences between water absorption on the 5% RH and 10% RH can be related to printing defects. Printing defects may also affect printed parts densities and that evidence was described in the work of M. Kariz *et al.* [20] on wood/PLA printed parts. In their work, variations in densities were associated with the fiber content present on 3D printed parts.

The densities of composite printed samples (Figure 60) revealed a significant decrease in comparison with the filaments (Figure 59). The 5% RH -90° and 10% RH-90° printed samples showed a density decrease of 15% and 19%, respectively. Since raw fibers have a higher density (≈ 1.6 g/cm³) than PLA (≈1.24 g/cm³), printing defects might be the primary cause of density decrease. The majority of printing defects were under extrusion and pores. The under extrusion issues are clearly visible in SEM images of Figure 71c and Figure 72c. Pores were detected on several composite samples (SEM images of Figure 72e and Figure 73d). The under extrusion in this type of material strongly relates to filament diameter variation, which is in agreement with observations done by M. Kariz *et al.* [20] and X. Xiao *et al.* [62]. In their research, inconsistent filament diameter is linked to unsteady extrusion and variable amounts of material extruded to the part layers.

The 0% RH-90° samples showed almost no density variation (-1%) compared with the filament, but the 0% RH-45° (density variation of -10%) had revealed that printing direction might also have a relation with density decrease. Concerning printing direction, 5% RH-45° (density variation of -18%) had the highest decrease in density within the 5% RH blend. Thus, 45° was the printing direction that most affected the densities of printed parts. The 45° printing direction affects the parts densities due to the nozzle path. In contrast to the 0° and 90° directions, in the 45° direction, the raster path does not cover the layer corners, creating additional voids between layers. Regarding printing defects, pores were another issue that affected printed parts densities. V. Balla *et al.* [8] correlated pores with the low density of composite (soybean hull/copolyester) parts. In their study, spherical and elliptical gas pores were identified on printed parts and the cause was pointed as being water vapor released from the fibers when printing at 220°C. Similar pores were detected in this work due to the used nozzle temperature (220°C). Those pore geometries can be seen in Figure 71f and Figure 72f, where it is visible that some pores are in the fiber/matrix interface area. Pores adjacent to the fibers are a clear indicator that fibers were the pores source. A. Célino *et al.* [93] reported that water could be trapped inside PF natural pores due to complex sorption mechanisms. In their study, capillarity is pointed to as one of the probable moisture absorption mechanisms of PF. In Figure 81f, it can be seen a pore with a dimension of ≈0.4mm, which is a considerable dimension. Thus, there is evidence that the filaments absorbed moisture during storage and that moisture was absorbed and trapped within fiber pores.

In summary, the detected main causes for density decrease on printed parts were defects caused by under extrusion and water vapor. Nevertheless, the printing direction of 45° should not

be discarded as a source of voids inside printed parts because the nozzle path does not cover the layer corners.

5.4.2. Mechanical properties

The mechanical strength of printed parts was affected by fiber content and printing direction. The printing direction was pointed by V. Mazzanti *et al.* [6] as a significant variable in the tensile strength of printed parts, where longitudinal printed specimens are significantly more resistant than specimens following other printing directions. That evidence is visible in this work. By analyzing the results of the tensile tests (Table 14), it is clear that better mechanical properties were obtained in the longitudinal (90°) printed parts. The tensile strength value obtained for the 0% RH-90° specimens (57 MPa) and Young modulus (3.33 GPa) was similar to the ones reported by several authors, even comparable with results obtained on hot-pressed samples. C. Tsou *et al.* [12] had in their research a tensile strength value of 50 MPa for hot-pressed samples using the Ingeo™ 4042D grade of PLA (Figure 15) blended with a filler compatibilizer. M. Kariz *et al.* [20] obtained a tensile strength of 55 MPa and a Young modulus of 3.27 GPa for printed parts with a very similar PLA grade (Ingeo™ 2003D (Figure 15)) to the one used in this work. Moreover, in their research, two commercial neat PLA filaments were also tested, achieving the same results for tensile strength (55 MPa). Thus, tensile tests show that the neat PLA filaments produced in this work printed parts with excellent tensile strength performance. Nevertheless and as aforementioned, the printing directions of 0° and 45° had a negative effect on the tensile and compressive strength of neat PLA printed parts. Under tensile loads, the tensile strength of 0% RH-45° decreased 35% and the 0% RH-0° decreased 54%, which indicates that transversal printing direction (0°) was the worst in terms of tensile strength. The reason for this decrease was the printing direction and printing defects such as poor adhesion between rasters (Figure 73a) for the 0% RH-0° and poor layer adhesion for the 0% RH-45° (Figure 72b). Both of the issues seem to have a relation with under extrusion. For compressive strength, the yield stress for the 0% RH-90° was 84 MPa, folowed by the 0% RH-0° (69 MPa) and 0% RH-45° (45 MPa). For compressive loads the vertically printed specimens with a direction of 45° had the lower strength. One of the reasons might be related to the nozzle path and the additional voids created, specially on the corners of the layers.

The composite samples had a decrease of tensile strength of 35% for the 5% RH-90° and 46 % for the 10 % RH-90°. This decrease is related to the under extrusion due to high filament diameter variations. Moreover, a high amount of pores also contributed to the mechanical strength decrease. The under extrusion is visible on SEM images of Figure 71c and Figure 72c. Large size pores are visible in SEM images of Figure 71f and Figure 81d. These irregularities on printed parts resulting from adding PF fibers to PLA were also pointed out by M. Kariz et al. [20]. The printing direction effect on composite tensile specimens was the same as for the neat PLA. The 5% RH-0° has the wort results within the %5 RH blend and the 10% RH-45° has the lowest

strength within the 10% RH blend. Nevertheless, the 10% RH blend had no 0° printed direction test specimens.

In terms of Young modulus and elongation at break, adding fibers decreased the elasticity modulus and added brittleness to the parts. The 5% RH-90° and 10% RH-90° had a decrease in the elasticity modulus of 22% and 24%, respectively. The elongation at break showed clear negative effects of fibers, where the 5% RH-90° and 10% RH-90° had a decrease of 50% and 48%, respectively. The brittleness added due to fiber content was also reported by X. Xiao *et al.* [62]. Their research concluded that increased porosity due to fiber content adds overall embrittlement of the printed parts.

The results were also clearly conclusive for the compressive tests, with the printing direction and fiber content affecting the yield stress and compressive modulus. The worse results were obtained for the vertically 45° printed specimens. Nevertheless, in the compressive tests, different failure mechanisms were obtained as a function of printing direction. The 90° printed samples had a failure behavior in agreement with V. Mazzanti et al. [6], where buckling of layers is the primary mechanism of part failure. Other directions had typical behaviors under compression for this type of material.

Flexural tests showed no enhancement of mechanical properties on bending by adding fibers. The high number of pores and under extrusion issues on the composite samples visible in Figure 81 were the primary causes of mechanical strength decrease under bending of composite parts.

In general, the tensile, compressive and bending strength of composite printed parts were affected by the same issues, namely:

- Variable amounts of deposited material (under extrusion) on the layers due to filament diameter variations;
- Pores caused by the fiber moisture content;
- Printing direction.

Chapter 6
Conclusions and future work

This chapter contains the conclusions to the results obtained after this research. Few considerations for future work are also addressed.

6.1. Conclusions

The objective of this work was to develop and characterize NFFP filaments made of RH fibers and PLA for use in AM. Filaments with 5%, 10%, 15% and 20% in RH fiber content and a control filament of neat PLA were extruded. Printability tests were done and the printable filaments were used to produce samples to study the obtained material behavior under tensile, compressive and bending tests. In addition, the thermal behavior of filaments and the chemical effects of alkali treatment on the fibers were also studied. Densities for filaments, fibers and printed parts were determined. The water absorption of printed parts was also analyzed.

After the study, the primary conclusions on the processes and materials were:

- Alkali treatment changed the chemical structure of RH fibers. FTIR analysis had shown that hemicellulose and lignin content of fibers may have decreased, which is in agreement with desirable results;
- The filament extrusion process had the fiber size, moisture content of raw materials, process temperatures and screw rotation speed as critical variables. The extruded filaments densities showed that the density was not significantly affected by the fiber content;
- Significant issues on printability were observed due to high variations of filament diameter as a result of fiber size and poor distribution of the fibers within the matrix;
- Nozzle cloggings, filament brittleness and the unprintability of the 15% RH and 20% RH blends are due to the fiber agglomeration and their poor distribution within the matrix;
- The quality of printed parts in terms of mechanical strength and densities were severely affected by the filament diameter variation, which caused under extrusion defects;
- The fiber content of 10% was the fiber limit for a printable filament considering the fiber size used. Despite being printable, the 10% RH filament caused severe nozzle cloggings;
- Filaments of 5% RH content, although containing some diameter variations and poor fiber distribution, were revealed to have reasonably good printability, showing no nozzle cloggings or fractures during the 3D printing process;
- Neat PLA filaments indicated that it is possible to produce reasonably good quality filaments using a desktop extruder.

Although the challenges and issues described above, RH fibers can be used as a filler in biopolymers such as PLA.

6.2. Considerations for future work

After the experience acquired in this work, several improvements can be pointed to achieve better results on the filaments, increase the allowable fiber content and reduce the printed parts defects. The suggestions are the following ones:

- Reduce the fiber dimensions to at least 0.1mm, for instance, using a mill operated with liquid N_2, allowing the use of a smaller diameter nozzle;
- Analyze the effectiveness of alkali treatment on the mechanical properties of the printed parts by producing a control filament with fibers without treatment;
- Apply a 2 stage procedure to produce filaments: use a twin roll mill to promote a good dispersive mixing, then pelletize and use a single-screw extruder to obtain the filaments;
- Alternatively, a twin-screw extruder in counter-rotating mode could be used to obtain a good dispersive and distributive mixing in the filaments.

References

[1] V. K. Balla, K. H. Kate, J. Satyavolu, P. Singh, and J. G. D. Tadimeti, “Additive manufacturing of natural fiber reinforced polymer composites: Processing and prospects,” *Compos. Part B Eng.*, vol. 174, no. March, p. 106956, 2019, doi: 10.1016/j.compositesb.2019.106956.

[2] A. Gholampour and T. Ozbakkaloglu, *A review of natural fiber composites: properties, modification and processing techniques, characterization, applications*, vol. 55, no. 3. Springer US, 2020.

[3] R. Siakeng, M. Jawaid, H. Ariffin, S. M. Sapuan, M. Asim, and N. Saba, “Natural fiber reinforced polylactic acid composites: A review,” *Polym. Compos.*, vol. 40, no. 2, pp. 446–463, Feb. 2019, doi: 10.1002/pc.24747.

[4] N. Karthi, K. Kumaresan, S. Sathish, S. Gokulkumar, L. Prabhu, and N. Vigneshkumar, “An overview: Natural fiber reinforced hybrid composites, chemical treatments and application areas,” *Mater. Today Proc.*, vol. 27, pp. 2828–2834, 2019, doi: 10.1016/j.matpr.2020.01.011.

[5] B. Panda, M. J. Tan, I. Gibson, and C. K. Chua, “The disruptive evolution of 3D printing,” *Proc. Int. Conf. Prog. Addit. Manuf.*, vol. Part F1290, pp. 152–157, 2016.

[6] V. Mazzanti, L. Malagutti, and F. Mollica, “FDM 3D printing of polymers containing natural fillers: A review of their mechanical properties,” *Polymers (Basel).*, vol. 11, no. 7, pp. 1–22, Jun. 2019, doi: 10.3390/polym11071094.

[7] L. Liu, M. Lin, Z. Xu, and M. Lin, “Polylactic acid-based wood-plastic 3D printing composite and its properties,” *BioResources*, vol. 14, no. 4, pp. 8484–8498, 2019, doi: 10.15376/biores.14.4.8484-8498.

[8] V. K. Balla, J. G. D. Tadimeti, K. H. Kate, and J. Satyavolu, “3D printing of modified soybean hull fiber/polymer composites,” *Mater. Chem. Phys.*, vol. 254, no. March, p. 123452, 2020, doi: 10.1016/j.matchemphys.2020.123452.

[9] Aparroz, “Aparroz, levamos o nosso arroz a sério.” https://aparroz.com/ (accessed Sep. 16, 2021).

[10] C. S. Wu and C. H. Tsou, “Fabrication, characterization, and application of biocomposites from poly(lactic acid) with renewable rice husk as reinforcement,” *J. Polym. Res.*, vol. 26, no. 2, 2019, doi: 10.1007/s10965-019-1710-z.

[11] M. R. Sanjay, P. Madhu, M. Jawaid, P. Senthamaraikannan, S. Senthil, and S. Pradeep, “Characterization and properties of natural fiber polymer composites: A comprehensive review,” *J. Clean. Prod.*, vol. 172, pp. 566–581, 2018, doi: 10.1016/j.jclepro.2017.10.101.

[12] C. H. Tsou *et al.*, “Preparation and characterization of renewable composites from Polylactide and Rice husk for 3D printing applications,” *J. Polym. Res.*, vol. 26, no. 9, 2019,

doi: 10.1007/s10965-019-1882-6.

[13] M. Ramesh, K. Palanikumar, and K. H. Reddy, “Plant fibre based bio-composites: Sustainable and renewable green materials,” *Renew. Sustain. Energy Rev.*, vol. 79, no. May, pp. 558–584, 2017, doi: 10.1016/j.rser.2017.05.094.

[14] V. Mazzanti, R. Pariante, A. Bonanno, O. Ruiz de Ballesteros, F. Mollica, and G. Filippone, “Reinforcing mechanisms of natural fibers in green composites: Role of fibers morphology in a PLA/hemp model system,” *Compos. Sci. Technol.*, vol. 180, no. March, pp. 51–59, Aug. 2019, doi: 10.1016/j.compscitech.2019.05.015.

[15] X. Li, L. G. Tabil, and S. Panigrahi, “Chemical treatments of natural fiber for use in natural fiber-reinforced composites: A review,” *J. Polym. Environ.*, vol. 15, no. 1, pp. 25–33, 2007, doi: 10.1007/s10924-006-0042-3.

[16] F. M. Al-Oqla and M. S. Salit, *Materials Selection for Natural Fiber Composites*. Elsevier, 2017.

[17] D. D. Stokke, Q. Wu, and G. Han, *Introduction to Wood and Natural Fiber Composites*. Chichester, UK: John Wiley & Sons Ltd, 2013.

[18] A. Gallos, G. Paës, F. Allais, and J. Beaugrand, “Lignocellulosic fibers: a critical review of the extrusion process for enhancement of the properties of natural fiber composites,” *RSC Adv.*, vol. 7, no. 55, pp. 34638–34654, 2017, doi: 10.1039/C7RA05240E.

[19] Y. Su *et al.*, “Prospects for Replacement of Some Plastics in Packaging with Lignocellulose Materials: A Brief Review,” *BioResources*, vol. 13, no. 2, pp. 4550–4576, Feb. 2018, doi: 10.15376/biores.13.2.Su.

[20] M. Kariz, M. Sernek, M. Obućina, and M. K. Kuzman, “Effect of wood content in FDM filament on properties of 3D printed parts,” *Mater. Today Commun.*, vol. 14, no. December 2017, pp. 135–140, 2018, doi: 10.1016/j.mtcomm.2017.12.016.

[21] B. Koohestani, A. K. Darban, P. Mokhtari, E. Yilmaz, and E. Darezereshki, “Comparison of different natural fiber treatments: a literature review,” *Int. J. Environ. Sci. Technol.*, vol. 16, no. 1, pp. 629–642, Jan. 2019, doi: 10.1007/s13762-018-1890-9.

[22] M. R. Mansor and S. Mohd Sapuan, *Concurrent Conceptual Design and Materials Selection of Natural Fiber Composite Products*. Singapore: Springer Singapore, 2018.

[23] A. K. Lau and A. P. Y. Hung, *Natural fiber-reinforced biodegradable and bioresorbable polymer composites*. Woodhead Publishing, 2017.

[24] University of Nebraska Lincoln, “Garden Terms: Plant Classification.” https://extensionpublications.unl.edu/assets/pdf/ec1258.pdf (accessed Oct. 05, 2021).

[25] A. K. Mohanty, M. Misra, and L. T. Drzal, “Surface modifications of natural fibers and performance of the resulting biocomposites: An overview,” *Compos. Interfaces*, vol. 8, no. 5, pp. 313–343, Jan. 2001, doi: 10.1163/156855401753255422.

[26] A. Mohanty, M. Misra, L. Drzal, S. Selke, B. Harte, and G. Hinrichsen, “Natural Fibers, Biopolymers, and Biocomposites,” in *Natural Fibers, Biopolymers, and Biocomposites*, CRC Press, 2005, pp. 1–877.

[27] M. M. Kabir, H. Wang, K. T. Lau, and F. Cardona, “Chemical treatments on plant-based natural fibre reinforced polymer composites: An overview,” *Compos. Part B Eng.*, vol. 43, no. 7, pp. 2883–2892, Oct. 2012, doi: 10.1016/j.compositesb.2012.04.053.

[28] J. Müssig, *Industrial Applications of Natural Fibres*. Chichester, UK: John Wiley & Sons, Ltd, 2010.

[29] Y. Zou and T. Yang, “Rice Husk, Rice Husk Ash and Their Applications,” in *Rice Bran and Rice Bran Oil*, Elsevier, 2019, pp. 207–246.

[30] N. Petchwattana, W. Channuan, P. Naknaen, and B. Narupai, “3D printing filaments prepared from modified poly(lactic acid)/teak wood flour composites: An investigation on the particle size effects and silane coupling agent compatibilisation,” *J. Phys. Sci.*, vol. 30, no. 2, pp. 169–188, 2019, doi: 10.21315/jps2019.30.2.10.

[31] Ahmad Adlie Shamsuri *, “Important Criteria for Preparation of 3D Printer Filaments from Polymer Biocomposites ,” *SVOA Mater. Sci. Technol.*, vol. 1, no. 1, pp. 1–3, 2019.

[32] C. Kukla, J. Gonzalez-Gutierrez, I. Duretek, S. Schuschnigg, and C. Holzer, “Effect of particle size on the properties of highly-filled polymers for fused filament fabrication,” in *AIP Conference Proceedings*, 2017, vol. 1914, no. December 2017, p. 190006, doi: 10.1063/1.5016795.

[33] M. Morales, C. Atencio Martinez, A. Maranon, C. Hernandez, V. Michaud, and A. Porras, “Development and Characterization of Rice Husk and Recycled Polypropylene Composite Filaments for 3D Printing,” *Polymers (Basel).*, vol. 13, no. 7, p. 1067, Mar. 2021, doi: 10.3390/polym13071067.

[34] D. Depuydt *et al.*, “Production and characterization of bamboo and flax fiber reinforced polylactic acid filaments for fused deposition modeling (FDM),” *Polym. Compos.*, vol. 40, no. 5, pp. 1951–1963, 2019, doi: 10.1002/pc.24971.

[35] Y. Tao, H. Wang, Z. Li, P. Li, and S. Q. Shi, “Development and application ofwood flour-filled polylactic acid composite filament for 3d printing,” *Materials (Basel).*, vol. 10, no. 4, pp. 1–6, 2017, doi: 10.3390/ma10040339.

[36] M. Benítez-Guerrero, L. A. Pérez-Maqueda, R. Artiaga, P. E. Sánchez-Jiménez, and J. Pascual-Cosp, “Structural and Chemical Characteristics of Sisal Fiber and Its Components: Effect of Washing and Grinding,” *J. Nat. Fibers*, vol. 14, no. 1, pp. 26–39, Jan. 2017, doi: 10.1080/15440478.2015.1137529.

[37] E. Csiszár and E. Fekete, “Microstructure and Surface Properties of Fibrous and Ground Cellulosic Substrates,” *Langmuir*, vol. 27, no. 13, pp. 8444–8450, Jul. 2011, doi: 10.1021/la201039a.

[38] Y. Huang, S. Löschke, and G. Proust, “In the mix: The effect of wood composition on the 3D printability and mechanical performance of wood-plastic composites,” *Compos. Part C Open Access*, vol. 5, no. March, p. 100140, Jul. 2021, doi: 10.1016/j.jcomc.2021.100140.

[39] A. Saidah, S. E. Susilowati, and Y. Nofendri, “Effect of Fiber Loading and Alkali Treatment on Rice Straw Fiber Reinforced Composite for Automotive Bumper Beam Application,” *Int. J. Adv. Sci. Eng. Inf. Technol.*, vol. 9, no. 6, p. 1865, Dec. 2019, doi: 10.18517/ijaseit.9.6.7006.

[40] N. Cordeiro, C. Gouveia, and M. J. John, “Investigation of surface properties of physico-chemically modified natural fibres using inverse gas chromatography,” *Ind. Crops Prod.*, vol. 33, no. 1, pp. 108–115, 2011, doi: 10.1016/j.indcrop.2010.09.008.

[41] T. P. T. Tran, J.-C. Bénézet, and A. Bergeret, “Rice and Einkorn wheat husks reinforced poly(lactic acid) (PLA) biocomposites: Effects of alkaline and silane surface treatments of husks,” *Ind. Crops Prod.*, vol. 58, pp. 111–124, Jul. 2014, doi: 10.1016/j.indcrop.2014.04.012.

[42] M. Kathirselvam, A. Kumaravel, V. P. Arthanarieswaran, and S. S. Saravanakumar, “Characterization of cellulose fibers in Thespesia populnea barks: Influence of alkali treatment,” *Carbohydr. Polym.*, vol. 217, no. April, pp. 178–189, Aug. 2019, doi: 10.1016/j.carbpol.2019.04.063.

[43] N. Johar, I. Ahmad, and A. Dufresne, “Extraction, preparation and characterization of cellulose fibres and nanocrystals from rice husk,” *Ind. Crops Prod.*, vol. 37, no. 1, pp. 93–99, May 2012, doi: 10.1016/j.indcrop.2011.12.016.

[44] P. Ramadevi, D. Sampathkumar, C. V. Srinivasa, and B. Bennehalli, “Effect of alkali treatment on water absorption of single cellulosic abaca fiber,” *BioResources*, vol. 7, no. 3, pp. 3515–3524, 2012, doi: 10.15376/biores.7.3.3515-3524.

[45] H. Kargarzadeh, N. Johar, and I. Ahmad, “Starch biocomposite film reinforced by multiscale rice husk fiber,” *Compos. Sci. Technol.*, vol. 151, pp. 147–155, Oct. 2017, doi: 10.1016/j.compscitech.2017.08.018.

[46] D. Jain, H. Sekhon, T. K. Bera, and R. Jain, “Comparison of different hydrophobic treatments for the durability improvement of palmyra natural fiber composites under hydrothermal ageing environments,” *J. Nat. Fibers*, vol. 17, no. 11, pp. 1–15, Nov. 2020, doi: 10.1080/15440478.2019.1588828.

[47] R. Sepe, F. Bollino, L. Boccarusso, and F. Caputo, “Influence of chemical treatments on mechanical properties of hemp fiber reinforced composites,” *Compos. Part B Eng.*, vol. 133, pp. 210–217, 2018, doi: 10.1016/j.compositesb.2017.09.030.

[48] S. Wang, L. Capoen, D. R. D’hooge, and L. Cardon, “Can the melt flow index be used to predict the success of fused deposition modelling of commercial poly(lactic acid) filaments into 3D printed materials?,” *Plast. Rubber Compos.*, vol. 47, no. 1, pp. 9–16, 2018, doi:

10.1080/14658011.2017.1397308.

[49] A. Le Duigou, D. Correa, M. Ueda, R. Matsuzaki, and M. Castro, “A review of 3D and 4D printing of natural fibre biocomposites,” *Mater. Des.*, vol. 194, p. 108911, Sep. 2020, doi: 10.1016/j.matdes.2020.108911.

[50] J. Shao, S. Xiang, X. Bian, J. Sun, G. Li, and X. Chen, “Remarkable melting behavior of PLA stereocomplex in linear PLLA/PDLA blends,” *Ind. Eng. Chem. Res.*, vol. 54, no. 7, pp. 2246–2253, 2015, doi: 10.1021/ie504484b.

[51] esun3d, “esun3d.” https://esun3d.net/ (accessed Oct. 17, 2021).

[52] Prusa, “Prusa Research - Official Josef Prusa Shop.” https://shop.prusa3d.com/en/filament (accessed Oct. 17, 2021).

[53] dowire, “dowire - printer filament.” https://dowire.pt/wp/produto/filamento-3d-dowire-pwood/ (accessed Oct. 17, 2021).

[54] E. Gkartzou, E. P. Koumoulos, and C. A. Charitidis, “Production and 3D printing processing of bio-based thermoplastic filament,” *Manuf. Rev.*, vol. 4, pp. 1–13, 2017, doi: 10.1051/mfreview/2016020.

[55] J. R. Wagner, E. M. Mount, and H. F. Giles, *Extrusion*. Elsevier, 2014.

[56] M. Gale, *Mixing in single screw extrusion*. ISmithers, 2009.

[57] Z. Refaa, M. Boutaous, S. Xin, and D. A. Siginer, “Thermophysical analysis and modeling of the crystallization and melting behavior of PLA with talc: Kinetics and crystalline structures,” *J. Therm. Anal. Calorim.*, vol. 128, no. 2, pp. 687–698, 2017, doi: 10.1007/s10973-016-5961-1.

[58] R. Blackburn, *Biodegradable and sustainable fibres*. Elsevier, 2005.

[59] NatureWorks LLC, “How Ingeo is Made.” https://www.natureworksllc.com/What-is-Ingeo/How-Ingeo-is-Made (accessed Oct. 17, 2021).

[60] R. A. Auras, L.-T. Lim, S. E. M. Selke, and H. Tsuji, *Poly (lactic acid): synthesis, structures, properties, processing, and applications*, vol. 10. John Wiley & Sons, 2011.

[61] D. R. Witzke, *Introduction to properties, engineering, and prospects of polylactide polymers*. Michigan State University, 1997.

[62] X. Xiao, V. S. Chevali, P. Song, D. He, and H. Wang, “Polylactide/hemp hurd biocomposites as sustainable 3D printing feedstock,” *Compos. Sci. Technol.*, vol. 184, no. April, pp. 1–8, 2019, doi: 10.1016/j.compscitech.2019.107887.

[63] A. Le Duigou, A. Barbé, E. Guillou, and M. Castro, “3D printing of continuous flax fibre reinforced biocomposites for structural applications,” *Mater. Des.*, vol. 180, p. 107884, 2019, doi: 10.1016/j.matdes.2019.107884.

[64] C. A. Murphy and M. N. Collins, “Microcrystalline cellulose reinforced polylactic acid

biocomposite filaments for 3D printing," *Polym. Compos.*, vol. 39, no. 4, pp. 1311–1320, Apr. 2018, doi: 10.1002/pc.24069.

[65] V. Mimini *et al.*, "Compatibility of Kraft Lignin, Organosolv Lignin and Lignosulfonate With PLA in 3D Printing," *J. Wood Chem. Technol.*, vol. 39, no. 1, pp. 14–30, 2019, doi: 10.1080/02773813.2018.1488875.

[66] F. Daver, K. P. M. Lee, M. Brandt, and R. Shanks, "Cork–PLA composite filaments for fused deposition modelling," *Compos. Sci. Technol.*, vol. 168, no. September, pp. 230–237, 2018, doi: 10.1016/j.compscitech.2018.10.008.

[67] A. N. Frone *et al.*, "Morpho-structural, thermal and mechanical properties of PLA/PHB/Cellulose biodegradable nanocomposites obtained by compression molding, extrusion, and 3d printing," *Nanomaterials*, vol. 10, no. 1, pp. 1–20, 2020, doi: 10.3390/nano10010051.

[68] S. T. Lee, *Polymeric Foams*. CRC Press, 2016.

[69] J.-M. Bouvier and O. H. Campanella, *Extrusion Processing Technology*. Chichester, UK: John Wiley & Sons, Ltd, 2014.

[70] 3Devo, "Composer 450." https://3devo.com/product/composer-450/ (accessed Oct. 21, 2021).

[71] M. Jonoobi, J. Harun, A. P. Mathew, and K. Oksman, "Mechanical properties of cellulose nanofiber (CNF) reinforced polylactic acid (PLA) prepared by twin screw extrusion," *Compos. Sci. Technol.*, vol. 70, no. 12, pp. 1742–1747, 2010, doi: 10.1016/j.compscitech.2010.07.005.

[72] S. Singh, G. Singh, C. Prakash, S. Ramakrishna, L. Lamberti, and C. I. Pruncu, "3D printed biodegradable composites: An insight into mechanical properties of PLA/chitosan scaffold," *Polym. Test.*, vol. 89, no. July, pp. 1–13, 2020, doi: 10.1016/j.polymertesting.2020.106722.

[73] E. Matias and B. Rao, "3D printing: On its historical evolution and the implications for business," *Portl. Int. Conf. Manag. Eng. Technol.*, vol. 2015-Septe, pp. 551–558, 2015, doi: 10.1109/PICMET.2015.7273052.

[74] B. Shaqour *et al.*, "Gaining a better understanding of the extrusion process in fused filament fabrication 3D printing: a review," *Int. J. Adv. Manuf. Technol.*, vol. 114, no. 5–6, pp. 1279–1291, May 2021, doi: 10.1007/s00170-021-06918-6.

[75] Fortune Business Insights, "3D printing market." https://www.fortunebusinessinsights.com/industry-reports/3d-printing-market-101902 (accessed Oct. 23, 2021).

[76] Prusa Research, "Original Prusa i3 MK3S." https://shop.prusa3d.com/en/3d-printers (accessed Oct. 23, 2021).

[77] anycubic, “Kossel Plus.” https://www.anycubic.com/products/anycubic-kossel-3d-printer (accessed Oct. 23, 2021).

[78] Stratasys, “Fortus 450mc.” https://www.stratasys.com/3d-printers/fortus-450mc (accessed Oct. 23, 2021).

[79] A. Fatih, Y. Corresponding, and I. Yavuz, “Effect of Heat Break Geometry on the Thermal Performance of A 3D Printer Extruder,” *Int. J. Sci. Technol. Res.*, vol. 6, no. 12, pp. 41–50, Dec. 2020, doi: 10.7176/JSTR/6-12-05.

[80] A. García-Domínguez, J. Claver, A. M. Camacho, and M. A. Sebastián, “Considerations on the applicability of test methods for mechanical characterization of materials manufactured by FDM,” *Materials (Basel).*, vol. 13, no. 1, p. 28, Dec. 2020, doi: 10.3390/ma13010028.

[81] M.-H. Hsueh *et al.*, “Effect of Printing Parameters on the Tensile Properties of 3D-Printed Polylactic Acid (PLA) Based on Fused Deposition Modeling,” *Polymers (Basel).*, vol. 13, no. 14, p. 2387, Jul. 2021, doi: 10.3390/polym13142387.

[82] C. Camposeco-Negrete, “Optimization of printing parameters in fused deposition modeling for improving part quality and process sustainability,” *Int. J. Adv. Manuf. Technol.*, vol. 108, no. 7–8, pp. 2131–2147, Jun. 2020, doi: 10.1007/s00170-020-05555-9.

[83] D. Bermudez, P. A. Quiñonez, E. J. Vasquez, I. A. Carrete, T. J. Word, and D. A. Roberson, “A Comparison of the physical properties of two commercial 3D printing PLA grades,” *Virtual Phys. Prototyp.*, vol. 16, no. 2, pp. 178–195, 2021, doi: 10.1080/17452759.2021.1910047.

[84] H. Long *et al.*, “Mechanical and thermal properties of bamboo fiber reinforced polypropylene/polylactic acid composites for 3D printing,” *Polym. Eng. Sci.*, vol. 59, no. s2, pp. E247–E260, 2019, doi: 10.1002/pen.25043.

[85] M. Tanase-Opedal, E. Espinosa, A. Rodríguez, and G. Chinga-Carrasco, “Lignin: A biopolymer from forestry biomass for biocomposites and 3D printing,” *Materials (Basel).*, vol. 12, no. 18, pp. 1–15, 2019, doi: 10.3390/ma12183006.

[86] R. Guo, Z. Ren, H. Bi, Y. Song, and M. Xu, “Effect of toughening agents on the properties of poplar wood flour/poly (lactic acid) composites fabricated with Fused Deposition Modeling,” *Eur. Polym. J.*, vol. 107, no. June, pp. 34–45, Oct. 2018, doi: 10.1016/j.eurpolymj.2018.07.035.

[87] I. S. Organization, “ISO 527-4: Determination of Tensile Properties—Part 4: Test Conditions for Isotropic and Orthotropic Fibre-Reinforced Plastic Composites.” International Standards Organization, 1997.

[88] I. ASTM, “Standard test methods for flexural properties of unreinforced and reinforced plastics and electrical insulating materials,” *ASTM D790-07*. ASTM Inernational, 2007.

[89] PerkinElmer, “Spectrum Two FT-IR Spectrometer.” https://www.perkinelmer.com/product/spectrum-two-ft-ir-sp10-software-l160000a (accessed Nov. 06, 2021).

[90] HITACHI, “Thermogravimetry/Differential Thermal Analyzer STA7200RV.” https://www.hitachi-hightech.com/global/sinews/technical_explanation/0656/ (accessed Nov. 06, 2021).

[91] Y. Kim, D. Jeong, K. Park, J.-H. Yu, and S. Jung, “Efficient Adsorption on Benzoyl and Stearoyl Cellulose to Remove Phenanthrene and Pyrene from Aqueous Solution,” *Polymers (Basel).*, vol. 10, no. 9, p. 1042, Sep. 2018, doi: 10.3390/polym10091042.

[92] B. A.N. and N. K.J., “Characterization of alkali treated and untreated new cellulosic fiber from Saharan aloe vera cactus leaves,” *Carbohydr. Polym.*, vol. 174, pp. 200–208, Oct. 2017, doi: 10.1016/j.carbpol.2017.06.065.

[93] A. Célino, S. Fréour, F. Jacquemin, and P. Casari, “The hygroscopic behavior of plant fibers: a review,” *Front. Chem.*, vol. 1, no. JAN, pp. 1–12, 2014, doi: 10.3389/fchem.2013.00043.